

UNIVERSITY OF CALIFORNIA,
IRVINE

Systematic Error Sources in a Measurement of
G using a Cryogenic Torsion Pendulum

DISSERTATION

submitted in partial satisfaction of the requirements
for the degree of

DOCTOR OF PHILOSOPHY

in Physics

by

William Daniel Cross

Dissertation Committee:
Professor Riley Newman, Chair
Professor Jonas Schultz
Professor Peter Taborek

2009

The dissertation of William Daniel Cross
is approved and is acceptable in quality and form for
publication on microfilm and in digital formats:

Committee Chair

University of California, Irvine
2009

DEDICATION

To

Leslie Allison Bunnage

For her support through this process,
and for being the extraordinarily impressive woman that she is,
she deserves all of my dedication, and more.

I love you, Leslie.

Table of Contents

	Page
LIST OF FIGURES	vii
LIST OF TABLES	x
ACKNOWLEDGEMENTS	xi
CURRICULUM VITAE	xii
ABSTRACT OF THE DISSERTATION	xiii
INTRODUCTION	1
Background	1
Techniques used in G Measurements	4
Motivations	8
Traits of the UCI G Experiment	8
Outline of the Dissertation	9
CHAPTER 1:	
The Static and Dynamic Methods in Gravitational Measurements	11
The Torsion Pendulum	11
The Static Method	12
The Dynamic Method	18
Tilt in the Dynamic Method	19
A Variation of the Dynamic Method: The Second Harmonic Method	19
CHAPTER 2:	
Principles of the UCI G Measurement Approach	21
Ring-Shaped Field Source Masses	21
Flat, Thin Pendulum	22
Large Torsion Amplitude	22
Different Fiber Types	23
Cryogenic Operation	23

TABLE OF CONTENTS (CONTINUED)

		Page
CHAPTER 3:	Motivation for the Design of the Source Mass Rings and Pendulum	26
	Ring Design	28
	Pendulum Design	32
CHAPTER 4:	The Experimental Apparatus	36
	Source Mass Rings	37
	The Pendulum	41
	Fibers	42
	Eddy Current Swing Mode Damping System	42
	Vacuum System	44
	“2K” Helium Pot	46
	Temperature Control System	47
	Optics System	48
	Timing System	52
	Lab Site	52
CHAPTER 5:	Further Formalism in a Dynamic Measurement of Gravity	53
	Conservative Torques Generated by the Pendulum Suspension Fiber	54
	Conservative Torques Generated by Ambient Fields	56
	Higher Order Effects of Torque Perturbation Terms	58
CHAPTER 6:	Systematic Experimental Error Sources	60
	Fiber	60
	Conservative Fiber Anharmonics	61
	Sensitivity to Amplitude Error	63
	Dissipative Fiber Torques	64
	The Stick-Slip Model	67
	The Kuroda Effect	68
	Magnetic Field	70
	Eddy Current Damping	72
	Optics	73
	Pendulum Heating	73
	Second Order Couplings	74
	Other Sources of Error	85

TABLE OF CONTENTS (CONTINUED)

		Page
CHAPTER 7:	Reported Value of G	86
REFERENCES		88
APPENDIX A:	Perturbative Method of Obtaining First-Order Corrections to Simple Harmonic Oscillation from Anharmonic Torques	90
APPENDIX B:	Nonlinear Conservative Fiber Torques: Harmonics, Offset, and Frequency Shifts	98
APPENDIX C:	Conservative Field Torques: Offset, Harmonics, Frequency Shift, Calculation of Coefficients, and Symmetries	102
APPENDIX D:	The Stick-Slip Effect: The Model	110
APPENDIX E:	Magnetic Damping	126

LIST OF FIGURES

	Page
Figure I.1 UCI G Experiment in the Context of CODATA 2006	3
Figure 1.1 Torsion Pendulum (Side View)	11
Figure 1.2 Torsion Pendulum (Top View)	12
Figure 1.3 Static Deflection of a Torsion Pendulum (Top View)	12
Figure 1.4 Optical Measurement System (Top View)	13
Figure 1.5 Static Pendulum Tilt (Top View)	14
Figure 1.6 Translation of a θ_x Tilt into an Erroneous Signal	15
Figure 1.7 Translation of θ_y Tilt into Measurement Error	16
Figure 1.8 Dynamic Method (Top View)	18
Figure 2.1 $\Delta\omega^2$ (Arbitrary Scale) vs. A (Radians) for the UCI Experiment	23
Figure 3.1 Model of Thin Rings Source Masses	29
Figure 3.2 Gravitational Potential of an Idealized Coaxial Two-Ring System, Along the Axis of Symmetry (arbitrary vertical axis)	29
Figure 3.3 $\frac{\partial g_x}{\partial x} = -\frac{\partial^2 \Phi}{\partial x^2}$ of an Idealized Coaxial Two-Ring System, Along the Axis of Symmetry	30
Figure 3.4 PPM Error in G Arising from an Undetected Pendulum Position Misplacement along the x-axis	32
Figure 3.5 Pendulum	34
Figure 4.1 The Cryostat	37

LIST OF FIGURES (continued)

	Page
Figure 4.2 Copper Source Mass Ring (one)	38
Figure 4.3 Rings with Constraining Rods	39
Figure 4.4 The UCI G Pendulum	41
Figure 4.5 Cross Section of an Azimuthally Symmetric Swing Mode Eddy Current Damping Device	43
Figure 4.6 Swing and Bounce Mode Eddy Current Damper	44
Figure 4.7 The Vacuum Can of the Cryostat	46
Figure 4.8 Optical Focusing during a Zero Crossing	49
Figure 4.9 Detector During a Transit	50
Figure 4.10 Summed Photodetector Signal during a “Zero Crossing”	50
Figure 4.11 Placement of 4 Primary (45 degree) and Secondary (90 degree) Mirrors around the UCI G Pendulum	51
Figure 6.1 The Stick-Slip Effect	67
Figure 6.2 Harmonic Spring with One Maxwell Unit	69
Figure 6.3 Points Used to Determine C_i and D_{ij} Cross Terms	78
Figure C.1 Symmetry in $\text{Re}(e^{im\phi})$ (facing toward the -z direction)	108
Figure C.2 Node Representation of $P_{lm}(\cos\theta)$, as a Function of Polar Angle, θ	109
Figure D.1 Blocks in a 1-Dimensional Parallel Stick-Slip Model	110
Figure D.2 Stick-Slip Force for a One Slipping Block System	114

LIST OF FIGURES (continued)

	Page
Figure D.3 $F_{ss}(x)$ for a Large Number of Stick-Slip Blocks	119
Figure D.4 Stick-Slip Blocks in a Series Configuration	121
Figure D.5 Torque as a Function of Amplitude for a Small Series Stick-Slip Effect	123

LIST OF TABLES

	Page
Table I.1 Change in Period of the UCI G Pendulum due to the Presence of the Source Masses	3
Table 4.1 The Four Stages of Temperature Control for the UCI G Experiment	47
Table 6.1 Error in G from Systematic Amplitude Excitations (δA) during Ring Modulation due to a Torque k_3 Frequency Shift	62
Table 6.2 $C_i(A)$	80
Table 6.3 dC_i/dA (rad^{-1})	81
Table 6.4 Values of D_{sj}	82
Table 6.5 dD_{sj}/dA (rad^{-1})	83
Table 6.6 Limits on Change in G from Second Order Couplings at Signal Maxima and 0.3 Rad	84
Table 6.7: $d\text{Log}(G)/dA$ (rad) from Second Order Couplings at Signal Maxima and 0.3 Radians	85
Table B.1 Sample Offset, Change of Frequency, and Harmonics of k_m through $m = 7$	101
Table D.1 a_n For Series Stick-Slip Effect	125

ACKNOWLEDGEMENTS

I would like to express my thanks in particular to the following individuals and institutions:

To my advisor, Professor Riley Newman, for welcoming me into his lab, for teaching me so many things about the how to better examine the physical world, for his relentless intelligence and his relentless effort, for his patience with me, for his efforts on my behalf, and for his integrity. With another advisor, I might never have completed this thesis.

To Dr. Eric Berg, for his efforts on my behalf, for the many times he stopped me from rushing to make a fool of myself, for his ability to bring structure to chaos, and especially for his encouragement. Without him, I would certainly never have finished this thesis.

To Michael Bantel, for his early efforts on this experiment. His inventions and his writings have helped me immensely.

To my wife, Leslie Bunnage, for her patience, her support, and occasionally, her sharp prodding. She has helped me immeasurably throughout this process.

To my the family that raised me: to my parents, Susan Catherine Cross and William David Cross, and to my younger brother, Zachary Index Cross for the wonderful childhood they gave me.

To my classroom teachers over these many years, for the time and energy they put into my development, each of whom brought learning to life in their own way that can't be explained in a brief few words. Some of those that I remember best are mentioned, but the list is far from exhaustive. From Lowell Elementary of Everett, WA, Ms. Mets (kindergarten). From Beaumont Elementary of Vista, CA, Ms. Luke (4th grade), for her persistence. From Washington Middle School of Vista High: Ms. Colclough (6th grade science and math), for refusing to be bound by curriculum guidelines when it didn't fit one unusual student; Ms. Gibson (7th grade literature and social studies), for her rigor; and Mr. Kellish (8th grade literature and social studies), for teaching me (by example) that being brilliant can be a lot of fun. From Vista High School of Vista, CA: Mr. Madison (10th and 11th grade chemistry), for encourage me to succeed not just in science, but throughout life; Ms. Barnes (11th grade literature), of Vista High School in Vista, CA, for the sharp wit she brought to bear on her students; Mr. Barnes (no relation) (history), of Vista High School in Vista, CA, for his easygoing fun; Mr. Gastauer (9th and 11th grade biology; JV swimming coach), for being awesome in so many ways; Gus Tavis (12th grade philosophy), for his enthusiasm for the material and encouragement for his students; and Ms. Gammon (12th grade biology), for her relentless effort. From UCSD, all for bringing the material alive: Brian Maple (1st year mechanics), Aneesh Manohar (3rd year mechanics), Donald Fredkin (statistical mechanics and electrodynamics), and Arthur Droge (several classes in religious studies). From UC Irvine, again, all for bringing the material alive: Myron Bander (mechanics, electrodynamics, and particle physics), Jonas Schultz (statistical mechanics), and Arvind Rajaraman (particle physics and statistical mechanics).

To the University of California, Irvine, and the National Science Foundation. Financial support was provided by grant numbers 9514944, 0108937, 0404514, and 0701707 that have made this research possible.

CURRICULUM VITAE

William Daniel Cross

- 1996 Full International Baccalaureate Scholar, Vista High School
- 2001 B. S. in Physics, University of California, San Diego
- 2001-02 Teaching Assistant, UCI Physics Department
- 2002-09 Research Assistant, UCI Physics Department
- 2003 M. S. in Physics, University of California, Irvine
- 2009 Ph. D. in Physics, University of California, Irvine

FIELD OF STUDY

Torsion Pendulums; Cryogenics; Vacuum Equipment; Gravitational Measurement

PUBLICATIONS

“Conceptual design of beam-ion profile diagnostics for the DIII-D tokamak.” Heidbrink, W. W., Cross, W. C., Krasilnikov, A. V. *Rev. Sci. Instrum.* **74** 1743 (2003);
DOI:10.1063/1.1534399

(planned but not yet submitted)

“A Measurement of G Using a Cryogenic Torsion Pendulum” M. K. Bantel, E. C. Berg, W. D. Cross, R. D. Newman (UC Irvine)

ABSTRACT OF THE DISSERTATION

Systematic Error Sources in a Measurement of
G using a Cryogenic Torsion Pendulum

By

William Daniel Cross

Doctor of Philosophy in Physics

University of California, Irvine, 2009

Professor Riley D. Newman, Chair

This dissertation attempts to explore and quantify systematic errors that arise in a measurement of G (the gravitational constant from Newton's Law of Gravitation) using a cryogenic torsion pendulum. It begins by exploring the techniques frequently used to measure G with a torsion pendulum, features of the particular method used at UC Irvine, and the motivations behind those features. It proceeds to describe the particular apparatus used in the UCI G measurement, and the formalism involved in a gravitational torsion pendulum experiment. It then describes and quantifies the systematic errors that have arisen, particularly those that arise from the torsion fiber and from the influence of ambient background gravitational, electrostatic, and magnetic fields. The dissertation concludes by presenting the value of G that the lab has reported.

Introduction

This work is a study of known systematic error sources in a measurement of G using a cryogenic torsion pendulum. The measurement builds upon work dating back to the original Cavendish experiment in the 18th century [1], and is part of an attempt to introduce a new refinement (cryogenics) into the usage of the classic torsion pendulum.

Background

Recent measurements of G have been plagued by systematic errors. This is manifestly apparent when one considers the published values of G and their assigned uncertainties. For instance, the German Physikalisch-Technische Bundesanstalt (PTB) group published, in 1995, a value [2] of G that differed by over half a percent, or 50 standard deviations, from the accepted value suggested by the Committee on Data for Science and Technology (“CODATA”) [3]. Although several years later the PTB group corrected [4] this measurement to a value more closely associated with CODATA, this only served to emphasize the subtlety of systematic errors that can arise in a G measurement. Other recent measurements, while in considerably better agreement with CODATA, nevertheless don't agree with one another as well as their collective error bars imply [5, 6, 7, 8, 9, 10, 11, 12]. Clearly, more work is needed in order to improve our confidence in the value of G .

The nature of dominant systematic error sources varies widely among modern G measurements. The various experiments that contribute to the most recent (2006) CODATA differ greatly in their experimental techniques. Most experiments have employed a pendulum, but that pendulum may be either used in a static deflection mode [6, 7, 8, 10] or in a torsional oscillation mode [6, 8, 11], on either a stationary [2, 6, 8, 10, 11] or a rotating [7, 6] frame of reference, using either a thin fiber [6, 10, 11] a relatively wide torsion strip [8, 10], or no fiber at all [2]. The source mass has been either spheres [6, 7], or cylinders [2, 8, 10, 11]. A few of the experiments use no torsion device at all [9, 12]. The large spread of G values obtained with the various measurement methods shows the need for a careful accounting of the systematic errors in any measurement of G. See Figure 1.

Figure I.1: UCI G Experiment in the Context of CODATA 2006

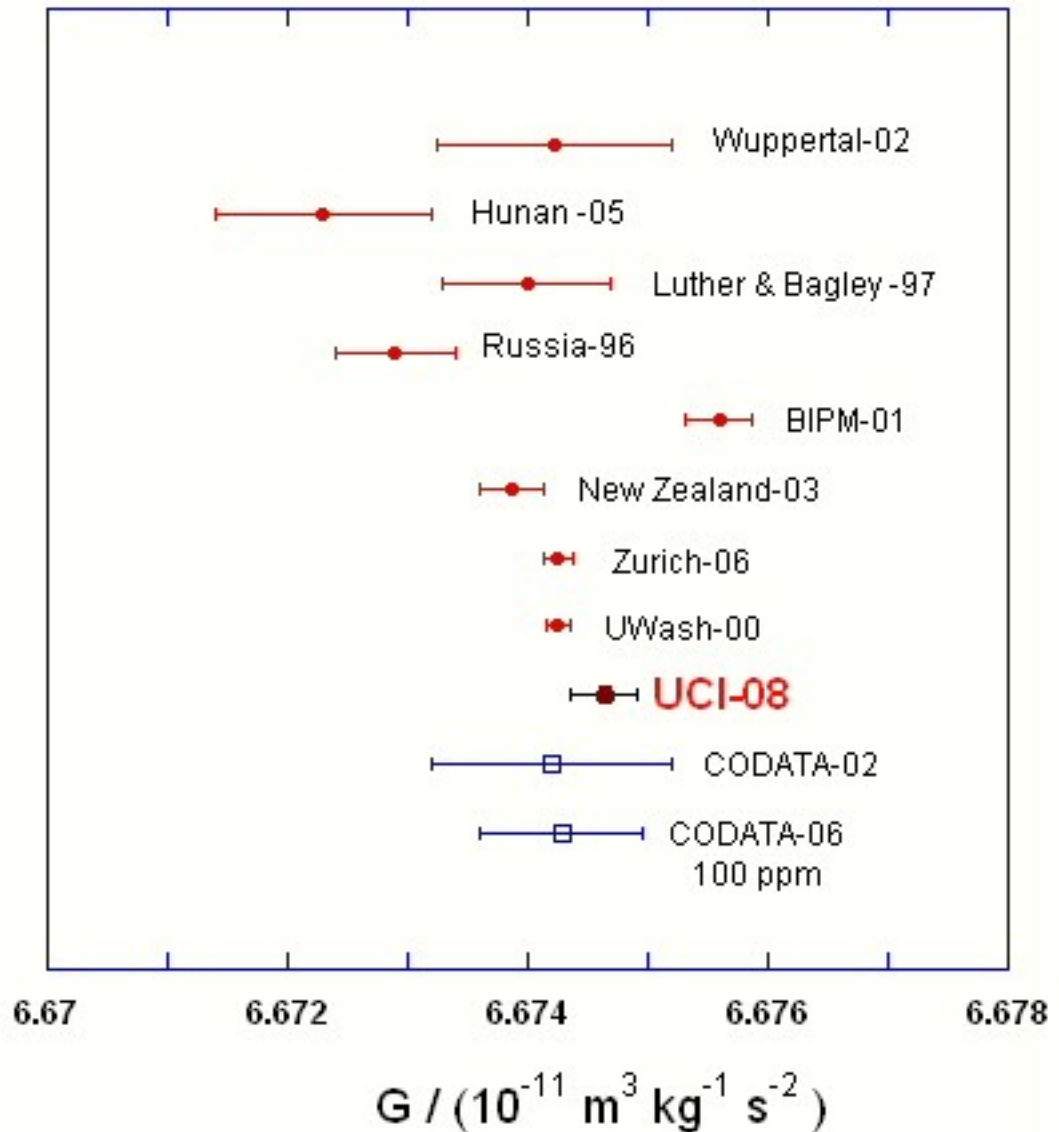


Figure 1 displays the G measurement results incorporated in the 2006 CODATA assessment of the value of G . Dates of publication are indicated in the labels. Labels correspond to references in this thesis as follows: Wuppertal-02 [9], Hunan-02, [11], Luther & Bagley-97 [6], Russia-96 [5], BIPM-01[8], New Zealand-03 [10], Zurich-06 [12], UWash-00 [7]. CODATA-02 displays the G value and 1 sigma uncertainty assigned in the 2002 CODATA

assessment, while the G value labeled "CODATA-06" is the 2006 CODATA assessment, based on the G values displayed above.

Techniques Used in G Measurements

The first recorded use of a torsion pendulum to measure gravity [1] involved measuring the static deflection of a pendulum from its equilibrium angle using a gravitational source mass. As the source mass position modulates, the equilibrium angle changes. If one has carefully accounted for all electrostatic, magnetostatic, and kinetic forces (ie, wind, convection currents, etc) to the level where they cannot affect the results of the experiment, the remaining forces on the pendulum are of two types: the first is the gravitational pull of the source masses, and the second is the restorative fiber torque. If one understands the behavior of the torsion fiber, has accurately gaged the geometry of the source masses, and can reliably measure the deflection magnitude, then the value of G can be inferred.

With this static technique, a number of issues arise. In the original Cavendish experiment, the pendulum's deflection angle was measured by visual observation; in a modern variation, a beam of light is typically reflected by a mirror mounted on the pendulum back to an electronic detector. The deflection is recorded and averaged over a period of time. In both variations, errors can result from poor calibration of the optical readout system.

In a high precision experiment, the number of photons reaching the detector can fluctuate, giving rise to "Shot noise." Increasing the amount of incident light will increase the signal-to-noise ratio, but may cause saturation of the detector. The fraction of incident

light that is absorbed by the mirror can lead to heating of the pendulum which will, in turn, change the pendulum's geometry, affect the behavior of the torsion fiber, and, if the pendulum is not in high vacuum, cause convection currents to form.

One must also take care in interpreting measurements of the pendulum's torsion constant. While the “torsion constant” is nearly constant, high precision experiments can detect a change in its value due to a change in the load that the torsion fiber carries, or the fiber's temperature, frequency of oscillation, amplitude, and even the time since its temperature or load was changed. Over time, its equilibrium angle will drift, as well.

A particularly insidious problem can arise in a direct measurement of the fiber's torsion constant, which is determined by setting the pendulum into torsional oscillation, and measuring its period. Because the moment of inertia of the pendulum can be determined from its geometry, a measurement of the period allows one to calculate the torsion constant of the fiber. However, Kuroda [14] has shown that a component of the torsion “constant” is frequency-dependent: more specifically, the torsion constant seems to increase with increasing frequency. This “Kuroda effect” (which will be described in more detail in chapter 6) means that there would be a lower effective torsion constant in a slowly modulated gravity experiment than would be inferred in a relatively high-frequency torsion constant measurement. A small fractional error in the torsion constant will translate directly into a fractional error in G determination.

A second technique used in a torsion pendulum measurement of gravity is the so-called “dynamic,” or “time of swing” measurement. The pendulum is put into torsional oscillation, and the change in the period of oscillation is measured as a source mass' position is modulated. At a small angle of oscillation, for example, the gravitational torques for one

configuration of the source mass could act in concert with the fiber's restorative torque to increase its effective torsion constant, and the pendulum would oscillate at a slightly higher frequency. Move the source mass to another position, and it will act in opposition to the fiber's restorative torque. The pendulum will then oscillate with a lower frequency. By observing the change in frequency, one can infer the strength of the gravitational interaction.

A characteristic of the dynamic method is that the magnitude of the frequency change depends upon the torsional amplitude of the pendulum. The reason for this is simple: because the fiber torque increases with increasing angular displacement, while the field torques are periodic under a full rotation of the pendulum, the gravitational torques must necessarily sometimes augment the fiber's torque, while at other times resisting it.

A large amplitude oscillator will traverse several of these torque regions over time, with the gravitational torque sometimes pulling it back towards equilibrium, and at other times away from equilibrium. Its torsion frequency is thus determined by a type of weighted average over several such regions (depending upon the time spent in each region). The net effect is a change in frequency that oscillates with increasing amplitude, with extrema of successively smaller magnitude. More specifically, the gravitational perturbation is related to a Bessel function of the oscillation amplitude, A . In the particular case of the UCI experiment, to a good approximation, $\Delta \omega^2 \propto J_1(2A)/A$.

The dynamic method is also sensitive to the Kuroda effect. This is because in a dynamic measurement, the frequency will be higher or lower (depending upon the position of the source masses), but the Kuroda effect can cause the torsion constant to increase in value during the high-frequency portion of the run, and can cause it to decrease during the low-frequency portion of the data run. This will serve to exaggerate any change in

frequency from the source mass modulation, and therefore, increase the measured value of G relative to the actual value.

Some techniques can avoid or minimize the Kuroda effect. For example, some measurements of G [8, 10] use of a narrow strip of metal as a fiber, with a restoring torque that is mostly gravitational in nature (over 96% for the Bureau International des Poids et Mesures, or “BIPM”[8]). It is therefore relatively independent of the material used. The PTB experiment did not even use a fiber, so the Kuroda effect had no bearing upon their experiment. Electrostatic compensation [8, 10] and inertial compensation [13, 7] experiments are by design independent of the fiber's torsion constant, and thus should be immune to any fiber-induced errors.

As will be described in chapter 5, the UCI lab has looked at the magnitude of the Kuroda effect [14] and concluded that it would not contribute significantly to the error budget of its G measurement.

The dynamic method has other problems, as well. For instance, work at the UCI lab has found evidence of a “stick-slip” behavior as a torsion pendulum oscillates, due to the twist in the fiber during oscillation and a tendency of the fiber to retain its shape, with adjacent regions “sticking” in a rigid form until the tension is great enough to make it break free, and “slip.” This will be described in further detail in chapter 3 and appendix D. Other nonlinearities in the fiber (both elastic and inelastic) may also introduce errors, as they change the oscillation profile of the pendulum.

Motivations

The motivation for the study of systematic error presented in this thesis is two-fold: first, to uncover and minimize systematic error in our own G measurement, and second, to be of help to other workers in our lab or other labs who may choose to pursue the use of a cryogenic torsion pendulum in gravitational research.

The UCI G Experiment

The UCI G experiment is a large-amplitude (up to 7.4 radians) torsion pendulum time-of-swing experiment, with a period of between 100s and 135s, a maximum gravitational torque of 1.6×10^{-6} dyn cm, and a shift in period given by Table 1

Table I.1: Change in Period of the UCI G Pendulum
due to the Presence of the Source Masses (assuming a period of 135 s)

Amplitude	Change of Period
small	6.5 ms
2.6 rad	-0.85 ms
4.2 rad	0.42 ms
5.8 rad	-0.26 ms
7.4 rad	0.18 ms

The UCI G experiment modulates source masses in such a way that the change in period between source mass positions is twice the time listed in Table 1.1, which lists change of period relative to absent source masses for a particular source mass position.

Organization of Thesis

Chapter 1 will describe in greater detail the techniques used in static and dynamic torsion pendulum experiments, and variations on each.

Chapter 2 will describe noteworthy aspects of the UCI G experiment that distinguish it from other dynamic torsion pendulum G measurements.

Chapter 3 will discuss in a simplified formal way why the source mass and pendulum were built with the particular geometry that they have.

Chapter 4 will list and describe the various parts of the equipment used in the UCI G experiment: the source mass, the pendulum, the experimental housing and mounts, and relevant parts of the readout system.

Chapter 5 will extend the relevant formalism from chapter 3 and generalize to describe the torques experienced by a torsion pendulum experiment.

Chapter 6 will examine the experiment and quantify its sources of systematic error.

The appendices will involve themselves with the process of determining the first order effects of torques that are weak relative to the torque of the fiber from which the pendulum hangs.

Appendix A will discuss the formalism of a first-order correction to an oscillating pendulum's frequency, offset angle (mean angle), and oscillation “overtones” due to small torques that are functions of the pendulum's angle and angular velocity.

Appendix B will apply the formalism of Appendix A to anharmonic conservative torques associated with the fiber.

Appendix C will apply the formalism of Appendix A to anharmonic conservative torques associated with static field potentials, and describe how to calculate the torques that arise from $1/r^2$ fields.

Appendix D will describe the stick-slip model, and apply the formalism of Appendix A to predict its effects on an oscillating pendulum.

Appendix E will describe weak eddy current damping, and apply the formalism of Appendix A to predict its effects on an oscillating pendulum.

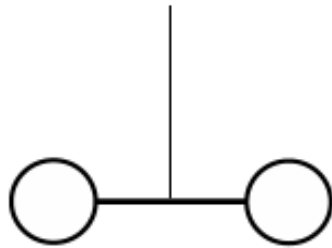
Chapter 1

The Static and Dynamic Methods in Gravitational Measurements

The Torsion Pendulum

A torsion pendulum sensitive to gravitational fields can be thought of as a “bar bell” suspended by a thin torsion fiber.

Figure 1.1: Torsion Pendulum (Side View)

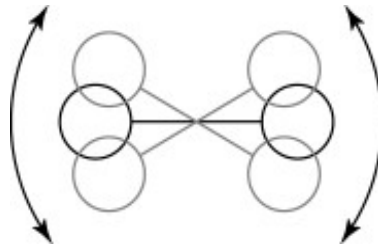


The fiber is under tension from the weight of the pendulum, which is, in turn, free to rotate about the axis of the fiber. If the pendulum is manually twisted, then released, it will enter into harmonic, torsional oscillation, described (to first order) by the following equation:

$$I \ddot{\theta} = -k \theta \quad (1.1)$$

The restorative torsion constant of a thin torsion fiber can be quite small, frequently on the order of 10^{-8} Nt*m/rad.

Figure 1.2: Torsion Pendulum in Oscillation (Top View)

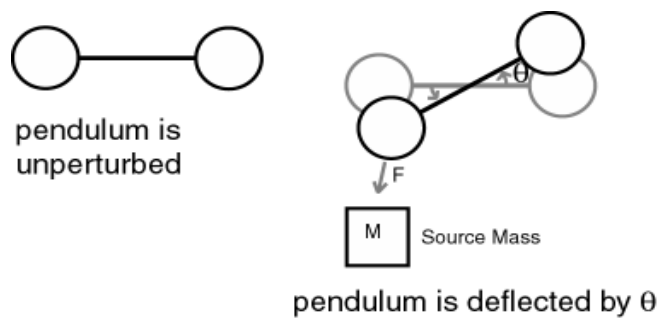


With a torsion pendulum, there are, as described in the introduction, two techniques for measuring a gravitational interaction: the static method, involving a stationary torsion pendulum, and the dynamic method, involving a torsion pendulum in oscillation.

The Static Method

The “static method” is the most straightforward approach to a gravitational experiment using a torsion pendulum. One simply measures the angular deflection of the pendulum in the presence of a source mass. The deflection reveals the interaction strength.

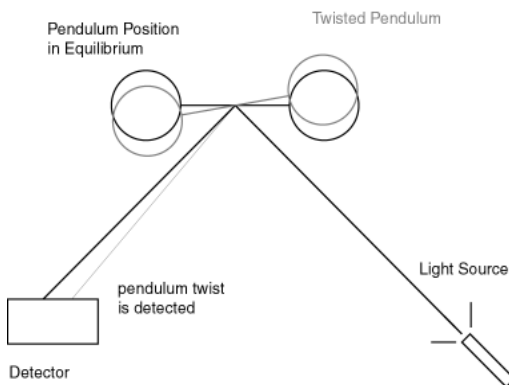
Figure 1.3: Static Deflection of a Torsion Pendulum (Top View)



This method is limited both by the accuracy and precision to which the (very small) deflection can be measured, and the accuracy and precision to which the torsion fiber constant is known. In order to measure this constant, the pendulum is typically set into torsional oscillation in the absence of ambient torques. Its oscillation period is measured, and the torsion constant is calculated using the measured period.

In the static method, the angular displacement is typically measured using an optical lever. Light is reflected by a mirror on the pendulum, and is observed by a position-sensitive detector.

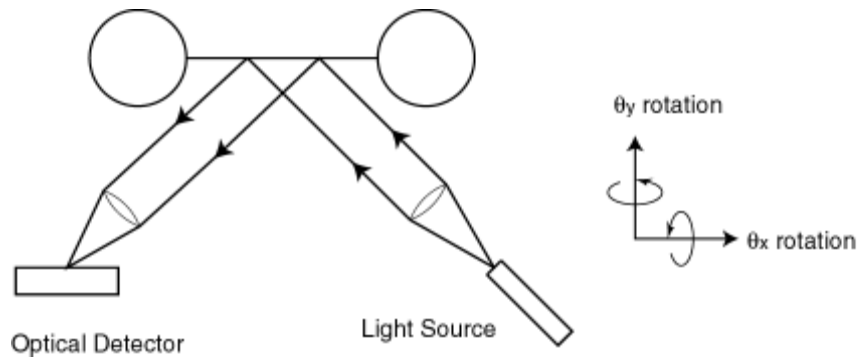
Figure 1.4: Optical Measurement System (Top View)



A danger in using this type of measurement (shown in Figure 1.4) is its sensitivity to apparatus tilt, which can have quite subtle effects. If the experimental housing, within which the torsion fiber is hung, tilts, then the pendulum will change position relative to its immediate environment. This change in position will then result in a false reading of its angular displacement. If this tilt correlates with the modulation of the source mass, this error will propagate and produce a false signal. To reduce this effect, an optical system may be built to collimate the light and focus it onto the detector. With this setup, the detector

remains sensitive to changes in angle, but becomes insensitive to changes in the pendulum's displacement.

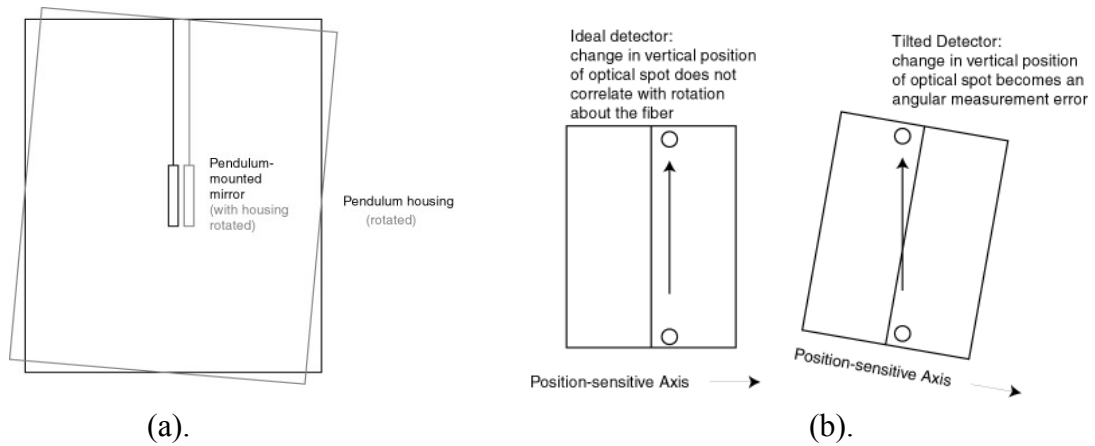
Figure 1.5: Static Pendulum Tilt (Top View)



While this setup (shown in Figure 1.5) reduces sensitivity to tilt-generated pendulum position translation error, the apparatus remains sensitive to tilt through other mechanisms. There are two orthogonal rotations (both shown in Figure 1.5) that do not involve a rotation about the fiber, and both can produce a false signal.

The most obvious effect comes from a combination of a θ_x rotation and a misaligned detector. This can cause the spot on the optical detector to become displaced in the z-direction. See Figure 1.6 (a) and (b).

Figure 1.6: Translation of a θ_x Tilt Into an Erroneous Signal



Although the pendulum in Figure 1.6 remains parallel to its original orientation, its angular orientation relative to the housing has changed. The optical signal bouncing off of the pendulum will change position vertically on the detector. If the position-sensitive axis of the detector is not completely orthogonal to this translation, then the translation will be misinterpreted as a change in the pendulum's angular orientation. The phantom rotation for a pendulum mirror with a detector misaligned by an angle, θ_d , together with (relative to the housing) θ_{pxs} , that correlates with the movement of the source mass, will be:

$$\delta \theta_{z_{apparent}} = \theta_d \theta_{pxs} \quad (1.2)$$

For a detector misaligned by 10 mrad (about 35 minutes of arc) and a pendulum tilt (correlating with the signal) of 1 μ rad, this would produce an apparent rotation of 10 nrad about the z-axis.

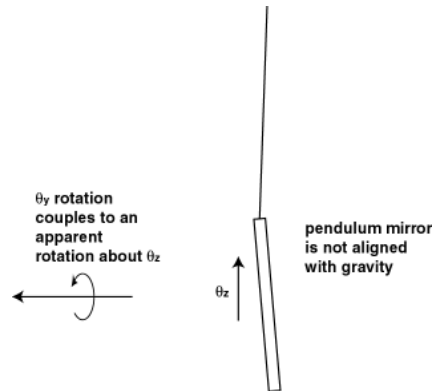
A rotation about θ_y would not be a problem if the mirrored face on the pendulum were normal to θ_y . If this were not the case, however, and the mirror were misaligned by an amount θ_{xp} , a θ_y rotation would produce a horizontal motion of the optical spot on the detector that would give a false signal. Note that, unlike the previous case, this effect does

not depend upon a misaligned detector. For a pendulum misaligned (about the x-axis) by an angle θ_{px} , and a tilt of the pendulum, correlated with the source mass, of θ_{pys} :

$$\delta \theta_{z \text{ apparent}} = \theta_{px} \theta_{pys} \quad (1.3)$$

A pendulum tilted 10 mrad about the x-axis, coupled to a signal-correlated tilt of 1 μ rad about the y-axis, for example, would produce an apparent rotation about the z-axis of 10 nrad.

Figure 1.7: Translation of θ_y Tilt into Measurement Error



A third way that tilt can correlate with a false signal is through the effect of electrostatic torques on a pendulum. As shown in Figure 1.6 (a), a tilt in the equipment housing the pendulum will move the pendulum relative to the housing. Any residual charges that are present on the surface of the housing will have created a set of mirror charges on the pendulum that depend upon the pendulum's position. In moving the pendulum (relative to the housing), these charges will rearrange themselves, changing the electrostatic torque that they exert upon the pendulum.

A similar problem is associated with gravitational and magnetic torques from the experimental housing, as a relative change in the position or tilt of the pendulum will

change the magnitude of these torques. All of the effects described above can create systematic measurement errors if correlated with a modulation of the gravitational source mass. Even if uncorrelated, these effects can degrade the precision of an experiment by contributing to background noise.

Variations on the static method are also sensitive to tilt error. In an “electrostatic compensation” measurement, an electrostatic torque is applied to the (grounded) pendulum. An optical feedback loop ensures that the pendulum does not move, relative to the housing. The electrostatic torques applied to the pendulum actively compensate for any external torques during a data run. Because the feedback loop does not actually hold the pendulum in one position, but instead holds a reflected optical spot in one position, it is subject to the same errors as a traditional static experiment.

In another variation of the static method, “inertial compensation,” no compensating torque is applied. Instead, the pendulum hangs within its housing, on a rotating platform. The platform, in turn, is made to accelerate or decelerate, at a rate such that the torsional angle between the pendulum and its housing does not vary. This acceleration is controlled by a feedback loop, using the optical lever as a reference. When the source masses are in place on the housing, both the pendulum and the housing will begin to rotate at constant acceleration, and by measuring that acceleration, the strength of the gravitational torque is inferred. This setup is less sensitive to tilt than a standard deflection experiment, because any tilt or ambient torque would have to rotate with the pendulum in order to have a systematic effect on the measurement.

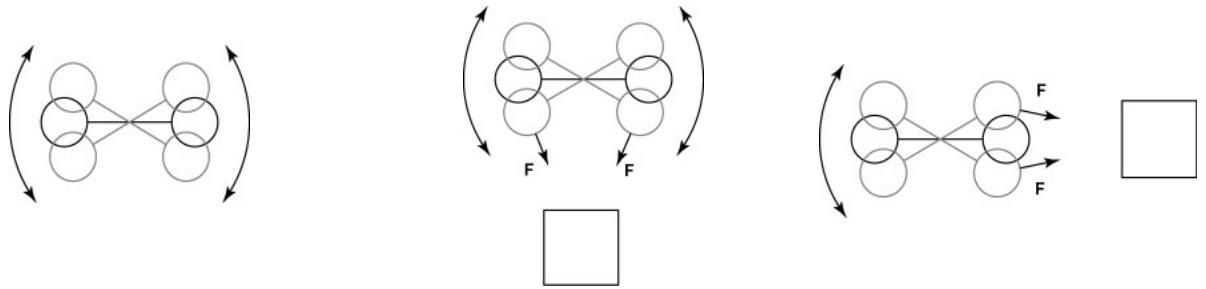
An inertial compensation experiment has its own unique difficulties. For instance, if the pendulum is not perfectly centered, a rotation of the apparatus will displace the

pendulum relative to the apparatus, causing it to swing. Accelerating apparatus rotation will eventually cause the pendulum to become displaced (relative to the apparatus frame) as a result of centrifugal forces.

The Dynamic Method

As discussed previously, in a “dynamic,” or “time of swing” measurement, the pendulum oscillates while data is taken. A gravitational torque is applied, and this changes the frequency of oscillation. This change in the frequency of oscillation indicates the interaction strength.

Figure 1.8: Dynamic Method (Top View)



a. No Source Mass
 $\omega^2 = \omega_0^2$

b. Source mass
 lowers oscillation
 frequency for
 small A
 $\omega^2 = \omega_0^2 - \Delta \omega^2$

c. Source mass
 raises oscillation
 frequency for
 small A
 $\omega^2 = \omega_0^2 + \Delta \omega^2$

If the net average torque from the source mass (over one period) acts to restore the pendulum to its equilibrium position, then the frequency is increased, as though the fiber's restorative torque had increased. On the other hand, if the net average torque acts to resist a

return to equilibrium by the pendulum, then the frequency is decreased, as though the fiber were slightly less stiff.

Determination of the oscillation period in the dynamic method is relatively straightforward. As with the static method, an optical lever measures the angle of the pendulum. As the pendulum rotates and the imaged, reflected beam crosses a particular position on a detector, the time is recorded (I will call this event a “crossing” or “zero crossing”). The intervals between this crossing and subsequent crossings are used to determine the oscillation period.

Tilt in the Dynamic Method

Unlike the static method, the dynamic method is relatively insensitive to tilt. This is because a tilt-induced mismeasurement of the pendulum's angle should not affect a measurement of the interval between crossings.

Any tilt of the housing can only affect the crossing time by a fixed amount, Δt . Because this will affect all subsequent crossings equally, it will not affect the measured frequency during a time interval during which the tilt does not change. It would only shift the zero crossing by a constant amount for all zero crossings, and any constant-time offset will have no effect. Thus, even if the apparatus or pendulum has a tilt that correlates with the source mass position, the period measurement will not be affected.

A Variation of the Dynamic Method : The Second Harmonic method

As described in Appendix C, local perturbative gravitational fields not only change the frequency of oscillation of the oscillator, they also create higher frequency harmonics in

the pendulum's motion. These harmonics will change sign with a modulation of the source mass. A gravitational method could be set up to detect these harmonics, by measuring $\theta(t)$ at several points during each cycle, using a fitting routine to extract the harmonics, and correlating the signal to that portion of the harmonics that modulate with the source mass. As of the date of publication of this dissertation, the author is not aware of any measurement of G having been performed using this method.

Chapter 2

Principles of the UCI G Measurement Approach

While every torsion pendulum gravitational experiment will have certain features in common, there are a number of key features of this particular measurement that are either unique among gravitational experiments, or else uncommon enough to merit mention and explanation. These include:

- Ring-shaped field source masses
- A flat, thin pendulum
- Several large torsional oscillation amplitudes
- Variation in types of fibers during the experiment
- Cryogenic temperatures

Ring-shaped field source masses

Placed at a particular separation distance, the ring-shaped source masses null all 3rd, 4th, and 5th spatial derivatives of their gravitational potential field at the midpoint of the rings' common axis. The result is that the source masses exert a torque on a pendulum placed near the rings' spatial midpoint which is extremely insensitive to error in the pendulum's position. This is explored further in Chapter 3.

Flat, thin pendulum

A flat, thin pendulum in the presence of the field generated by this ring configuration has a torsional oscillation frequency which is extremely insensitive to the pendulum's dimensions. Both this feature and the ring-shaped field source masses serve to greatly ease the demands for precision metrology. See chapter 3.

Large Torsion Amplitude

The torque from static field interactions can be expressed as a Fourier series of component torques that are periodic under a full rotation:

$$\tau = -\sum_m \alpha_m \cos(m\theta) - \sum_m \beta_m \sin(m\theta) \quad (2.1)$$

The minus signs are used to keep this equation consistent with the formalism discussed in Appendix C. For the UCI G experiment, these torques are zero by design through $m=5$, except for the component,

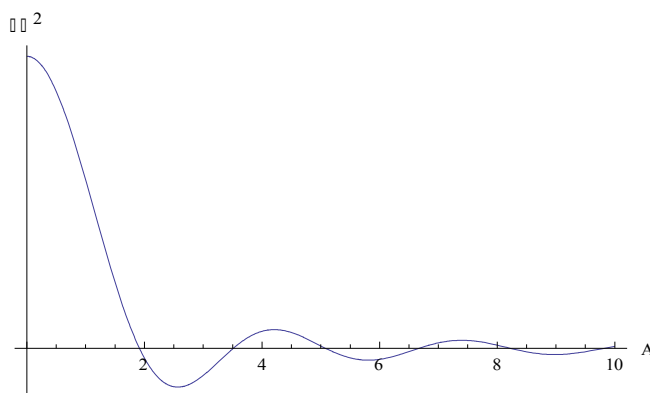
$$\tau_s = -\sum_m \beta_2 \sin(2\theta) \quad (2.2)$$

This torque is deliberately nonzero, and its effect on the frequency is the quantity measured in the UCI G experiment.

As the pendulum oscillates at large amplitude, it will experience regions of both positive and negative torque. The net effect is that the change in the square of the frequency, $\Delta(\omega^2)$, or simply “ $\Delta\omega^2$ ”, is related to the amplitude, A , by a Bessel function. As shown in Appendix 3, the signal will be proportional to the Bessel function, $J_1(2A)/A$:

$$\Delta\omega^2 = \frac{2J_1(2A)}{A} \frac{\beta_2}{I} \quad (2.3)$$

Figure 2.1: $\Delta\omega^2$ (Arbitrary Scale) vs. A (Radians) for the UCI Experiment



While the magnitude of the signal strength tends to decrease with increasing amplitude, operating at the extrema of the function yields good signal to noise ratio while ensuring minimal sensitivity to error in amplitude determination. See chapter 6 for more details. In addition, measurement of G based on operation at different amplitudes permits an important check of anelastic effects and other error sources.

Different Fiber Types

This provides another important check of fiber-dependent anelastic effects and other error sources. As described in further in chapter 4, the UCI G experiment uses Al 5056 fibers, heat treated CuBe fibers, and CuBe fibers as drawn.

Cryogenic Operation

The cryogenic aspects of the UCI experiment will help the measurement in several ways. Thermal noise torque, for instance, is proportional to $\sqrt{k_B T / Q}$, where Q is the mechanical quality factor of the oscillation. The experiment benefits here in two ways from

the cryogenic temperatures. Directly, the temperature itself is lower. Indirectly, the internal friction of the fiber is greatly reduced at low temperature, resulting in a much higher Q.

In addition, thermal control is better, as the experiment is submerged in a bath of liquid helium, fixing the temperature of the walls of the vacuum chamber. In addition, the materials used to fabricate the experiment are less sensitive to changes in temperature, this close to absolute zero. Variation of fiber torsion constant with temperature, and consequent variation in torsional frequency is an important source of noise in the dynamic method; thus, the reduced temperature sensitivity, coupled with the ability to maintain a highly constant temperature are of great benefit.

Furthermore, at low temperatures, cheap materials (such as the lead foil used in the UCI G experiment) become superconductive, so that ambient magnetic fields passing through a lead envelope will become “pinned,” shielding the pendulum from ambient magnetic field modulation.

Lastly, the low temperature helps to achieve an extremely high vacuum. First, materials will outgas much less at low temperatures, and second, any gases that do touch a cold surface are much more likely to stick to it, rather than bounce off. This helps to achieve very high vacuum in the region of the pendulum. Pressures as low as 10^{-7} mBar were measured at the room temperature portion of the vacuum chamber while the vacuum can was immersed in liquid helium, and the pressure in the low temperature region should have been much lower than this, although we did not have a device capable of measuring the pressure at such low temperatures.

On the down side, cryogenic equipment can be difficult to deal with. Opening up the experiment to fix problems becomes very time consuming, and many electronic devices do not function well at low temperatures.

Throughout any G experiment, it is vital to keep in mind, at all times, that the pendulum and source masses are not isolated from the rest of the universe, but are housed with, and measured, timed, modulated, and regulated by equipment that may itself introduce errors. These error sources include temperature variation, tilt, vibration, electrostatic interactions, magnetic interactions, wire cross-talk, digitization errors, computer program errors, etc. Some of these error sources are beyond the scope of this dissertation, but most are fully capable of introducing systematic errors sufficient to embarrass even an extremely capable scientist.

Chapter 3

Motivation for the Design of the Source Mass Rings and Pendulum

In the UCI experiment, a multipole formalism is used to extract G from the measured frequency shift produced by moving the source mass rings. Here, we briefly outline that formalism; details will be presented in chapter 6 and Appendix C.

The combined torque experienced by the pendulum from the restoring torque from an ideal torsion fiber plus the gravitational interaction of the pendulum with its environment may be expressed:

$$\tau(\theta) = -k\theta - \Re\left(\sum_{l=1}^{\infty} \sum_{m=-l}^l imq_{lm} a_{lm} e^{-im\theta}\right) \quad (3.1)$$

where k is the fiber's torsion constant and the q_{lm} and a_{lm} are respectively pendulum mass multipole moments and field multipole moments, defined in Appendix C. The frequency when the pendulum is placed in torsional oscillation is given by

$$\omega^2 \simeq \omega_0^2 \left[1 + \frac{2}{A} \sum_{m=1}^{\infty} J_1(mA) \frac{\beta_m}{k} \right] \quad (3.2)$$

where $\omega_0^2 = k/I$, I is the pendulum's moment of inertia, A is the torsional oscillation amplitude, and β_m is given by:

$$\beta_m = -2m \Re \sum_{l=m}^{\infty} q_{lm} a_{lm} \quad (3.3)$$

Equation 2 is accurate to first order in the ratio β_2/k .

The symmetry of the pendulum is such that $\beta_m = 0$ for odd m . The field moments a_{lm} and hence the β_m depend on the position of the source masses. When the ring field mass system is rotated about the pendulum's fiber axis by 90 degrees, β_2 and β_6 retain the same magnitude but reverse their sign, while β_4 is unchanged. Defining $\Delta_s \omega^2$ to be the change in the square of the torsional frequency when the ring source mass system is rotated by 90 degrees, we then find:

$$\Delta_s \omega^2 = \frac{4}{IA} [\beta_2 J_1(2A) + \beta_6 J_1(6A) + O(\beta_8)] \quad (3.4)$$

As the a_{lm} , and hence β_m , are each proportional to G , it is clear that equation 4 may be expressed in the form:

$$\Delta_s \omega^2 = C(A) \times G \quad (3.5)$$

so that G may be found:

$$G = \frac{\Delta_s \omega^2}{C(A)} \quad (3.6)$$

For the pendulum and source mass parameters of the UCI G measurement, the term proportional to β_6 in equation 4 represents a correction of only a few ppm to the dominant term proportional to β_2 . Thus in much of this thesis, the emphasis will be on error sources in determining β_2 , and the signal frequency shift will be normally approximated as:

$$\Delta_s \omega^2 = \frac{4}{IA} \beta_2 J_1(2A) \quad (3.7)$$

The source masses and pendulum used in the UCI G measurement have a variety of geometric properties designed to minimize sensitivity to error in mass and dimensional

metrology. The pendulum is thin and square, while the source mass consists of two rings, placed symmetrically on either side of the pendulum at a particular calculated separation.

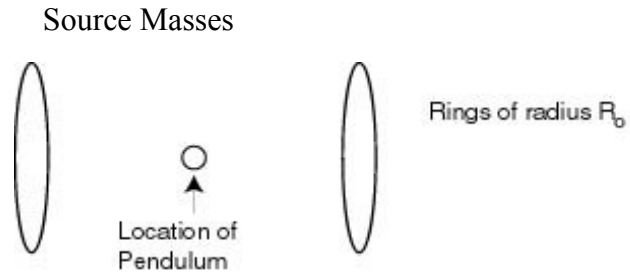
Ring Design

The UCI G experiment uses two copper rings as a source mass, designed to give a well-defined gravitational signal in the form of a change of frequency of oscillation.

A careful choice of ring geometry and separation can generate a gravitational potential whose spatial derivatives of order 1 and 3-5 vanish at a point midway between the rings. The remaining low order derivatives correspond to the gradient of \mathbf{g} – a field derivative that couples to the quadrupole moment of the pendulum. The vanishing of the next three derivatives means that the gradient of \mathbf{g} is nearly constant over a large volume. This makes the coupling of the source mass rings to the pendulum becomes extremely insensitive to error in the rings' placement.

In terms of the multipole formalism introduced in Appendix C, this nulling of derivatives corresponds to the nulling of field moments a_{lm} for $l = 1, 3, 4,$ and 5 , leaving only a_{22} . A particular ring spacing may be found which accomplishes this for rings of any width and outer and inner diameter. For rings of negligible cross-sectional size, the required separation between rings is $\sqrt{6+\sqrt{30}}$ times the radius of the rings, R_0 . The figures in the following discussion correspond to this special case.

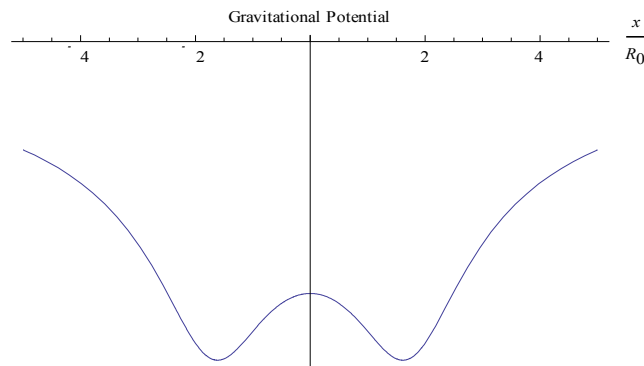
Figure 3.1: Model of Thin Rings



A convenient method to get a sense of the symmetry is to examine the gravitational potential along the axis of symmetry of the rings. This allows for a more intuitive exploration of the geometry than an a_m formulation might. Because the desired ring separation is proportional to the rings' radius, all of the following graphs will have an x-axis that is denominated in ratios to that radius.

Figure 3.2: Gravitational Potential of an Idealized Coaxial Two-Ring System, Along the Axis of Symmetry

(arbitrary vertical axis)

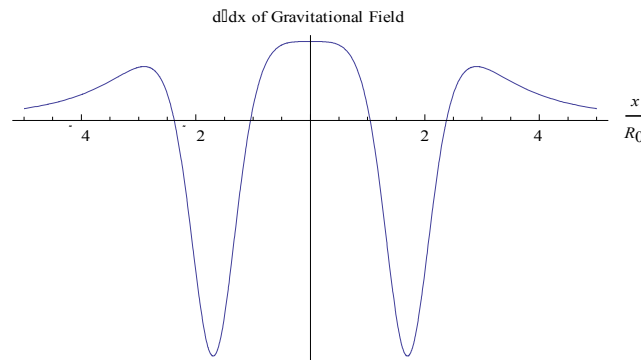


The gravitational potential cannot be directly measured, and the gravitational \mathbf{g} field

of the rings is zero at the midpoint (by symmetry). The leading measurable non-zero term is therefore the derivative of the field vector \mathbf{g} , and it is this term that is proportional to the experimental signal. The reason why is that we are measuring a quadrupole torque. A dipole pendulum moment would respond to the gravitational \mathbf{g} field. However, an important feature of any torsion pendulum is that it necessarily has no horizontal mass dipole moment relative to its suspension axis. Hence, only \mathbf{g} field derivatives contribute to the torque it experiences.

Figure 3.3: $\frac{\partial g_x}{\partial x} = -\frac{\partial^2 \Phi}{\partial x^2}$ of an Idealized

Coaxial Two-Ring System, Along the Axis of Symmetry
(arbitrary vertical axis)



Directly at the origin, the third, fourth, and fifth partial derivatives of the gravitational potential are all equal to zero. Odd derivatives are zero by symmetry, and the fourth derivative is nulled by the choice of ring spacing. This symmetry doesn't only apply to the x-coordinate. All derivatives of the potential field, of order 3 through 5, can be shown to vanish at the midpoint between the rings with the proper separation.

First, it should be realized that all y- and z- derivatives are interchangeable at the

origin due to symmetry, to all orders. Working from the fact that the Laplacian of the field is zero anywhere except on the one-dimensional rings, ie,

$$\frac{\partial^2 \Phi}{\partial x^2} + \frac{\partial^2 \Phi}{\partial y^2} + \frac{\partial^2 \Phi}{\partial z^2} = 0 \quad (3.8)$$

we can use the the symmetry in y and z to show:

$$\frac{\partial^2 \Phi}{\partial x^2} = -2 \frac{\partial^2 \Phi}{\partial y^2} = -2 \frac{\partial^2 \Phi}{\partial z^2} \text{ at the origin} \quad (3.9)$$

Consider the Φ_{xx} and Φ_{yy} terms from equation 9, and take their second derivative with respect to x.

$$\frac{\partial^4 \Phi}{\partial x^4} = -2 \frac{\partial^2 \left(\frac{\partial^2 \Phi}{\partial y^2} \right)}{\partial x^2} = -2 \frac{\partial^2 \left(\frac{\partial^2 \Phi}{\partial x^2} \right)}{\partial y^2} \text{ at the origin} \quad (3.10)$$

Combining the equations 10 and 9,

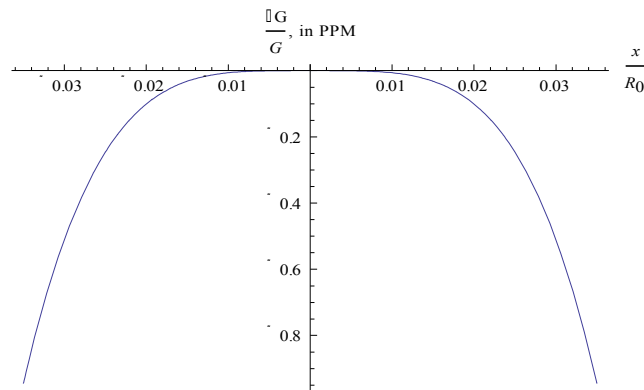
$$\frac{\partial^4 \Phi}{\partial x^4} = -2 \frac{\partial^2 \left(\frac{\partial^2 \Phi}{\partial y^2} \right)}{\partial x^2} = -2 \frac{\partial^2 \left(\frac{\partial^2 \Phi}{\partial x^2} \right)}{\partial y^2} = 4 \frac{\partial^4 \Phi}{\partial y^4} \text{ at the origin} \quad (3.11)$$

So not only is the fourth derivative of the field with respect to x equal to zero (by construction), but so is the fourth derivative of the potential field Φ with respect to y. By symmetry, this must be true of z as well, and any fourth derivative of the field constructed by some combination of x-, y-, and z-derivatives. By a similar technique, it can be shown that any odd derivatives of Φ (in any combination) are zero as well, as a result of the three components of the force being zero at the origin (due to symmetry).

Only at the sixth derivative of the field do we see a nonzero value. Because the gravitational interaction with the pendulum is proportional to the derivative of the vector field \mathbf{g} , and this derivative is nearly constant over a large volume, the gravitational

interaction and hence the determination of G is extremely insensitive to error in the pendulum placement. For the case of a thin ring explored here, the error in G due to an undetected error in placement of as much as 3.5% of the ring's radius would be less than 1 ppm.

Figure 3.4: PPM Error in G Arising from an Undetected Pendulum Position Misplacement along the x-axis



At this point the use of Cartesian coordinates in discussing the ring-pendulum interaction has reached the end of its usefulness, and any further consideration of the geometry should use the spherical harmonic formulation laid out in Appendix C. This allows for a more general approach, and one that can account for the more complex geometries that arise in physical situations.

Pendulum Design

The pendulum was designed to be relatively thin. Not only is a flat, thin pendulum easier to fabricate and measure, but it helps to minimize error in G associated with measurement errors. We have the following relation for the pendulum frequency shift generated by the ring source masses from Appendix C, equation C.11,

$$\Delta \omega^2 = \sum_{m=1}^{\infty} 2 \frac{\beta_m}{I} \frac{J_1(mA)}{A} \quad (3.12)$$

And, from Appendix C, equation C.30,

$$\beta_m = - \sum_{l=m}^{\infty} 2 m \Re(q_{lm} a_{lm}) \quad (3.13)$$

where the a's represent the gravitational field of the source mass, and the q's represent the responsiveness of the test mass. If the gravitational source masses are fabricated and oriented in such a way that the signal is dominated by a real a_{22} term, equation 12 can be expressed as

$$\Delta \omega^2 = -8 \Re\left(\frac{q_{22}}{I}\right) a_{22} \frac{J_1(2A)}{A} \quad (3.14)$$

It is the pendulum's geometry that is of interest to us here, so dropping all other factors from equation 14, we see that:

$$\Delta \omega^2 \propto \frac{\Re q_{22}}{I} \quad (3.15)$$

The moment, q_{22} , has been defined such that:

$$\begin{aligned} q_{22} &= \int \rho(\mathbf{r}) r^2 Y_{22}^*(\theta, \phi) d\mathbf{r} = \sqrt{\frac{15}{32\pi}} \int \rho(\mathbf{r}) (x - iy)^2 dV; \\ \Re(q_{22}) &= \sqrt{\frac{15}{32\pi}} \int \rho(\mathbf{r}) (x^2 - y^2) dV \end{aligned} \quad (3.16)$$

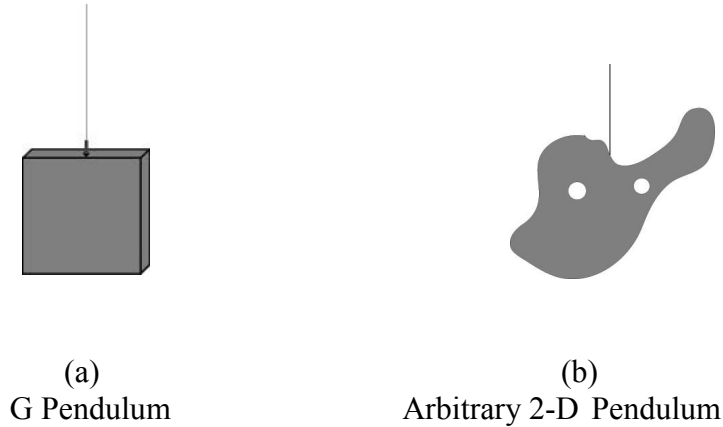
Dividing by the moment of inertia,

$$\begin{aligned} \Re\left(\frac{q_{22}}{I}\right) &= \sqrt{\frac{15}{32\pi}} \frac{\int \rho(\mathbf{r}) (x^2 - y^2) dV}{\int \rho(\mathbf{r}) (x^2 + y^2) dV} \\ &\rightarrow \sqrt{\frac{15}{32\pi}} \frac{\int \rho(\mathbf{r}) x^2 dV}{\int \rho(\mathbf{r}) x^2 dV} = \sqrt{\frac{15}{32\pi}} \text{ as } y \rightarrow 0 \text{ over the volume} \end{aligned} \quad (3.17)$$

For a flat two-dimensional pendulum with a normal vector that is perpendicular to the fiber axis, this ratio approaches a constant as the thickness approaches 0. At that limit,

any geometry will suffice. A two-dimensional pendulum shaped like Figure 3.5 (b) will experience the same change in frequency squared ($\Delta\omega^2$) in the presence of a uniform gravitational field gradient as any other flat two-dimensional shape would.

Figure 3.5: Pendulum



In addition to making the pendulum flat and thin, a deliberate choice of width-height ratio can also have an important effect upon the pendulum's behavior. While any geometry will give the same frequency shift in the presence of a gravitational potential of constant gradient, not all pendulums will respond equally to fields with non-zero higher derivatives.

Another geometric choice to consider is a pendulum designed to null the pendulum's q_{42} moment. This was the approach taken by Gundlach et al [7]. Expressed in Cartesian coordinates,

$$q_{42} = -\frac{3}{8} \sqrt{\frac{5}{2\pi}} \int \rho(\mathbf{r})(x-iy)^2(x^2+y^2-6z^2) dV \quad (3.18)$$

For a geometrically perfect, rectangular pendulum, for example, this moment is zero when the dimensions obey the following relation:

$$height = \sqrt{\frac{3}{10} * (thickness^2 + width^2)} \quad (3.19)$$

For a perfectly thin pendulum, this means that the height is about 55% of the width. This

will complement any nulling of the a_{42} produced by a careful choice of source mass geometry, described above.

Alternatively, one could choose to null the pendulum's q_{62} moment through a similar method, resulting in a choice of pendulum height that obeys one of the following relations:

$$height = \sqrt{\frac{thickness^2}{2} + \frac{width^2}{2} \pm \frac{\sqrt{13 thickness^4 + 34 thickness^2 width^2 + 13 width^4}}{4\sqrt{7}}} \quad (3.9)$$

For a thin pendulum, this means that the height is approximately either 92% or 40% of the width.

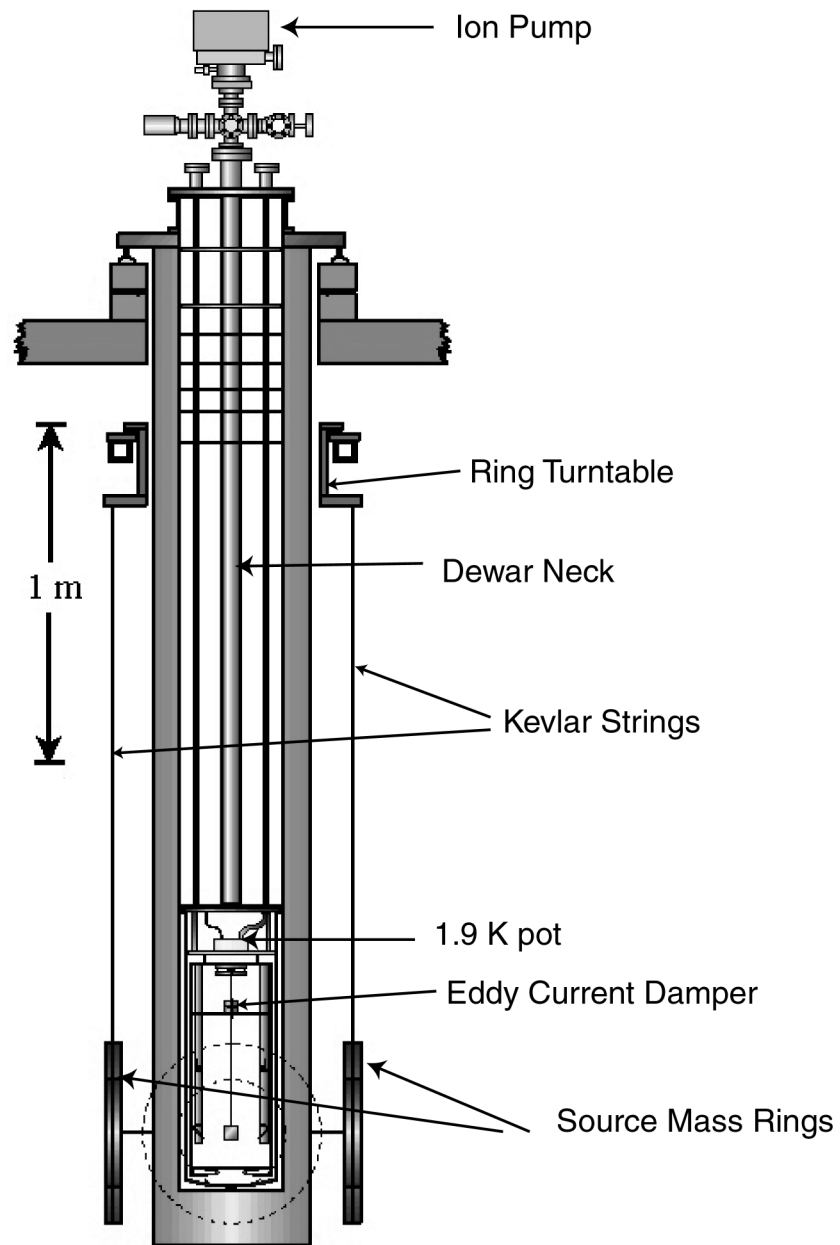
For a well-designed double ring shaped source mass, the $q_{62}a_{62}$ term is likely to be the leading nonzero quadrupole correction to the $q_{22}a_{22}$ term, so this geometry might be favorable for some G experiments.

Chapter 4

The Experimental Apparatus

This chapter describes the key components of the experimental apparatus used in the UC Irvine measurement of G .

Figure 4.1: The Cryostat (Courtesy of Mike Bantel)

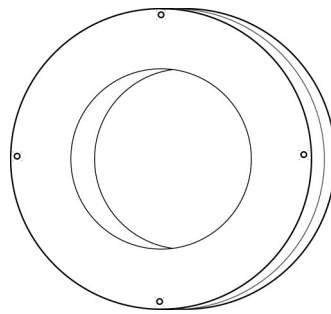


Source Mass Rings

The gravitational source masses are cylindrical copper rings, with inner diameter of 31.242 cm, an outer diameter of 52.07 cm, and a thickness of 4.826 cm. Each ring weighs approximately 58.93 kg, and is coated by an alloyed, non-magnetic layer of NiP8, an alloy

of nickel and approximately 9% phosphorous, $\sim 7.5 \mu\text{m}$ thick (the density is well matched to that of the copper, so the precise thickness is irrelevant; a 50% discrepancy in the thickness will give only a 0.5 ppm change in G, while the thickness is, in fact, known to about 25%). The rings are tapered by about $20 \mu\text{m}$ (ring 1) or $12 \mu\text{m}$ (ring 2), and both are slightly thicker at the outer diameter than the inner diameter. The total correction $\delta G/G$ from this tapering is approximately 24 ppm. Density varied throughout the ring's diameter by approximately 15 ppm. Assuming that this variation is linear from one side of the ring to another, it would give a $\delta G/G$ of approximately 0.2 ppm (with small variations that depend upon the ring's orientation). Due to symmetry, radial density variations (those that do not vary with azimuthal angle) do not produce first-order changes in ring field moments, and can be ignored. The inner and outer ring edges have chamfers of projected width 0.62mm.

Figure 4.2: Copper Source Mass Ring (one)

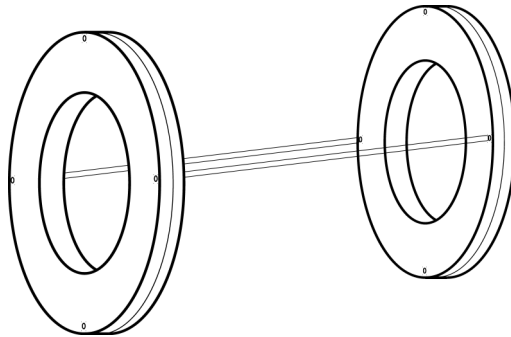


The rings are suspended 1.87 meters below the bottom of the turntable by Kevlar string of linear density 1.4 g/mm, which wraps around the bottom of each ring, and back up to a mount, constrained by an azimuthal groove in the outside of each ring 1.25 mm wide and 1.25 mm deep. The two Kevlar string mounts for each ring are located approximately 17.5 cm apart. In order to maintain the separation between the two rings, two rods of fused

silica are placed between them, parallel to the rings' axis of symmetry, and at the same height as the axis of symmetry, 25.019 centimeters from the (horizontal) axis of symmetry. Each rod is 65 cm long and 8 mm in diameter, with a density of 2.2 g/cm^3 . In order to accommodate the spacer rods, each ring has 8 circular 5mm diameter and 1 mm thick sapphire plates weighing 75.7 mg each, glued into accommodating holes of 6mm diameter. Each window has approximately 13 mg of glue (based on volume and density measurements). There are 4 windows on each face of each copper ring, placed at the same azimuthal angle relative to each other. The plates are in place to prevent the spacers from digging or grinding into the rings, or simply pushing into the rings elastically.

Surrounding each sapphire plate are 4 holes of diameter 1.6 mm and depth 3.6 mm for up to four Delrin pins (9.5 mm long and 24.7 mg each) to constrain the placement of the rods and prevent them from slipping. The two rings are separated by a face-to-face distance of 65 cm and are oriented coaxially.

Figure 4.3: Rings with Constraining Rods



The redundant sapphire windows allow four 90 degree rotations about each ring's symmetry axis, and one 180 degree rotation around a vertical axis, in order to average over

mass distribution asymmetries using successive data sets taken with different ring orientations.

In order to measure the temperature of each ring, platinum thermometers were placed in each ring with grease, for a total mass of 80 mg for the platinum thermometer plus grease. They were affixed in a 2mm diameter hole 6.35 mm deep on the outside rim of each ring, 45 degrees azimuthally from the sapphire windows.

A turntable allowed for changes in the ring height and adjustment of the ring orientations. The ring modulation software was carefully calibrated to ease the rings into position quickly (roughly 1-2 minutes per transport) and with minimal swinging, although there was always some residual ring oscillation remaining. A laser beam reflected by a small mirror mounted on one of the rings to a two-axis position sensor served to sense residual swing motion of the rings following their periodic repositioning. The entire mirror and mount assembly weighed 261 mg, with a center of mass approximately 3.5 mm from the outer edge of the ring. The reflected laser beam was used by the software to control small rotations of the turntable from which the rings were suspended in order to damp the swing motion. Ring position consistency was maintained between successive ring modulations with the data from a separate set of lasers reflected off of mirrors on the turntable.

Had this action not been taken, the swinging rings would have systematically applied a smaller than expected net torque on the pendulum. As shown in appendix C, a relative rotation ϕ between the pendulum and the source mass results in a sinusoidal change in the torque; for a β_2 -dominated interaction, this goes as $\text{Cos}(2\phi)$ or, for small rotations,

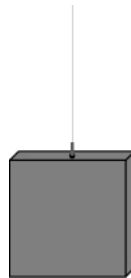
$d(\log \beta_2) = -2 \phi^2$. A pair of rings swinging in this fashion would require a time average of the torques applied to the pendulum.

The Pendulum

The pendulum used in the G experiment is approximately a square, 40 mm by 40 mm, and 3 mm thick, weighing 10.9 g.

The pendulum is composed of fused silica (Corning 7989-OAA, density 2.2006 g/cm³), coated with a layer of aluminum (100 nm ± 10nm) + SiO₂ (27nm ± 2.7 nm). The 2004 and 2006 data added a layer of chromium (5 nm) plus a layer of gold (200 nm ± 20 nm). At the top of the pendulum is a hole, 1mm in diameter and a depth of 4 mm, into which is glued a brass screw weighing 42 mg ± 3 mg. The glue used was on the order of 1.4 mg of Stycast 1266. Each edge of the pendulum had a chamfer, approximately 0.44 mm wide.

Figure 4.4: The UCI G Pendulum



As described in chapter 3, the pendulum is designed to be as thin as is practical in order to minimize the sensitivity to machining and metrology errors of the ratio of the signal

sensitivity to the moment of inertia, q_{22}/I . Its two-fold symmetry nulls the value of the Newtonian moments, q_{lm} , for odd m .

Unfortunately, one of the pendula, during a gold coating process, was damaged. A chip of fused silica (and the accompanying coating) broke off during the coating process, and the repaired pendulum was later used in the 2004 data runs.

Fibers

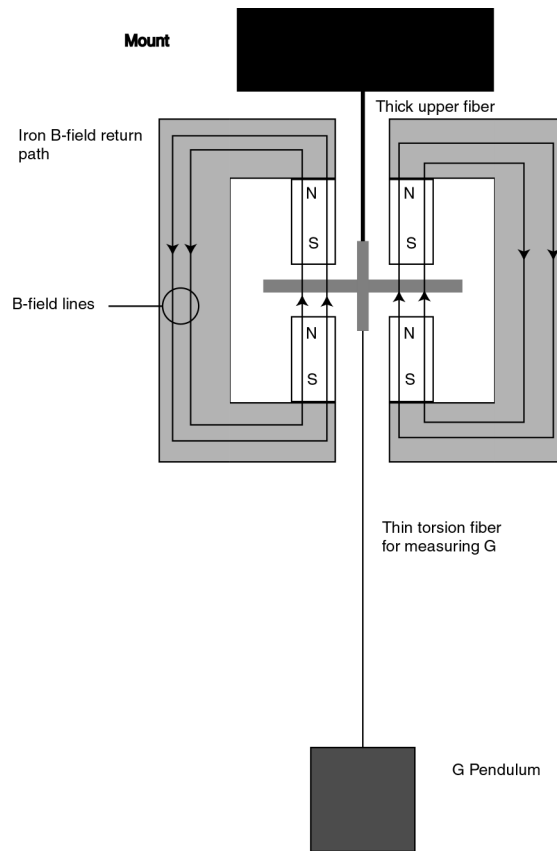
The UCI G experiment used three different fibers in order to procure a range of data under different values of Q , with different anharmonic torque strengths, and for different materials. The first type of fiber was a copper beryllium (CuBe) fiber. The second type was a CuBe fiber that was then heat treated at 320 C for approximately 8 hours, then cooled at a rate of 30 C per hour to room temperature.

The fibers varied in length but were approximately 25 cm long. At each end, the fiber was glued into a mount consisting of a hand-cut length of aluminum tubing (approximately 2 cm long) using Stycast 1266 epoxy. For further details, see Bantel [18]

Eddy Current Swing Mode Damping System

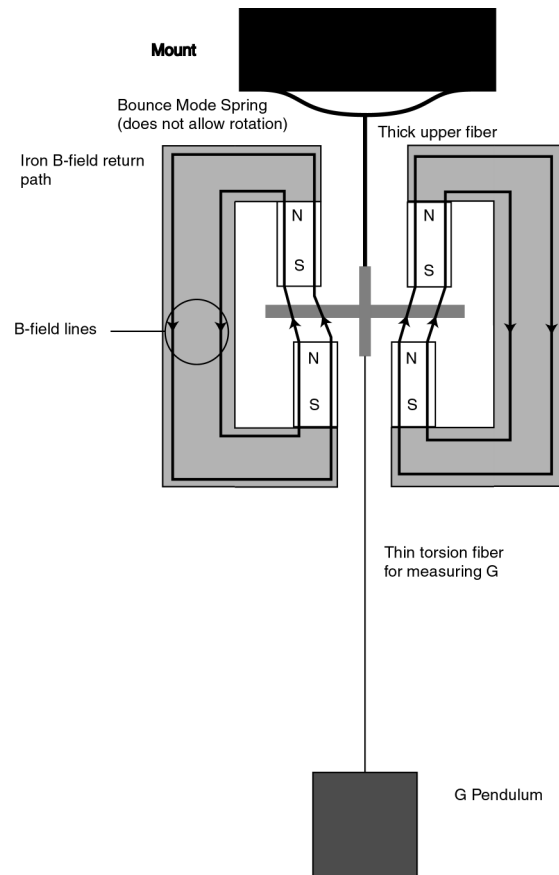
In order to quickly damp swing mode oscillations of the pendulum, the apparatus was built with an eddy current damping system, with magnetic fields bridging the vacuum gap between the top and bottom portions of the device. The damper uses a two-stage pendulum suspension, with a stiff upper fiber that will flex if the G pendulum is swinging but will not allow significant rotation at expected amplitudes.

Figure 4.5 Cross Section of an Azimuthally Symmetric
Swing Mode Eddy Current Damping Device



In addition to swing modes, the pendulum has an oscillatory degree of freedom in which it may “bounce” up and down, stretching its torsion fiber. Such oscillation can couple nonlinearly into a torque on the pendulum which could be a source of systematic bias. To damp this bounce mode, we experimented with the modified eddy current damping system shown in Figure 6. A spring was added to allow the eddy current damping disk to oscillate vertically, and the magnet shape was altered.

Figure 4.6: Swing and Bounce Mode Eddy Current Damper



This system was tested with a 240 gram pendulum designed for future planned experiments, but failed to reduce observed noise levels.

Vacuum System

The stainless steel vacuum can has an OD of 27.3 cm, an ID of 26.6 cm, and 78.7 cm of full ID (with rounded bottom). The vacuum chamber has a long neck, 5.1 cm in diameter and 205 cm long from the top of the vacuum can to the top plate of the insert. During data runs, the helium level is somewhere above the top of the vacuum can but below the lowest of seven baffles, approximately 1.2 meters above.

The vacuum in the region of the G pendulum is achieved through a multi-stage process. After the vacuum chamber is sealed, it is pumped down using a turbo pump (Varian Turbo-V70) backed by a diaphragm pump (Varian VS102). The turbo pump/diaphragm pump combination was chosen in order to avoid oil migration into the vacuum chamber.

When the pressure drops low enough, ($\sim 10^{-5}$ mbar), an Varian triode 20 l/s ion pump is engaged to bring the pressure down to approximately 10^{-6} mbar. When the dewar is filled with liquid helium, the pressure drops further through molecular adhesion to any cold surface. This effect is exploited with several cubic centimeters of activated charcoal in the vacuum chamber. After being exposed to atmosphere, this charcoal was heated during its initial exposure to vacuum in order for it to outgas.

At the location of the ion pump (at the top of the apparatus and at room temperature), the cryopumping is able to generate a vacuum on the order of 10^{-7} mbar. This room-temperature pressure is likely to be orders of magnitude larger than the pressure at the location of the pendulum.

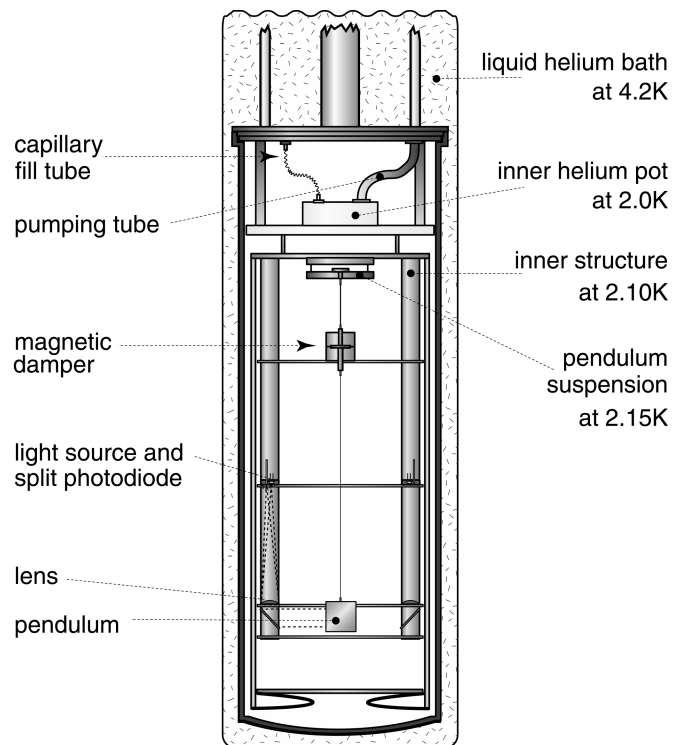
During the 2000, 2002, and 2004 data runs, the ion pump was usually on while data was being taken. During the 2006 data runs, the ion pump was normally turned off, and we relied on the activated charcoal cryopump action to maintain high vacuum for the pendulum, as it was suspected that the ion pump contributed to a noisy readout signal coming from the photodetector. There were also fears that the ion pump was burping gas into the vacuum system, although this was never rigorously investigated.

“2K” Helium Pot

To further reduce the operating temperature of the pendulum, and to facilitate temperature control, the cryostat includes a chamber (“2 K pot”) into which helium is drawn from the 4.2K reservoir through a capillary tube. By pumping this pot to pressures of a few mbar, its temperature may be reduced to 1.9K with our system (others have gotten to 1K and below). Unfortunately, these systems typically suffer from capillary flow rate oscillations which were later suspected of contributing to statistical noise through mechanical vibration.

Figure 4.7: The Vacuum Can of the Cryostat

(Courtesy of Mike Bantel)



Although the 2K pot was used for the entire G experiment, it will not be used in future experiments, and we cannot recommend its use in future gravitational cryogenic torsion pendulum experiments.

Temperature Control System

Weakly thermally coupled to the 2K pot is a platform equipped with a Ge thermometer and heater which are used in a PI (proportional – integral) control system to maintain this stage at a constant temperature a few tenths of a degree above that of the 2K pot. This stage is thermally coupled to a cylindrical aluminum shield (the “cold can”) which surrounds the pendulum's support structure. Within this shield, a final temperature control stage is weakly thermally coupled to the preceding stage, and is equipped with its own thermometer, heater, and a PI temperature control system. Together these elements form a four stage temperature control system.

Table 4.1: The Four Stages of Temperature Control for the UCI G Experiment

Stage	Description
0	the 4.2K thermal bath of the main thermal reservoir
1	the 2K pot, with temperature controlled via pressure control in a PI system for some data runs
2	weakly coupled to stage 1, with its own PI temperature control
3	weakly coupled to stage 2, with its own PI temperature control

Stage 3 has two thermometers: T3, which is used in this stage's control loop, and T4, which is mounted in the copper element to which the upper pendulum fiber is mounted. T4 serves to monitor the cumulative performance of the various temperature control loops, and also provides a measure of the temperature of the fiber for use in estimating systematic error from fiber temperature variation.

Throughout the G experiment we attempted to use the stage 1 temperature control by modulating the pressure on the helium pot pumping line, although it periodically would

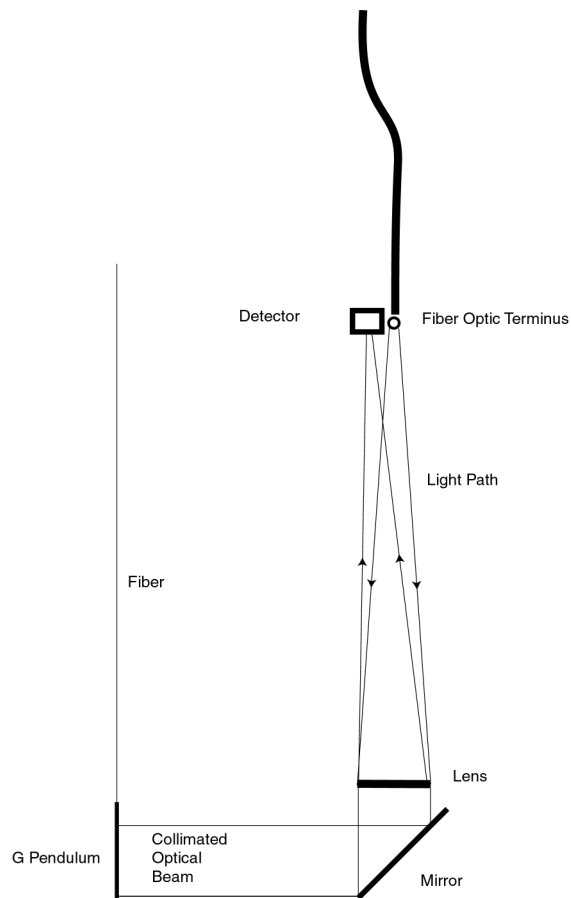
deviate drastically from desired temperature ranges.

In addition to heat entering the system from the control loop heaters, a fraction on the order of 10% of the optical lever light is absorbed by the pendulum. The pendulum was coated with a thin layer of gold after the 2004 data run in order to increase the reflectivity (78% for the Aluminum coating, 98.7% for the gold coating).

Optics System

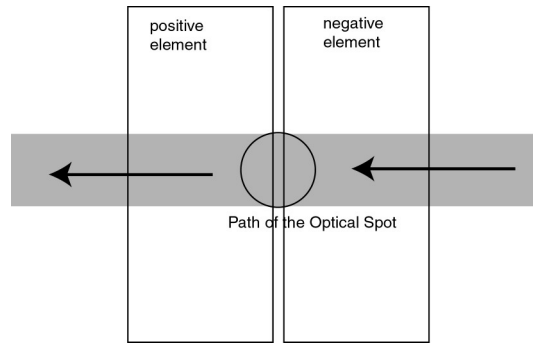
In order to measure the period of the pendulum, as well as the higher harmonics of its oscillation, the pendulum is imaged using an LED at room temperature, with a fiber optic cable to transport the light through the helium bath and into the vacuum system. The LED used was a Honeywell HFE 4226-022 850 nm GaAlAs, mated to a 62.5 μm fiber delivering approximately 100 μW of 850 nm light at 60 mA of input current. When the light exits the fiber optic cable, it is collimated using a 163mm focal length lens, aimed at the G pendulum with a 45-degree aluminum coated mirror (reflectivity of $\sim 90\%$), and reflected off of the G pendulum. If the reflective surface of the G pendulum is perpendicular to the beam column, it is reflected back towards the 45 degree mirror, and refocused by the collimating lens onto its split photodetector. See Figure 8.

Figure 4.8: Optical Focusing during a Zero Crossing



As the pendulum face aligns with the mirror, the imaged spot sweeps across the split photodetector, 1mm x 2 mm total area, with a 50 μ m gap. For a period of 135 seconds (depending on the fiber being used) and an amplitude of 2.57 radians, the optical spot will take 2.56 ms to cross the 1mm wide photodetector. See Figure 9.

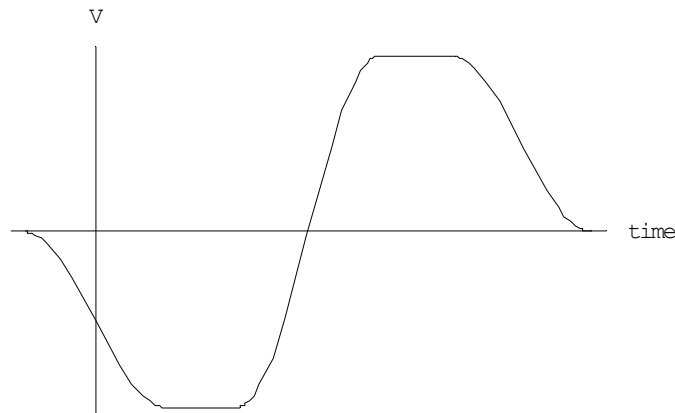
Figure 4.9: Detector during a Transit



The photodetector (a CentroVision LD2A-0; peak current 10 mA, 0.54 A/W response at 900 nm) fed current to an amplifier that typically consisted of a pair of Burr Brown (now Texas Instruments) OPA627 op amps as “transconductance” (current-to-voltage) amplifiers, with feedback components 1.8 Mohm in parallel with 12 pF. These go to an INA110 differential amplifier, set for unity gain.

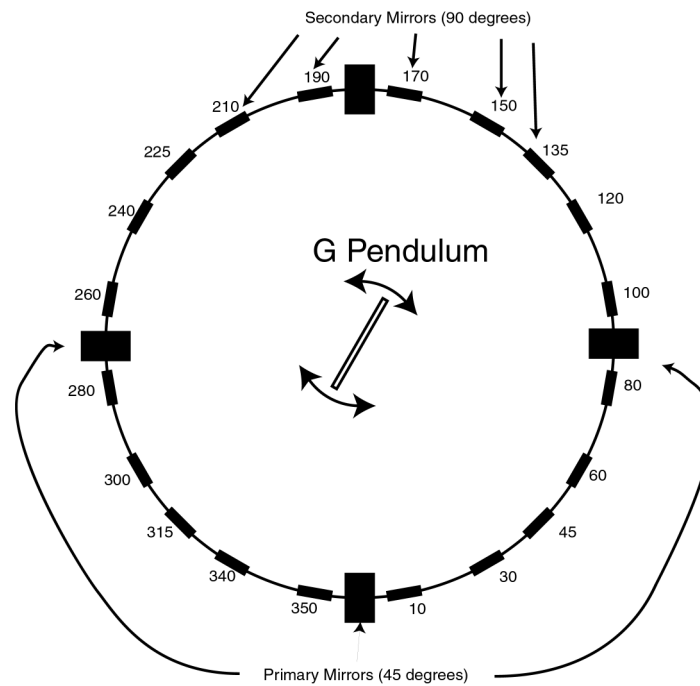
Each face of the photodetector generates a current that is converted into a voltage by a resistor and summed using this setup. The moment at which the summed voltage becomes zero is called a “zero crossing.” See Figure 10

Figure 4.10: Summed Photodetector Voltage during a “Zero Crossing”



Digitizations in the central region are used to construct a third-order fit, and the time at which $V=0$ in this fit is recorded and used to determine the frequency of the pendulum. In order to obtain information about the pendulum's behavior at other angles, 90 degree aluminum mirrors (reflectivity $\sim 90\%$) are set up in a ring around the pendulum, as shown in Figure 11.

Figure 4.11: Placement of 4 Primary (45 degree) and Secondary (90 degree) mirrors around the UCI G Pendulum



Although Figure 11 shows four redundant 45 degree mirrors, only one was used in G data run.

When the collimated beam reflects off of its corresponding 45 degree mirror and then the surface of the G pendulum, it may also reflect off of a secondary mirror. If so, it will reflect back to the UCI G pendulum, and from there to the primary mirror, through the

focusing lens, to be imaged at the photodetector. This enables the measurement of specific times when the pendulum passes through these angles, permitting greater characterization of the pendulum's oscillation than one would achieve with only the central crossing.

Timing System

The period of the oscillating pendulum during the UCI G experiment could be as little as approximately 100 seconds or as much as 135 seconds depending on the fiber being used. The signal change in period when the ring system was rotated was at most 1.7 ms (for the as-drawn CuBe fiber at 2.57 radian amplitude) and as small as 0.2 ms (for the A15056 fiber at 7.4 radian amplitude). Thus, measuring G to 10 ppm required measuring the oscillation periods with accuracy as great as 2 parts in 10^{11} .

In order to achieve this level of precision, we use an HP 58503B GPS-steered crystal controlled time base, which generated a highly accurate and stable 10 MHz sine wave signal. This signal is converted to a square wave that is used as the digitization timebase of a National Instruments data acquisition card (PCI-MIO-16-1: 12 bit 1.25 million samples/second). The card uses the counter and the voltage input to feed information on transits to the computer, which fits the data and logs the transit.

Lab Site

The experiment takes place at a location roughly 10 meters underground, in a former NIKE missile launch site on the Hanford reservation in the desert of the eastern part of the state of Washington. The closest publicly accessible road is approximately 5 miles from the site, minimizing seismic noise pollution from automobiles and humans.

Chapter 5

Further Formalism in a Dynamic Measurement of Gravity

In chapter 3 we outlined the basic formalism for extracting a value of G from frequency shift measurements in the UCI G experiment. That discussion assumed that the only torques acting on the pendulum were those due to an ideal torsion fiber and an ideal gravitational source mass. In this chapter, we extend that formalism to take into account non-ideal fiber properties as well as external torque sources such as background gravitational fields and magnetic fields.

In order to describe the behavior of a torsion pendulum, it is useful to subdivide the forces (or rather, the torques) acting on the pendulum into several different categories, and to characterize the response of the pendulum to each of these categories. The equation of motion of the torsional pendulum will be:

$$I \ddot{\theta} = \tau \tag{5.1}$$

where τ may be expressed:

$$\tau = - \left\{ \sum_n k_n \theta^n + \sum_i \tau_i(\theta, \dot{\theta}) + \sum_m [a_m \cos(mq) + b_m \sin(mq)] \right\} \tag{5.2}$$

where the first sum represents elastic torques generated by the fiber, the second sum represents dissipative torques, and the third sum represents torques generated by pendulum couplings to external static fields. We will consider each of these torques in turn.

It is convenient to think of a torsion pendulum's behavior (in the presence of only the torque of an ideal fiber) as that of a simple harmonic oscillator:

$$I \ddot{\theta} = -k_1 \theta \quad (5.3)$$

Solving the equation of motion, we find that (for an appropriate choice of $t = 0$):

$$\begin{aligned} \omega_0 &= \sqrt{\frac{k_1}{I}} \\ \theta_0(t) &= A \sin(\omega_0 t) \end{aligned} \quad (5.4)$$

Conservative Torques Generated by the Pendulum Suspension Fiber

A precision experiment will reveal that, rather than behaving as equations 3 and 4 suggest, there is in fact a much more intricate behavior to the pendulum oscillation induced by the fiber,

$$I \ddot{\theta} = \tau_{fiber}(\theta, \dot{\theta}) \quad (5.5)$$

The fiber torque can be subdivided into two categories: the first consists of conservative torques, which do not dissipate energy and do not depend upon angular velocity, and the second consists of energy dissipative torques which do depend upon angular velocity.

$$\tau_{fiber}(\theta, \dot{\theta}) = \tau_{f, cons}(\theta) + \tau_{f, diss}(\theta, \dot{\theta}) \quad (5.6)$$

Considering just the conservative torques, equation 3 can be rewritten:

$$I \ddot{\theta} = -k_1 \theta - k_2 \theta^2 - k_3 \theta^3 - \dots - k_n \theta^n - \dots \quad (5.7)$$

The case where k_1 dominates this behavior has been solved in Appendix B. The pendulum's motion is found to be of the following form, where the frequency ω and coefficients A , a_n , and b_n are given to first order in the ratios k_n/k_1 by:

$$\theta(t) = A \sin(\omega t) + a_0 + \sum_{m=2}^{\infty} a_m \cos(m \omega t) + b_m \sin(m \omega t) \quad (5.8)$$

then the solution will take on the following values:

$$\frac{\Delta \omega^2}{\omega_0^2} = \sum_{n=3,5,7,\dots}^{\infty} \left(\frac{1}{2}\right)^{n-1} \frac{n!}{\left(\frac{n+1}{2}\right)! \left(\frac{n-1}{2}\right)!} A^{n-1} \frac{k_n}{k_1} \quad (5.9)$$

$$a_0 = - \sum_{n=2,4,6,\dots}^{\infty} \left(\frac{1}{2}\right)^n \frac{n!}{\left(\frac{n}{2}\right)! \left(\frac{n}{2}\right)!} A^n \frac{k_n}{k_1} \quad (5.10)$$

$$a_{m, \text{even}} = \sum_{n=m, m+2, m+4, \dots}^{\infty} \frac{1}{n^2 - 1} \left(\frac{1}{2}\right)^{n-1} (-1)^{\frac{m}{2}} \frac{n!}{\left(\frac{n+m}{2}\right)! \left(\frac{n-m}{2}\right)!} A^n \frac{k_n}{k_1} \quad (5.11)$$

$$a_{m, \text{odd}} = 0 \quad (5.12)$$

$$b_{m, \text{even}} = 0 \quad (5.13)$$

$$b_{m, \text{odd}} = \sum_{n=m, m+2, m+4, \dots}^{\infty} \frac{1}{m^2 - 1} \left(\frac{1}{2}\right)^{n-1} (-1)^{\frac{m-1}{2}} \frac{n!}{\left(\frac{n+m}{2}\right)! \left(\frac{n-m}{2}\right)!} A^n \frac{k_n}{k_1} \quad (5.14)$$

The first few terms (up through $m = 7$) in equations 9-14 can be seen in the table at the end of Appendix B.

During the exploration of second-order couplings (discussed in Chapter 6), these first-order terms for k_2 and k_3 have been checked against the results of numerical integrations in order to confirm their validity. Limits on computational accuracy of approximately 10^{-17} seconds and 10^{-17} rad put an upper limit on the uncertainty in the value given by equation 9 of less than 6 parts per billion. For this computation, k_1 was set to .032 dyn cm/rad, the period was set to 135 seconds, and k_2 and k_3 were set to $4.8 \cdot 10^{-5} k_1$.

There are a number of symmetries that appear in the oscillator's response to these conservative torques. First, the frequency is only affected by torques of odd n . Second, offsets are only produced by torques of even n . Third, odd n torques produce odd sine

harmonics, ie, a k_{13} term will produce harmonics of $\sin(13\omega t)$, $\sin(11\omega t)$, $\sin(9\omega t)$, etc. This is because the torque is an odd function of θ , and this makes the torque an odd function of t (since we have defined that $\theta(0)=0$ for the dominant harmonic). Similarly, the even character of even m torques will produce even cosine harmonics.

The second group of fiber torques consists of the dissipative torques that serve to damp the pendulum's motion. This consists of a vast parameter space of torques, only a few of which are potentially relevant to a measurement of G . Therefore, these will not be described here, but a few potentially relevant cases will be described in greater detail in chapter 6. Any torque that depends upon angular velocity, or the sign of the angular velocity, will fit into this category.

Conservative Torques Generated by Ambient Fields

Another set of torques that act upon the torsion pendulum is caused by the ambient static fields in the neighborhood of the pendulum. Because these torques are periodic under a full rotation, they can be represented by a Fourier expansion:

$$\tau = - \sum_{m=1}^{\infty} [\alpha_m \cos(m\theta) + \beta_m \sin(m\theta)] \quad (5.15)$$

These torques can be further subdivided into those that correlate with the motion of the source mass, and those that do not.

As with conservative fiber nonlinearities, these field torques produce changes in frequency, as well as harmonics. Start with the assumption that the oscillator's behavior is dominated by a simple harmonic oscillation. The solution will be presented in the same form as equation 8:

$$\theta(t) = A \sin(\omega t) + a_0 + \sum_{n=2}^{\infty} [a_n \cos(n\omega t) + b_n \sin(n\omega t)] \quad (5.16)$$

The first-order solutions are derived in Appendix C, and the results are reproduced here:

$$\frac{\Delta \omega^2}{\omega_0^2} = \sum_{m=1}^{\infty} 2 \frac{J_1(mA)}{A} \frac{\beta_m}{k_1} \quad (5.17)$$

$$a_0 = - \sum_{m=0}^{\infty} J_0(mA) \frac{\alpha_m}{k_1} \quad (5.18)$$

$$a_{n,even} = \sum_{m=1}^{\infty} \frac{2}{(n^2-1)} J_n(mA) \frac{\alpha_m}{k_1} \quad (5.19)$$

$$a_{n,odd} = 0 \quad (5.20)$$

$$b_{n,even} = 0 \quad (5.21)$$

$$b_{n,odd} = \sum_{m=1}^{\infty} \frac{2}{(n^2-1)} J_n(mA) \frac{\beta_m}{k_1} \quad (5.22)$$

As with the nonlinear fiber torques, the frequency shifts (equation 17) have been checked during exploration of second-order couplings of various torques on the frequency explored in chapter 6. Limits on computational accuracy of approximately 10^{-17} seconds and 10^{-17} rad put an upper limit on the error of the first order correction given by equation 17 to less than 1 part per billion. For this computation, k_1 was set to .032 dyn cm/rad, the period was set to 135 seconds, and the field torque terms were set to $4.8 \cdot 10^{-5} k_1$.

In equation 17, the fractional shift in frequency is of order of the small dimensionless parameter β_m/k_1 . In a dynamic measurement of G, all but one of the relevant gravitational torque terms will be small due to a careful experimental design (see chapter 3). That remaining torque term will dominate the signal. In the case of the UCI G experiment, this term is β_2 , and the measured change in frequency is expressed as

$$\left(\frac{\Delta\omega^2}{\omega^2}\right)_s = \frac{2J_1(2A)}{A} \frac{\beta_2}{k_1} \quad (5.23)$$

Several symmetries arise in equations 17-22. The a_n terms, for example arise from $\alpha_m \cos(m\theta)$ torques on the pendulum. Because

$$\cos(m\theta) = 1 - \frac{m^2\theta^2}{2!} + \frac{m^4\theta^4}{4!} - \dots \quad (5.24)$$

we would expect the a_n terms produced by α_m to have a symmetry similar to the symmetry produced by “even m ” θ^m terms, which is the case. Both produce only $\cos(n\theta)$ harmonics, with even n . Both are even functions of θ and of t . Both produce a change in the offset angle. A similar symmetry is produced by the $\sin(m\theta)$ torques. The harmonics produced by these terms are odd-integer sines, and are odd functions of θ and t . Like odd polynomial terms of θ , these $\sin(m\theta)$ terms affect the frequency of the oscillation.

Equations 17-22 form a general perturbative solution for all conservative field interactions: electrostatic, magnetostatic, and gravitational. Each field source will contribute its own set of α_m and β_m to the pendulum's motion, and any that correlate with the motion of the source mass will contribute to the measured frequency shift.

Higher Order Effects of the Torque Perturbation Terms

Equations 17-22 describe only the first-order effect of small perturbative field torques, and equations 9-14 are also only to first order. None of these indicate the magnitude of any second-order (or higher) effects. These effects arise because the pendulum's behavior deviates from that of a pure sine wave, and any alteration of the sine wave will slightly change the perturbing effects of all torques. Unfortunately, analytic

methods do not lend themselves to an easy exploration of higher order frequency perturbations. The magnitude of the second-order effects will be described in chapter 6.

Chapter 6

Systematic Experimental Error Sources

This chapter explores and quantifies sources of systematic error that arise in a cryogenic torsion pendulum used to measure G with a frequency method.

Fiber

A defining feature of a torsion pendulum is that it hangs by a fiber. While low-precision experiments can treat the pendulum as an ideal damped torsional harmonic oscillator, this would be naïve in a high-precision experiment, where its anharmonic behavior would bias the results. For a more complete examination of the fiber's behavior, see [Anelastic behavior of a torsion pendulum with a CuBe fiber at low temperature, and implications for a measurement of the gravitational constant](#) (1998), Michael Kurt Bantel's PhD thesis [18].

A well-behaved fiber's anharmonic torques are quite small relative to its simple harmonic torque. For the UCI G experiment, the anharmonic torques were at most five orders of magnitude smaller than the harmonic torque.

Conservative Fiber Anharmonics

The simplest anharmonic torques in a fiber are terms proportional to θ^n , where $n > 1$. These can be thought of as higher order terms of a Taylor expansion of the fiber's torque as a function of θ . They will affect the pendulum's frequency and mean angular displacement (or “offset”), as well as generating harmonics of the fundamental sinusoidal oscillation, but do not dissipate energy. A calculation of these effects to first order is found in Appendix B, using the formalism laid out in Appendix A.

Anharmonic torques proportional to odd powers of θ will produce a shift in frequency. For a torque component proportional to θ raised to an odd power, n , this frequency shift will be proportional to a $A^{(n-1)}$, where A is the torsional amplitude. This can lead to an error in G if the ring modulation produces a systematic change in the amplitude. Consider how an error in G might arise from a torque

$$\tau = -k_1 \theta - k_3 \theta^3 \quad (6.1)$$

To first order in the ratio k_3/k_1 , this will shift the frequency by an amount,

$$\frac{\delta \omega^2}{\omega^2} = \frac{3}{4} \frac{k_3}{k_1} A^2 \quad (6.2)$$

If the torsional amplitude A changes systematically by an amount δA when the source mass ring positions are modulated, then there will be a systematic contribution to the total frequency shift given by

$$\delta \left(\frac{\delta \omega^2}{\omega^2} \right) = \frac{3}{2} \frac{k_3}{k_1} A \delta A_{signal} \quad (6.3)$$

This leads to a systematic mismeasurement of G by the ratio of this value to the frequency shift produced by the rings when they are modulated, found in Appendix C to be approximately

$$\left(\frac{\Delta \omega^2}{\omega^2}\right)_{signal} = \frac{\beta_2}{k_1} \frac{4 J_1(2A)}{A} \quad (6.4)$$

where β_2 is the amplitude of the signal torque

$$\tau_{signal} = -\beta_2 \sin(2\theta) \quad (6.5)$$

This yields a potential error in G of

$$\frac{\delta G}{G} = \frac{3}{8} \frac{k_3}{\beta_2} \frac{A^2}{J_1(2A)} \delta A_{signal} \quad (6.6)$$

For the amplitudes used in the experiment, this leads to the following errors:

**Table 6.1: Error in G from Systematic Amplitude Excitations (δA)
during Ring Modulation due to a Torque k_3 Frequency Shift**

A (rad)	(dlogG /dA) / (k ₃ /β ₂)
0.3	0.24
2.57	-14.6
4.21	48.9
5.81	-109
7.4	199

For the UCI G experiment, the value of k_3/β_2 is approximately -8×10^{-4} (using a CuBe fiber as drawn), leading to a potential 1 ppm G error sensitivity due to systematic amplitude variation of as little as 7.5 μ rad (for 7.4 radian amplitude) or 5.4 mrad at 0.3 radians.

Sensitivity to Amplitude Error

A systematic amplitude error can lead to a systematic error in G . From chapter 5, equation 23, we define the signal measurement, $s(A)$, to be

$$s(A) \equiv \left(\frac{\Delta \omega^2}{\omega^2} \right)_s \simeq \frac{2J_1(2A)}{A} \frac{\beta_2}{k_1} \propto G \quad (6.7)$$

(For a difference in frequency as the rings shift from one position to the other, double this quantity) Then, using a Taylor expansion of $J_1(2A)$ at an amplitude near any A_0 (defined as any point where s is at a local extremum),

$$\frac{\Delta s(A, A_0)}{s(A_0)} \equiv \frac{s(A) - s(A_0)}{s(A_0)} \simeq -2(A - A_0)^2 \quad (6.8)$$

The only exception is the maximum near $A = 0$, where the formula is

$$\frac{\Delta s(A, 0)}{s(A_0)} \simeq -\frac{A^2}{2} \quad (6.9)$$

Next, we can ask how much an uncertainty in the amplitude will affect a measurement of $s(A)$ at some amplitude near (but not at) a maximum. If $(A - A_0)$ is known to within some accuracy, δA , then the formula is:

$$\frac{\delta G}{G} \simeq \delta \left[\frac{\Delta s(A, A_0)}{s(A_0)} \right] = \frac{\partial \left[\frac{\Delta s(A, A_0)}{s(A_0)} \right]}{\partial A} \delta A \simeq 4(A - A_0) \delta A \quad (6.10)$$

or, at 0 amplitude,

$$\frac{\delta G}{G} \simeq \delta \left[\frac{\Delta s(A, 0)}{s(A_0)} \right] \simeq A \delta A \quad (6.11)$$

These two equations show that an experiment that takes place far from a maximum needs a more precise measurement of the amplitude than one that takes place close to a maximum.

Dissipative Fiber Torques

Studies of the fibers used at UCI [17,18] and elsewhere [19] have shown that the measured value of $1/Q$ as a function of amplitude for a torsion pendulum has the following functional form:

$$\frac{1}{Q} = \left(\frac{1}{Q} \right)_{A=0} + b A \quad (6.12)$$

for some value of b (for the UCI G lab, b is between $2.1 \cdot 10^{-7}$ for Al and $1.5 \cdot 10^{-6}$ for CuBe fibers as drawn). We now ask what fiber behavior can account for this observed linear dependence of $1/Q$ on amplitude. Because

$$\frac{1}{Q} = \frac{\text{change in energy over one period}}{2\pi * (\text{oscillator energy})} \equiv \frac{\Delta E_{\text{cycle}}}{(2\pi E)} \quad (6.13)$$

and since

$$E \approx \frac{1}{2} k_1 A^2 \quad (6.14)$$

we can infer that the functional form of equation 12 is caused by a torque that each cycle dissipates energy in proportion to A^3 :

$$\Delta E = \int_{\text{cycle}} \tau(A, \theta(t), \dot{\theta}(t); t) \dot{\theta} dt = (\text{constant}) * A^3 \quad (6.15)$$

If we set our 0th order behavior to be

$$\theta(t) = A \sin(\omega t) \quad (6.16)$$

then we are left with the 0th order equation

$$\Delta E = A \omega \int_{\text{cycle}} \tau(A, \theta(t), \dot{\theta}(t); t) \cos(\omega t) dt = (\text{constant}) * A^3 \quad (6.17)$$

This happens when a dissipative torque is proportional to A^2 , or to some function with an integral over one period that is proportional to A^2 , such as θ^2 or $(d\theta/dt)^2$, or some combination. Possible combinations include:

$$\tau_{A^2} = -k_{A^2} A^2 \hat{\theta} \quad (6.18a)$$

$$\tau_{\theta^2} = -k_{\theta^2} \theta^2 \hat{\theta} \quad (6.18b)$$

$$\tau_{\dot{\theta}^2} = -k_{\dot{\theta}^2} \dot{\theta}^2 \hat{\theta} \quad (6.18c)$$

$$\tau_{A\theta} = -k_{A\theta} A |\theta| \hat{\theta} \quad (6.18d)$$

$$\tau_{A\dot{\theta}} = -k_{A\dot{\theta}} A \dot{\theta} \quad (6.18e)$$

$$\tau_{\theta\dot{\theta}} = -k_{\theta\dot{\theta}} |\theta| \dot{\theta} \quad (6.18f)$$

Note that the first four expressions require a factor,

$$\hat{\theta} = \text{sign}(\dot{\theta}) \quad (6.19)$$

in order to generate nonconservative torques. Hu and Luo [19] and Peters [20] have tended to assume the functional form of equation 18c, while Bantel and Newman [17, 18] have modeled the amplitude-dependent Q term with the stick-slip model, represented by a combination of equations 18a, 18b, and a non-dissipative term proportional to $A\theta$. Using the method outlined in Appendix A, none of these dissipative torque expressions listed above (equations 18a-f) will affect either the frequency or the mean angle (“offset”), though they will produce the following “odd cosine” harmonic amplitudes (all “sine” harmonics and “even cosine” harmonics are equal to 0):

$$k_{A^2}: a_n = \frac{4}{\pi} \frac{(-1)^{\frac{n+1}{2}}}{n(n^2-1)} A^2 \frac{k_{A^2}}{k_1}, \text{ n odd} \quad (6.20a)$$

$$k_{\theta^2}: a_n = -\frac{A_n}{k_1} \frac{1}{n^2-1} = \frac{4}{\pi} \frac{(-1)^{\frac{n-1}{2}} (n^2-2)}{n(n^2-4)(n^2-1)} A^2 \frac{k_{\theta^2}}{k_1}, \text{ n odd} \quad (6.20b)$$

$$k_{\dot{\theta}^2}: a_n = -\frac{A_n}{k_1} \frac{1}{n^2-1} = \frac{8}{\pi} \frac{(-1)^{\frac{n+1}{2}}}{n(n^2-4)(n^2-1)} A^2 \frac{k_{\dot{\theta}^2}}{k_1}, \text{ n odd} \quad (6.20c)$$

$$k_{A\theta}:a_n = \frac{2}{\pi} \left(\frac{1}{n^2-1} \right) \left(\frac{1}{(-1)^{\frac{n-1}{2}} \frac{n}{2} - \frac{1}{2}} \right) A^2 \frac{k_{A\theta}}{k_1}, \text{ n odd} \quad (6.20d)$$

$$k_{A\dot{\theta}}:a_n = 0 \text{ for all n} \quad (6.20e)$$

$$k_{\theta\dot{\theta}}:a_n = \frac{4}{\pi} \frac{1}{n^2-4} \frac{1}{n^2-1} A^2 \frac{k_{\theta\dot{\theta}}}{k_1}, \text{ n odd} \quad (6.20f)$$

Each of these terms contributes to $\Delta(1/Q)$, as well:

$$\Delta\left(\frac{1}{Q}\right)_{A^2} = \frac{4}{\pi} A \frac{k_{A^2}}{k_1} \quad (6.21a)$$

$$\Delta\left(\frac{1}{Q}\right)_{\theta^2} = \frac{4}{3\pi} A \frac{k_{\theta^2}}{k_1} \quad (6.21b)$$

$$\Delta\left(\frac{1}{Q}\right)_{\theta^2} = \frac{8}{3\pi} A \frac{k_{\theta^2}}{k_1} \quad (6.21c)$$

$$\Delta\left(\frac{1}{Q}\right)_{\theta^2} = \frac{2}{\pi} A \frac{k_{A\theta}}{k_1} \quad (6.21d)$$

$$\Delta\left(\frac{1}{Q}\right)_{A\dot{\theta}} = A \frac{k_{A\dot{\theta}}}{k_1} \quad (6.21e)$$

$$\Delta\left(\frac{1}{Q}\right)_{A\dot{\theta}} = \frac{4}{3\pi} \frac{k_{\theta\dot{\theta}}}{k_1} \quad (6.21f)$$

It is difficult [21] to ascertain which mathematical function listed (or possibly another, unlisted function that we haven't thought of) is most relevant. A torque of the form of equation 18c would arise from friction in a viscous fluid, which is quite unlikely to occur in the very low pressure and temperature present during the experiment. Further evidence against viscous damping comes from the fact that different fibers provide very different

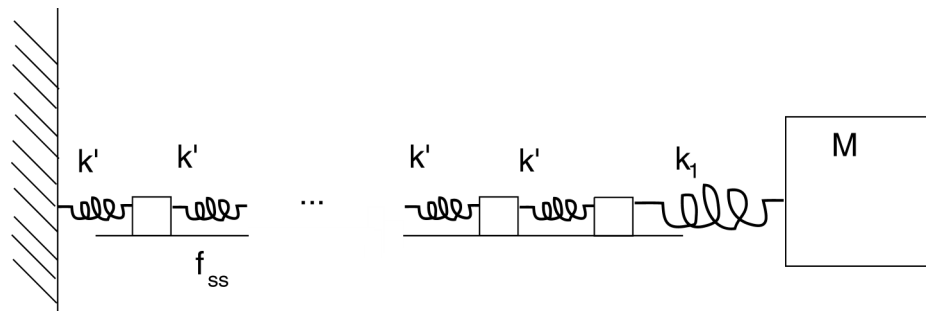
values of $d(1/Q)/dA$, so the dominant source of dissipation likely originates from the fiber's internal friction, rather than externally, through an ambient effect.

In searching for a physical, fiber-based damping mechanism, the lab has explored the stick-slip model, discussed briefly below.

The Stick-Slip Model

A stick-slip torque (described more extensively in Appendix D) is a candidate for damping that can produce a linear dependence of $1/Q$ on amplitude. See figure 1

Figure 6.1: The Stick-Slip Effect



In this linear version, a large series of massless blocks are coupled frictionally to a fixed “floor,” and slide when the force on each block exceeds a set frictional force value, f_{ss} (which is equal for each block). This f_{ss} is both a static and dynamic coefficient of friction. The oscillating mass, M , drags the closest blocks back and forth a small distance as it oscillates.

A torsional analog would involve zero-inertia stick-slip “discs” coupled to a fixed base, with the last one attached to the fiber. This would necessarily be a “mount” or “edge” effect. The effective differential torque would be

$$\tau_{ss} = k_{ss} [2 A \theta - \hat{\theta} (A^2 - \theta^2)] \quad (6.22)$$

leading to a first-order frequency shift, and “odd cosine” harmonics, as described in Appendix D. The contribution to $(1/Q)$ is simply the difference of 21a and 21b (replacing their respective k 's with k_{ss}):

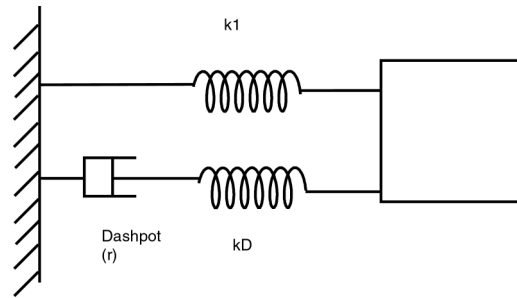
$$\Delta \left(\frac{1}{Q} \right)_{ss} = \frac{8}{3\pi} \frac{k_{ss}}{k_1} A \quad (6.23)$$

Unfortunately, the physical mechanism described in Appendix D is not fully consistent with the physical situation. In the UCI G lab, the fiber is attached to its mount by a drop of epoxy. If the stick-slip model presented were to be realistic, the “stick-slip” effect would need to take place entirely at the region of contact of the fiber with the epoxy. Therefore, additional drops along the length of the fiber should have increased the magnitude of the “stick-slip” effect, which should have been seen as a change in the value $d(1/Q)/dA$. In fact, additional drops did not affect this value, although they did serve to increase $1/Q$ by a fixed amount at all amplitudes.

The Kuroda Effect

Kuroda [14] has shown that dashpot-spring effects can cause the spring constant, k_1 , to appear to vary with frequency. This can cause a systematic upward bias in values of G . Consider figure 2.

Figure 6.2: Harmonic Spring with One Maxwell Unit



Imagine that the natural frequency of oscillation could be adjusted (while keeping the Maxwell unit constant). For extremely low frequency, the dashpot would slide to keep the bottom spring, k_D , relaxed at all times. The effective spring constant would be $k_1' = k_1$. Next, consider what would happen at very high frequency (much higher than the time constant of the Maxwell unit). Here, the dashpot would not relax significantly, and the effective spring constant would be $k_1' = k_1 + k_D$. Thus, a changing frequency of oscillation induces a changing spring constant, further changing the frequency of oscillation. Increasing or decreasing the frequency by moving a source mass coupled to a torsion pendulum will do exactly this.

The model explored by Kuroda is that of a logarithmic frequency distribution of maxwell units. Newman and Bantel [15] have placed an upper limit on the G bias produced by this mechanism for any distribution of Maxwell units:

$$0 \leq \frac{\delta G}{G} \leq \frac{1}{2Q} \quad (6.24)$$

Because the fiber in the UCI G experiment has a Q greater than 50,000 during all data runs, the contribution of the Kuroda effect on the measured value of G is less than 10 ppm.

Magnetic Field

Magnetic fields are an insidious problem for torsion pendulum experiments. The minuscule differential gravitational torques on the torsion pendulum can be easily dwarfed by even a small magnetic coupling between the pendulum and the source mass, and magnetic shielding is expensive and only partly effective. In some torsion pendulum experiments, any change in the magnetic field in the region around the torsion pendulum is offset by three orthogonal Helmholtz coils, all centered on the pendulum and controlled by feedback loops.

The UCI G experiment does not use active feedback, but instead relies entirely on magnetic shielding, providing an attenuation of a factor of approximately 2000 to variations in the magnetic field. The outermost layer is Metglas magnetic shielding. It comes in the form of a metal tape or ribbon which is wrapped as elegantly as possible around the exterior of the dewar; it is far from a continuous layer. The material is degaussed at the beginning of each cooldown. The second layer of magnetic shielding consists of lead foil wrapped around the walls and floor of the vacuum chamber, with a third layer of lead foil wrapped around the cold can (a cylindrical wall of aluminum located inside of the vacuum can but around the experiment, that is in thermal contact with the 2K pot rather than the 4.2K liquid helium bath). This is effective because all of these layers of lead are at less than 4.2K, and lead becomes superconductive at its critical temperature of 7.2K. The UCI G experiment then takes advantage of the Meissner effect, dramatically reducing changes in the magnetic field lines that pass through the lead shielding after it hits its critical temperature. Experiments at the UCI G lab have shown an attenuation of approximately 1000 with this effect. When the source mass is modulated during the experiment, any changes in the

magnetic field induced by the modulation of the source mass and external to the experiment must affect the pendulum by going around the lead shielding.

Ideally, the lead shielding would form a complete, unbroken shell around the pendulum. In practice, insulated wires need to pass through that shell. Feedthroughs, and pumping lines require holes to pass through the lead shield. Therefore, the superconductive shielding is open at the top of the vacuum can. The Metglas magnetic shielding wrapped around the dewar is open at the mouth of the dewar.

Most magnetic fields are only a minor concern: they might degrade Q through eddy current damping, but will only produce a spurious signal if a component of the field modulates with the gravitational signal. Therefore, the main concern is changes of the magnetic field in the vicinity of the pendulum that are associated with ring position. The rings can produce field variation in one of two ways, either as a response to the earth's magnetic field, or else internally, either from residual ferromagnetism in the “non magnetic” nickel-phosphorous coating of the copper rings or from magnetic impurities in the bulk of the copper ring material.

In order to estimate an upper limit on magnetic field strength perturbation, the magnetic field produced by the rings was measured by a magnetometer with sensitivity below 1 mGauss. A null reading was achieved, but the 1σ upper limit of the ring fields at the point of the pendulum was 0.16 mGauss for a configuration with no shielding at all. The upper limit of the sensitivities was 20 ns of period change per mGauss, translating to

$$\frac{\delta \omega^2}{\omega^2} = 2 \frac{\delta \omega}{\omega} = 2 \frac{\delta T}{T} = 2 \frac{20 \text{ nSec}}{\text{mGauss}} 0.16 \text{ mGauss} \frac{1}{135 \text{ s}} = 4.7 \times 10^{-11} \quad (6.25)$$

$$\frac{\delta G}{G} = \frac{\left(\frac{\delta \omega^2}{\omega^2}\right)}{\left(\frac{\Delta \omega_{rings}^2}{\omega^2}\right)} = \frac{\left(2\frac{\delta T}{T}\right)}{\frac{\beta_2}{k_1} \left(\frac{4J_1(2A)}{A}\right)} = \frac{4.7*10^{-11}}{4.8*10^{-5} * 4 \frac{J_1(2A)}{A}} = \frac{2.5*10^{-7}}{\frac{J_1(2A)}{A}} < 9 \text{ ppm} \quad (6.26)$$

The value of 9ppm is for a the maximum of the signal near $A = 7.4$ radians. All other amplitudes used in data runs had smaller corrections to G . For 2.57 radians it was less than 2 ppm. Also, the shielding should attenuate this number even further.

Eddy Current Damping

The functional response of the pendulum to eddy current damping is explored in Appendix E. If we assume that the pendulum is perfectly flat and thin, and further define the “strength” of the eddy current damping as $k_{e.c.}$, then the torque it applies to the pendulum will be

$$\tau_{e.c.} = -k_{e.c.} \sin^2(\theta - \psi_0) \dot{\theta} \quad (6.27)$$

where ψ_0 is the angle between the horizontal component of the magnetic field and the normal vector of either face of the pendulum at rest. Such a torque will not affect the frequency or the pendulum “offset” (mean angle), but will generate harmonics (see appendix E), and contribute to damping in the following manner:

$$\Delta\left(\frac{1}{Q}\right) = \frac{\omega}{2} \left(1 - \cos[2\psi_0] \frac{J_1(2A)}{A}\right) \frac{k_{e.c.}}{k_1} \quad (6.28)$$

For large amplitudes this approaches “- b v” type damping, but at lower amplitudes its exact contribution to damping is determined by the angle ψ_0 and the amplitude.

If for no other reason than maximizing the value of Q , magnetic fields should be reduced as far as is possible.

Optics

Systematic error from optical misalignment is a potential problem. As shown in Chapter 1, it can have a detrimental effect on static torsion pendulum experiments. In a dynamic experiment, however, the problem is eliminated. No misalignment of the optics can cause a systematic change in the measured period of the pendulum.

Pendulum Heating

A systematic difference in pendulum heating between one ring configuration and another can translate into a spurious G signal by affecting the frequency of oscillation of the fiber. The main source of heating of the UCI G pendulum is from the light used to image the pendulum, although other potential sources of heat include the heaters in the temperature control loop, some sort of differential heat pickup from the stepper motor when the rings move in one direction and not the other, etc.

The pendulum using Aluminum 5056 fiber (which had the greatest sensitivity to temperature of any fiber we used) had a period sensitivity to temperature changes of

$$\frac{\partial \log P}{\partial T_4} < 7 \frac{\text{ppm}}{\text{K}} \quad (6.29)$$

$$\frac{\delta G}{G} = \delta \log G = \frac{\delta \omega^2 / \omega^2}{\Delta \omega_{\text{signal}}^2 / \omega^2} \quad (6.30)$$

$$\frac{\delta \omega^2}{\omega^2} = \frac{2 \omega \delta \omega}{\omega^2} = 2 \frac{\delta \omega}{\omega} = -2 \frac{\delta P}{P} = -2 \delta \log P \quad (6.31)$$

$$\frac{\partial \log G}{\partial T_4} = -14 \frac{\text{ppm}}{\text{K}} \quad (6.32)$$

Careful monitoring of the fiber support temperature put limits on the temperature variations of the experimental runs, the largest of which were on the order of one mK. Also

reassuringly, the time constant of heat dissipation in the pendulum is on the order of 11 hours, much longer than the ring modulation period of approximately 40 minutes.

Second order couplings

The full set of torques on the pendulum includes the terms

$$\begin{aligned} \tau(\theta, \dot{\theta}, A) = & -k_1 \theta + \sum_{n=2}^{\infty} -k_n \theta^n - \sum_{n=1}^{\infty} [\alpha_n \cos(n\theta) + \beta_n \sin(n\theta)] \\ & - k_{ss} [2A\theta - \hat{\theta}(A^2 - \theta^2)] - k_{ec} \dot{\theta} \sin^2(\theta - \psi_0) - k_{visc} \dot{\theta}^2 - \dots \end{aligned} \quad (6.33)$$

(k_{ss} , k_{ec} , and k_{visc} represent the strength of the stick-slip, eddy current, and viscous or “- b v²” torque on the pendulum).

Torques that affect the frequency to first order include odd-n θ^n torques, the stick-slip torque (through its “- 2 A θ ” component), and β_n torques.

The frequency shift (as well as harmonics, changes in mean angle of orientation or “offset,” and contribution to 1/Q) from each of these listed torques has been derived analytically to first order for all of the torques listed in equation 33, and are derived in Appendices B-E, using the method laid out in Appendix A.

To first order, each of these effects is independent of one another. All frequency shifts will add linearly, as will contributions to 1/Q, offset, harmonics, etc. Even the G signal is not affected, to first order, by the presence or absence of any other torques (except, of course, for the dominant k_1 torque). Numerical analysis has shown that this first order analysis is adequate for a G measurement on the order of 10 ppm, using a method outlined below.

The second order effects of perturbing torques (for example, k_3 or a contribution to β_2 from ambient static gravitational fields) upon one another can be understood qualitatively in the following way:

The assumption in constructing each of these first-order terms is that each is acting on a pendulum undergoing perfect sinusoidal motion. But as each term adds its harmonics to the pendulum behavior, the pendulum's motion deviates from this pure harmonic motion, and when the second order effects are determined, they must take into account the first-order harmonics generated by all relevant torques (including the torque whose second-order effect is being examined). Third-order effects must take into account harmonics generated by second-order torques, and so on.

To quantitatively evaluate the nonlinear second order effects of the torque terms in equation 33, we proceed as follows:

First, we define a more concise method of describing the relative strength of the various torques. We will define the strength of each torque to be u_i , where i is some appropriate index to identify the torque, and u_i is the parameter equal to the torque coefficient divided by k_1 . So, for example,

$$u_{k_3} = \frac{k_3}{k_1}, u_{\beta_4} = \frac{\beta_4}{k_1}, etc... \quad (6.34)$$

Notice that each of these parameters u_i is dimensionless, and that a perturbative treatment is only valid where

$$u_i \ll 1 \quad (6.35)$$

The pendulum oscillation frequency will be a function of torsional amplitude A , k_1 , and the set of u_i parameters. We may Taylor expand that function as follows, where the coefficients C_i , D_{ij} , E_{ijk} , ... are each functions of A .

$$\frac{\omega^2}{\omega_0^2} = 1 + \sum_i C_i u_i + \sum_{i,j} D_{i,j} u_i u_j + \sum_{i,j,k} E_{i,j,k} u_i u_j u_k + \dots \quad (6.36)$$

To first order, we then have

$$\frac{\omega^2}{\omega_0^2} = 1 + \frac{\delta \omega^2}{\omega_0^2} = 1 + \sum_i C_i u_i + O(u^2) \quad (6.37)$$

where, for example,

$$\begin{aligned} u_{k_3} &= \frac{k_3}{k_1}; C_{k_3} = \frac{3}{4} A^2; \\ u_{\beta_4} &= \frac{\beta_4}{k_1}; C_{\beta_4} = 2 \frac{J_1(4A)}{A} \\ &\text{etc...} \end{aligned} \quad (6.38)$$

The notation “ u_s ” (s for signal) will be reserved for the β_2 torque associated with the source mass rings:

$$u_s = \frac{\beta_{2rings}}{k_1}; C_s = \frac{2J_1(2A)}{A} \cos(2\theta_{rings}) \quad (6.39)$$

Note the $\cos(2\theta_{rings})$ term in equation 39. During the experiment, the ring positions are modulated as the ring pair revolves $\pi/2$ radians about the pendulum axis and then back again, causing a sign flip in C_s . It is this sign flip that represents the change in frequency as the rings are modulated. Rewriting equation 37 to include the s index notation,

$$\frac{\omega^2}{\omega_0^2} = 1 + \frac{\delta \omega^2}{\omega_0^2} = 1 + C_s u_s + \sum_i C_i u_i + O(u^2) \quad (6.40)$$

Generalizing to account for second order terms

$$\begin{aligned} \frac{\omega^2}{\omega_0^2} &= 1 + \frac{\delta \omega^2}{\omega_0^2} = 1 + C_s u_s + \sum_i C_i u_i \\ &\quad + D_{ss} (u_s)^2 + \sum_j D_{sj} u_s u_j + \sum_i \sum_j D_{ij} u_i u_j + O(u^3) \end{aligned} \quad (6.41)$$

This equation does not include a small contribution from the β_6 and higher contribution of the ring source masses to the torque. This contribution is small enough that it needs to be treated only to first order, and is handled separately in our analysis.

The signal on which our G measurement is based is the difference $\Delta\omega^2_{\text{signal}}$ defined as the difference between the ω^2 values for the two different ring positions. Terms linear in u_s change sign in equation 41 when the rings move, contributing the following to $\Delta\omega^2_{\text{signal}}$:

$$\frac{\delta \omega^2_{\text{signal}}}{\omega_0^2}(\text{from } u_s) = C_s u_s + \sum_j D_{sj} u_s u_j + O(u_s^3) \quad (6.42)$$

We see immediately that if the D_{sj} terms are ignored, the result is an error in G given by:

$$\frac{\delta G}{G} = \frac{\delta \omega^2(\text{perturbative effect})}{\Delta \omega^2(\text{ring signal})} = \frac{D_{sj}(A) u_s u_j}{C_s(A) u_s} = \frac{D_{sj}(A)}{C_s(A)} u_j \quad (6.43)$$

Equivalently, a G value found using only the C_s term must be corrected by this amount.

Thus, it is important to evaluate the D_{sj} coefficients for the perturbing torques which affect our G measurement.

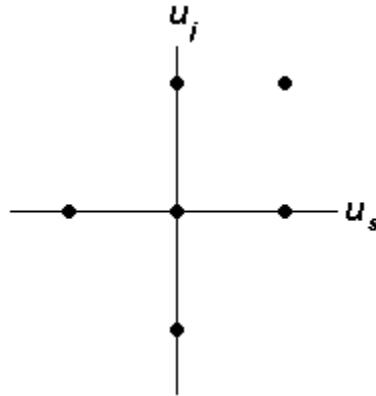
Equation 42 does not fully account for the signal frequency shift, because there will be terms in equation 41 which are not proportional to β_2 but still change their value when the rings are moved. Examples are terms proportional to β_1 arising from magnetic couplings, or proportional to β_3 arising from small defects in source mass and pendulum fabrication. Such effects need only be considered to first order, and may be treated separately.

We now discuss the numerical evaluation procedure used to evaluate the D_{sj} coefficients, and their resulting values.

To evaluate the relevant D_{sj} coefficients, while at the same time testing the correctness of our analytic evaluation of the C_i and C_s coefficients, we made a set of six

numerical integrations of the equation of motion implied by equation 42. Each integration used a different set of values of u_i and u_s , in the pattern shown by Figure 3.

Figure 6.3: Points Used to Determine C_i and $D_{s,j}$ Cross Terms



The initial angular position of the pendulum in each integration was an arbitrary value chosen to give the desired amplitude A , while its initial velocity was zero. The integration tracked the motion of the pendulum through a little more than 1.5 oscillation cycles, with a minimum accuracy of 10^{-14} rad and 10^{-14} seconds. The corresponding frequency ω for each parameter set was determined by finding the time interval between sequential negative slope zero crossings of the $\theta(t)$ function.

The resulting set of six frequencies were then fit to equation 42 to determine the desired C and D coefficients. This process was repeated for a set of oscillation amplitudes corresponding to those used in our G measurement. Additionally, for each amplitude, the derivatives dC_j/dA and $dD_{s,j}/dA$ were determined by making small variations in the assumed value of the amplitude A .

The resulting C coefficients agreed with those calculated analytically to at least seven digits, providing an important check of these calculations.

The effect of neglecting higher order terms in the expansion of equation 42 was probed by increasing the magnitude of the assumed u_s and u_i parameters in the numerical integration, and found to be negligible.

Resulting values of the C and D coefficients, and their derivatives with respect to A, are presented in tables 2-5.

Table 6.2: $C_i(A)$

	Ci(A)				
	0.3 rad	2.57 rad	4.21 rad	5.81 rad	7.4 rad
$\beta_{2\text{Signal}}$	1.9113	-0.2646	0.1290	-0.0800	0.0558
$\beta_{2\text{Background}}$	1.9113	-0.2646	0.1290	-0.0800	0.0558
β_1	0.9888	0.3736	-0.0673	-1.0657	0.0295
β_3	2.7063	0.1418	-0.0685	-0.0538	0.0246
β_4	3.3219	-0.0189	-0.0329	-0.0263	-0.0206
β_5	3.7196	-0.0807	0.0818	-0.0001	-0.0353
β_6	3.8768	0.1384	-0.0458	0.0212	-0.0118
α_1	0	0	0	0	0
α_2	0	0	0	0	0
α_3	0	0	0	0	0
α_4	0	0	0	0	0
k_2	0	0	0	0	0
k_3	0.0675	4.95	13.28	25.32	41.05
k_{ss}	-0.6000	-5.14	-8.42	-11.62	-14.8
b_v^2	0	0	0	0	0
b_{mag}	0	0	0	0	0

Because amplitude varies during the course of a data run, the first derivative of C_i with respect to A is also relevant:

Table 6.3: dC_i/dA (rad^{-1})

	$dC_i(A)/dA$				
	0.3 rad	2.57 rad	4.21 rad	5.81 rad	7.4 rad
$\beta_{2\text{Signal}}$	-0.5822	0	0	0	0
$\beta_{2\text{Background}}$	-0.5822	0	0	0	0
β_1	-0.0744	-0.3544	-0.1464	0.6931	0.0674
β_3	-1.8917	0.4362	0.2698	-0.0996	-0.1209
β_4	-4.2493	-0.7595	-0.3336	-0.1954	-0.1315
β_5	-7.7360	0.8140	0.0304	-0.2547	0.0225
β_6	-12.2457	-0.5431	0.3762	-0.2540	0.1834
α_1	0	0	0	0	0
α_2	0	0	0	0	0
α_3	0	0	0	0	0
α_4	0	0	0	0	0
k_2	0	0	0	0	0
k_3	0.45	3.85	6.31	8.71	11.1
k_{ss}	-2	-2	-2	-2	-2
b_v^2	0	0	0	0	0
b_{mag}	0	0	0	0	0

Next are the values of the cross terms, and their amplitude derivatives:

Table 6.4: Values of D_{sj}

	Dsj(A)				
	0.3 rad	2.57 rad	4.21 rad	5.81 rad	7.4 rad
$\beta_{2\text{Signal}}$	Does Not Modulate				
$\beta_{2\text{Background}}$	-0.0006	-0.0430	-0.0150	-0.0072	-0.0042
β_1	-0.0001	-0.0270	0.0170	-0.0006	-0.0047
β_3	-0.0021	0.0290	0.0040	-0.0058	-0.0009
β_4	-0.0048	-0.0111	0.0060	-0.0034	0.0021
β_5	-0.0088	-0.0055	-0.0090	-0.0009	0.0026
β_6	-0.0140	0.0160	0.0038	0.0013	0.0006
α_1	-0.57	0	0	0	0
α_2	-0.55	0	0	0	0
α_3	-0.51	0	0	0	0
α_4	-0.45	0	0	0	0
k_2	-0.0175	0.0002	-0.0007	0.0018	-0.0034
k_3	0.0005	0.2468	-0.4070	0.5400	-0.6600
k_{ss}	0.1050	0.0049	-0.0170	0.0390	-0.0713
b_v^2	0	0	0	0	0
b_{mag}	0	0	0	0	0

Table 6.5: dD_{sj}/dA (rad)

	dD _{sj} /dA				
	0.3 rad	2.57 rad	4.21 rad	5.81 rad	7.4 rad
β₂Signal	Does Not Modulate				
β₂Background	-0.0084	0.1200	0.0350	0.0160	0.0085
β₁	-0.0011	0.0450	-0.0273	0.0040	0.0054
β₃	-0.0270	-0.0650	-0.0310	0.0090	0.0090
β₄	-0.0600	-0.0320	0.0085	-0.0040	0.0022
β₅	-0.1070	0.1100	0.0280	-0.0160	-0.0090
β₆	-0.1662	-0.1300	-0.0480	-0.0240	-0.0140
α₁	-1.7400	0.2240	0.1070	-0.0260	-0.0270
α₂	-1.4900	-0.1880	-0.0520	-0.0220	-0.1200
α₃	-1.1020	0.1360	-0.0025	-0.0180	0.0020
α₄	-0.6080	-0.0780	0.0275	-0.0130	0.0080
k₂	-0.17	2.33	-3.05	3.6	-4.08
k₃	0.0065	-0.35	0.45	-0.52	0.57
k_{ss}	0	0	0	0	0
b_v²	-0.0008	0.0100	0.0170	0.0160	-0.1770
b_{mag}	0.0056	-0.1690	0.1110	-0.1100	0.0880

Upper limits have been placed on several values of u_j , and the resultant change $\delta G/G$ calculated, and presented in table 6.

**Table 6.6: Limits on Change in G from Second Order Couplings at Signal Maxima
and 0.3 Rad**

(values of over 1 ppm are printed in bold)

Ui	Value	dG/G predicted (ppm)				
		0.3 rad	2.57 Rad	4.21 Rad	5.81 Rad	7.4 Rad
$\beta_{2\text{Signal}}/k_1$	4.7853E-5	1.0E+6	1.0E+6	1.0E+6	1.0E+6	1.0E+6
k_1 (cgs)	3.2600E-2	N/A	N/A	N/A	N/A	N/A
$\beta_{2\text{Background}}/k_1$	1.4356E-5	-4.8E-3	2.33	-1.67	1.3	-1.08
β_1/k_1	5.5000E-7	-2.0E-5	0.06	0.07	3.9E-3	-0.046
α_1/k_1	5.5E-7	-0.16	0	0	0	0
α_2/k_1	1.4E-5	-4.1	0	0	0	0
k_2/k_1	3.2E-7	-0.030	-2.1E-4	-1.9E-3	-7.3E-3	-0.020
k_3/k_1 CuBe	-3.7E-8	-9.5E-6	0.035	0.12	0.25	0.44
k_3/k_1 CuBe H.T.	-1.4E-7	-3.6E-5	0.13	0.44	0.94	1.65
k_3/k_1 Al 5056	-6.0E-8	-1.5E-5	0.056	0.19	0.4	0.71
k_{ss}/k_1 CuBe	7.0E-7	0.038	-0.013	-0.092	-0.34	-0.89
k_{ss}/k_1 CuBe H.T.	1.4E-6	0.077	-0.026	-0.185	-0.68	-1.8
k_{ss}/k_1 Al 5056	1.9E-7	0.01	-0.0035	-0.025	-0.093	-0.24
b_v^2/k_1	1.8E-6	0	0	0	0	0
b_{mag}/k_1	4.0E-5	0	0	0	0	0

**Table 6.7: $d\text{Log}(G)/dA$ (rad) from Second Order Couplings
at Signal Maxima and 0.3 Radians
(using the values for u_j found in Table 6)**

U _i	Value	dLog(G)/dA (ppm/rad)				
		0.3 rad	2.57 Rad	4.21 Rad	5.81 Rad	7.4 Rad
$\beta_{2\text{Signal}}/k_1$	4.7853E-5	0	0	0	0	0
k_1 (cgs)	3.2600E-2	N/A	N/A	N/A	N/A	N/A
$\beta_{2\text{Background}}/k_1$	1.4356E-5	-0.06	-6.5	3.9	-2.9	2.2
β_1/k_1	5.5000E-7	-3.2E-4	-0.094	-0.12	-0.028	0.050
α_1/k_1	5.5E-7	-0.5	-0.47	0.46	0.18	-0.27
α_2/k_1	1.4E-5	-11.2	10.2	-58	39	-31
k_2/k_1	3.2E-7	-0.028	-2.9	-7.7	-15	-24
k_3/k_1 CuBe	-3.7E-8	-2.4E-4	1.3E-2	-1.7E-2	1.9E-2	-2.1E-2
k_3/k_1 CuBe H.T.	-1.4E-7	-9.1E-4	4.9E-2	-6.4E-2	7.3E-2	-7.9E-2
k_3/k_1 Al 5056	-6.0E-8	-3.9E-4	2.1E-2	-2.7E-2	3.1E-2	-3.4E-2

(values of greater than 10ppm per radian are printed in bold)

Other Sources of Error

There are a great many aspects of the UCI G measurement that are not addressed in this thesis. These include details of data analysis procedures, including (for example) data cuts based on ring swing amplitudes following transport, cuts on fiber temperature variation, techniques used to include the protocols for varying ring configurations between run sets to average out mass density variation effects, and corrections for variation in air density and ring temperature. And of course, a vast number of details related to mass and dimensional metrology techniques and their uncertainties have not been discussed.

Chapter 7

Reported Value of G

The experiment used three fibers, and operated at various amplitudes determined by the maxima of the Bessel function, $J_1(2A)/A$. This allowed us to check the consistency of the measurement at higher amplitudes where anharmonic torques should produce a greater effect on the signal. In fact, results were consistent over the range of torsional amplitudes for each fiber type, but differed significantly among the different fibers used. Expressed as a ppm difference relative to the current “CODATA” G value ($6.67428 \times 10^{-11} \text{ m}^3/\text{kg s}^2$), the fibers made from CuBe as drawn, heat treated CuBe, and A15056 yielded G values differing respectively from CODATA by 26, 8, and 54 ppm, with approximately 13 ppm uncertainty in each case. (The G values reported at the CPEM 2008 conference were larger by 10ppm in each case, having omitted a previously calculated 10ppm correction).

Our G measurement was conducted “blind” by hiding the precise value of field source masses until just before announcing the results. The data taken with the A15056 fiber was deemed a priori the more reliable of the three sets, because the A15056 fiber exhibits the highest quality factor, the least dependence of quality factor on torsional amplitude, and yielded the most consistent results at different amplitudes. Hence before removing the “blind,” we decided to base our announced G value on data taken using the A15056 fiber,

with an uncertainty reflecting the range of G values from the three fiber types. Our final G value is then larger than “CODATA” by 54 ppm, with an assigned uncertainty of (+25, -42) ppm. The result adds weight to the 2006 CODATA value relative to a G value reported by a BIPM group [8], which found G to be greater than the CODATA value by 196 ± 41 ppm.

The value of G reported by the UCI group is $6.67464 (+.00017, -.00028) \times 10^{-11}$ m³/kg s²

References

1. H. Cavendish, Esq. F. R. S. and A. S., *Experiments to Determine the Density of the Earth*. Philosophical Transactions of the Royal Society of London, Vol. 88, (1798), 469-526
2. W. Michaelis, H. Haars, R. Augustin, *A new precise determination of Newton's Gravitational Constant*. Metrologia **32** (1995/96) 267-276
3. P. J. Mohr, B. N. Taylor, David B. Newell, *CODATA Recommended Values of the Fundamental Physical Constants: 2006*, National Institute of Standards and Technology, Gaithersburg, Maryland
4. W. Michaelis, H. Haars, J. Melcher, *Supplementary investigations to PTB's evaluation of G*. Metrologia **41** (2004) L29-L32
5. O. V. Karagioz and V. P. Izmailov, *Measurement of the gravitational constant with a torsion balance*. Measurement Techniques, Vol. 39, No. 10 (1996) 979-987
6. C. H. Bagley and G. G. Luther, *Preliminary Results of a Determination of the Newtonian Constant of Gravitation: A Test of the Kuroda Hypothesis*. Phys. Rev. Lett. **78** issue 16 (1997) 3047-3050
7. J. H. Gundlach and S. M. Merkowitz, *Measurement of Newton's Constant Using a Torsion Balance with Angular Acceleration Feedback*. Phys. Rev. Lett. **85** issue 14 (2000) 2869-2872
8. T. J. Quinn et al., *A New Determination of G Using Two Methods*. Phys. Rev. Lett. **87** issue 11 (2001) 1101
9. U. Kleinvoss, et al., *Measurement of the Newtonian Gravitational Constant G*. Precision Electromagnetic Measurements. Conference Digest. Conference on Volume (2002) 148-149
10. T. R. Armstrong and M. P. Fitzgerald, *New Measurements of G Using the Measurement Standards Laboratory Torsion Balance*. Phys. Rev. Lett. **91**, issue 20 (2003) 1101-201104
11. Z. Hu, J. Guo, and J. Luo. *Correction of source mass effects in the HUST-99 measurement of G*. Phys. Rev. D. **71** issue 12 (2005) 7505-7508
12. St. Schlamminger, et al. *Measurement of Newton's gravitational constant*. Phys. Rev. D. **74** issue 8 (2006) 2001-2026
13. G. G. Luther and W. R. Towler, *Redetermination of the Newtonian Gravitational Constant G*. Phys. Rev. Lett. **48** (1982) 121-123

14. K. Kuroda, *Does the Time-of-Swing Method Give a Correct Value of the Newtonian Gravitational Constant?*. Phys. Rev. Lett. **75** (1995) 2796-2798
15. M. K. Bantel and R. D. Newman, *Preparation for a Determination of G using a Cryogenic Torsion Pendulum*, for the proceedings of the Eighth Marcel Grossman Meeting on General Relativity (1997)
16. R. D. Newman and M. K. Bantel, *On determining G using a cryogenic torsion pendulum*. Meas. Sci. Technol. **10** (1999) 445-453
17. M. K. Bantel and R. D. Newman. *High precision measurement of torsion fiber internal friction at cryogenic temperatures*. Journal of Alloys and Compounds **310** issues 1-2 (2000) 233-242
18. M. K. Bantel, PhD Thesis, *Anelastic behavior of a torsion pendulum with a CuBe fiber at low temperature, and implications for a measurement of the gravitational constant*. University of California at Irvine (1998)
19. Z. Hu, J. Luo, *Amplitude Dependence of Quality Factor of the Torsion Pendulum*, Phys Lett A **268** (2000) 255
20. R. D. Peters, *Oscillator Damping with More than One Mechanism of Internal Friction Dissipation*, arXiv:physics/0302003 v1 3 Feb 2003
21. A. B. Lebedev, *Application of Internal Friction to Analysis of Plastic Behavior of Crystals*, Journal de Physique IV, **6** (1996) C8-225-264

Appendix A

Perturbation of Harmonic Motion by a Small Nonlinear Force

Term

This appendix describes a method of determining the first-order effect of small perturbing forces on an oscillator dominated by simple harmonic behavior. Generally, such forces can change an oscillator's mean position (sometimes called “offset”), change its frequency, and generate higher harmonics of the fundamental oscillation. In this appendix, the notation corresponds to a linear harmonic oscillator, such as a mass on a spring. For a torsion oscillator, force, spring constant, mass, and position are replaced, respectively, with torque, torsional spring constant, moment of inertia, and angular position.

Consider a simple harmonic force,

$$F(x) = -k_1 x \tag{A.1}$$

yielding the differential equation

$$F(x) = m \ddot{x} = -k_1 x \tag{A.2}$$

with solutions

$$x(t) = A \sin(\omega_0 t + \phi) \tag{A.3}$$

for a frequency defined by $\omega_0^2 = \frac{k_1}{m}$ and amplitude A. Or, with an appropriate choice of

t,

$$x(t) = A \sin(\omega_0 t) \quad (\text{A.4})$$

Next, consider what happens when a small perturbing force is added to equation 2.

$$F(x) = m \ddot{x} = -k_1 x + P(x, \dot{x}) \quad (\text{A.5})$$

We will assume that the initial conditions for the solution of this equation yield a peak oscillation amplitude A such that

$$\frac{|P(x, \dot{x})|}{k_1 A} \ll 1 \quad \text{for all values of } -A \leq x \leq A \quad (\text{A.6})$$

The method we will use here to solve this equation is valid only for forces which do not depend on dx/dt , and thus are not dissipative. Assuming that the solution of equation 5 will be periodic in t , it can be expressed

$$x(t) = A \sin(\omega t) + x_0 + a_1 \cos(\omega t) + \sum_{n=2}^{\infty} [a_n \cos(n\omega t) + b_n \sin(n\omega t)] \quad (\text{A.7})$$

We will assume that the phase of the solution is implicitly chosen so that $a_1 = 0$. In addition, equation 7 must meet the conditions,

$$\begin{aligned} |x_0| &\ll A \\ |a_n| &\ll A \\ |b_n| &\ll A \end{aligned} \quad (\text{A.8})$$

Clearly, $x(t)$ is invariant under the discrete time translations of

$$t \rightarrow t + n \frac{2\pi}{\omega}, \quad n = 0, \pm 1, \pm 2, \dots \quad (\text{A.9})$$

The second derivative of equation 7 yields

$$\ddot{x}(t) = -A\omega^2 \sin(\omega t) - \sum_{n=2}^{\infty} (n^2 \omega^2) [a_n \cos(n\omega t) + b_n \sin(n\omega t)] \quad (\text{A.10})$$

Plugging equations 7 and 10 into equation 5 gives us

$$\begin{aligned}
& -m\omega^2 \left\{ A \sin(\omega t) + \sum_{n=2}^{\infty} n^2 [a_n \cos(n\omega t) + b_n \sin(n\omega t)] \right\} = \\
& k_1 \left\{ -A \sin(\omega t) - x_0 - \sum_{n=2}^{\infty} a_n \cos(n\omega t) + b_n \sin(n\omega t) \right\} + P(x)
\end{aligned} \tag{A.11}$$

Grouping like terms and dividing by m,

$$\begin{aligned}
& k_1 x_0 - A(m\omega^2 - k_1) \sin(\omega t) - \\
& \sum_{n=2}^{\infty} (n^2 m\omega^2 - k_1) [a_n \cos(n\omega t) + b_n \sin(n\omega t)] = P(x)
\end{aligned} \tag{A.12}$$

We recall that the unperturbed frequency is given by

$$\omega_0^2 = \frac{k_1}{m} \tag{A.13}$$

In order to proceed any further, $P(x, dx/dt)$ needs to be expressed as a function of time, and broken down into its Fourier series components:

$$\begin{aligned}
& P(t) = P(x(t)) \simeq P(A \sin(\omega t)) \\
& P(t) \simeq A_0 + \sum_{n=1}^{\infty} A_n \cos(n\omega t) + B_n \sin(n\omega t)
\end{aligned} \tag{A.14}$$

Note that the approximation in equation 14 expresses x using only the leading (0-order) term in equation 7. This approximation is permissible for a first-order perturbation of P in x and dx/dt .

The coefficients in equation 14 are:

$$A_0 = \frac{\omega}{2\pi} \int_0^{\frac{2\pi}{\omega}} P(t) dt \tag{A.15}$$

$$A_n = \frac{\omega}{\pi} \int_0^{\frac{2\pi}{\omega}} \cos(n\omega t) P(t) dt \tag{A.16}$$

$$B_n = \frac{\omega}{\pi} \int_0^{\frac{2\pi}{\omega}} \sin(n\omega t) P(t) dt \tag{A.17}$$

Plugging equation 14 into equation 12 gives

$$\begin{aligned}
& k_1 x_0 - A(m\omega^2 - k_1)\sin(\omega t) - \\
& \sum_{n=2}^{\infty} (n^2 m\omega^2 - k_1)[a_n \cos(n\omega t) + b_n \sin(n\omega t)] \\
& = A_0 + A_1 \cos(\omega t) + B_1 \sin(\omega t) + \sum_{n=2}^{\infty} A_n \cos(n\omega t) + B_n \sin(n\omega t)
\end{aligned} \tag{A.18}$$

Again, grouping like terms,

$$\begin{aligned}
& (A_0 - k_1 x_0) + A\left(m\omega^2 - k_1 + \frac{B_1}{A}\right)\sin(\omega t) + A_1 \cos(\omega t) + \\
& \sum_{n=2}^{\infty} \left\{ [a_n(n^2 m\omega^2 - k_1) + A_n] \cos(n\omega t) + [b_n(n^2 m\omega^2 - k_1) + B_n] \sin(n\omega t) \right\} = 0
\end{aligned} \tag{A.19}$$

Due to the orthogonality of Fourier series components, this is satisfied if and only if each term leading a sine or cosine is individually equal to 0, and if the constant term is 0, as well.

Note that the A_1 Fourier force term is not paired with a Fourier position term. For conservative forces, the A_1 force term is equal to zero, and is not a concern. In fact, a nonzero A_1 term is a valid definition of a nonconservative force. In order to find the change in energy of a system ΔE from a force P , one needs to integrate the force times distance:

$$\Delta E = \int_{x_1}^{x_2} \mathbf{P}(x, \dot{x}) \cdot d\mathbf{x} = \int_{t_1}^{t_2} \mathbf{P}(x, \dot{x}; t) \cdot \frac{d\mathbf{x}}{dt} dt \tag{A.20}$$

For a simple harmonic oscillator,

$$\frac{dx}{dt} = -A\omega \cos(\omega t) \tag{A.21}$$

and our integral in equation 20 is simplified to

$$\Delta E = \int -P(x, \dot{x}; t) A\omega \cos(\omega t) dt = -A\omega \int P(x, \dot{x}; t) \cos(\omega t) dt \tag{A.22}$$

This is just equation 16 for $n = 1$ times a factor of $(-A\pi)$.

Even for dissipative forces, the A_1 term does not produce a change in frequency, an offset, or any harmonics to first order, but is associated with damping, as will be shown below.

Another treatment that lends itself to a more explicit formulation of damping can be

found in Mike Bantel's thesis [18].

In equation 19, the first (constant) term determines the offset (or mean angle):

$$x_0 = \frac{A_0}{k_1} \quad (\text{A.23})$$

The second term (that of $\sin(\omega t)$) determines the frequency (and the frequency change coming from the perturbation):

$$\begin{aligned} \omega^2 &= \frac{k_1}{m} - \frac{B_1}{A m} = \omega_0^2 \left(1 - \frac{B_1}{A k_1} \right) \\ \frac{\Delta \omega^2}{\omega_0^2} &= \frac{\omega^2 - \omega_0^2}{\omega_0^2} = -\frac{B_1}{A k_1} \end{aligned} \quad (\text{A.24})$$

Keep in mind that A is the oscillation amplitude, while A_i and B_i are Fourier components of the perturbative force as a function of time.

The harmonics of the motion are given by

$$a_n = -\frac{A_n}{n^2 m \omega^2 - k_1} = -\frac{A_n}{m} \frac{1}{\left(n^2 \omega^2 - \frac{k_1}{m} \right)} = -\frac{A_n}{m} \frac{1}{(n^2 \omega^2 - \omega_0^2)} \approx -\frac{A_n}{k_1} \frac{1}{n^2 - 1} \quad (\text{A.25})$$

$$b_n = -\frac{B_n}{n^2 m \omega^2 - k_1} \approx -\frac{B_n}{k_1} \frac{1}{n^2 - 1} \quad (\text{A.26})$$

where in the previous two equations ω is approximated by ω_0 (which is a legitimate approximation to first order).

Equations 20–23 give the change in frequency, the change in equilibrium point, and all harmonics, so long as the solutions to equations 15–17 are provided. Later appendices will simply refer to these equations and plug in appropriate values.

We have now found the frequency shift and harmonics which result from small non-dissipative torque deviations from an ideal torsion pendulum. As noted earlier, our method is limited to non-dissipative torques. However, if there are dissipative torque components,

we can still find the rate at which the oscillator is damped, and equivalently find the oscillator's quality factor Q , as follows. Start with the undamped oscillation expressed in equation 4.

$$x(t) = A \sin(\omega_0 t) \quad (\text{A.4})$$

we need to find the energy dissipated over the course of a cycle by integrating

$$\begin{aligned} \Delta E &= \int_{\text{cycle}} P(x, \dot{x}) dx \\ &= \int_0^{\frac{2\pi}{\omega}} P(t) \frac{dx}{dt} dt \\ &= \int_0^{\frac{2\pi}{\omega}} P(t) A \omega \cos(\omega t) dt \\ &= A \pi \left[\left(\frac{\omega}{\pi} \right) \int_0^{\frac{2\pi}{\omega}} P(t) \cos(\omega t) dt \right] \\ &= A \pi A_1 \end{aligned} \quad (\text{A.27})$$

To find the effect on $1/Q$, we need to divide by the total energy of the system, and divide by 2π to find the fractional energy lost per radian, rather than per cycle:

$$\begin{aligned} \Delta \left(\frac{1}{Q} \right) &= - \frac{\Delta E}{2\pi E} \\ &= - \frac{A \pi A_1}{2\pi \left(\frac{1}{2} k_1 A^2 \right)} \\ &= - \frac{A_1}{k_1 A} \end{aligned} \quad (\text{A.28})$$

We have calculated $\Delta(1/Q)$, rather than simply Q , because of convenience: contributions to $1/Q$ add linearly.

Equation 25 and its exploration here brings up an issue that merits examination: the basic assumption of this perturbative method is that the motion of the oscillator is periodic, but obviously this is impossible when dissipative forces are present. Can failing to account

for the decaying oscillation lead to errors in the predicted harmonics? We will see that it should not, by examining the situation where a small perturbative force is added, and the complete solution can be found analytically: the case of “- b v” damping.

The force is expressed as

$$P(x) = -b \dot{x} = -b v \quad (\text{A.29})$$

Plugging this into equation 5, we see that

$$m \ddot{x} + b \dot{x} + k_1 x = 0 \quad (\text{A.30})$$

A solution to this equation is

$$x = A_0 e^{-\frac{b}{2m}t} \sin(\omega t), \quad \omega = \sqrt{\frac{k_1}{m} - \frac{b^2}{4m^2}} \quad (\text{A.31})$$

Define the time-dependent amplitude to be

$$A(t) = A_0 e^{-\frac{b}{2m}t} \quad (\text{A.32})$$

The lowest-order correction to the frequency from the damping term is (from A.28)

$$\delta \omega^2 = -\frac{b^2}{4m^2} \quad (\text{A.33})$$

which is second order in b; the first-order treatment described above should not return any change of frequency. The damping produces no harmonics, and 1/Q is given by

$$\begin{aligned} \Delta\left(\frac{1}{Q}\right) &= -\frac{\Delta E_{cycle}}{2\pi E} \\ &= -\frac{\frac{1}{2}k_1 \left[A^2\left(t=2\frac{\pi}{\omega}\right) - A^2(t=0) \right]}{\frac{1}{2}k_1 A^2(t=0)} \\ &= 1 - e^{-\frac{b}{m\omega}} \\ &\simeq \frac{b}{m\omega} \end{aligned} \quad (\text{A.34})$$

Next, consider what happens when we assume no amplitude decay and use the technique

described above. 28 is plugged into equation 14 to find the force harmonics:

$$P(t) = -b \dot{x} = -Ab\omega \cos(\omega t) \quad (\text{A.35})$$

The only nonzero force harmonic is

$$\begin{aligned} A_1 &= -Ab\omega \frac{\omega}{\pi} \frac{1}{2} \frac{2\pi}{\omega} \\ &= -Ab\omega \end{aligned} \quad (\text{A.36})$$

and all other force harmonics are 0.

As expected, the frequency doesn't change (to first order), nor are any harmonics generated to first order in b . The only nonzero quantity is $1/Q$:

$$\begin{aligned} \Delta\left(\frac{1}{Q}\right) &= -\frac{A_1}{k_1 A} \\ &= \frac{b\omega}{k_1} \\ &\simeq \frac{b}{m\omega} \end{aligned} \quad (\text{A.37})$$

So to first order in b , the exact treatment and the first-order approximation (assuming constant amplitude) give exactly the same results: no harmonics, no first-order change in frequency, and an identical contribution to $1/Q$ (since the change to $1/Q$ is a first-order effect).

Appendix B

First Order Perturbative Corrections to Simple Harmonic Oscillation from Nonlinear Conservative Fiber Torques

This appendix applies the methodology of Appendix A to the particular case where the torque is purely a function of angle, represented by a Taylor expansion about $\theta=0$. This will be applied to nonlinear torques on the torsion pendulum arising from properties of the torsion fiber.

Although the torsion fiber used in the G experiment does have velocity-dependent torques, a portion of its torques are velocity independent, and may be represented by the technique laid out in this appendix. This subset of nonlinear fiber torques are termed “conservative” fiber torques.

Consider a torque dominated by a linear term, perturbed by one small nonlinear term in θ , of degree m :

$$I \ddot{\theta} = -k_1 \theta - k_m \theta^m$$
$$\frac{k_m}{k_1} \ll 1$$
(B.1)

Because the k_1 term dominates, we can assume that the behavior is, to zero order in k_m ,

$$\theta(t) = A \sin(\omega_0 t)$$
(B.2)

with ω_0 being the frequency with $k_m = 0$. Perturbing this with the k_m term will potentially

create an offset, and additional harmonics, and a frequency to be determined later:

$$\theta(t) = A \sin(\omega t) + a_0 + \sum_{n=2}^{\infty} a_n \cos(n\omega t) + b_n \sin(n\omega t) \quad (\text{B.3})$$

The harmonics in equation 3 form a complete set.

Taking the second time derivative of equation 3,

$$\ddot{\theta}(t) = -A\omega^2 \sin(\omega t) - \omega^2 \sum_{n=2}^{\infty} n^2 [a_n \cos(n\omega t) + b_n \sin(n\omega t)] \quad (\text{B.4})$$

When solving for the non-fundamental harmonics in equations 3 and 4, we will only find the solution to first order in k_m :

$$\tau_{k_m}(\theta) = k_m [\theta(t)]^m \simeq k_m A^m \sin^m(\omega t) \quad (\text{B.5})$$

This approximation is valid for a first-order perturbation. From Appendix A, we can find the change in offset angle, change in frequency, and the amplitude of all non-fundamental harmonics if we find the Fourier coefficients of the torque given in equation 5.

To do this, we can make use of the formulas,

$$\begin{aligned} \sin^m(\omega t) = & \left(\frac{1}{2}\right)^m \frac{m!}{\left(\frac{m}{2}\right)! \left(\frac{m}{2}\right)!} \\ & + \left(\frac{1}{2}\right)^{m-1} \sum_{n=2,4,6,\dots}^m (-1)^{\frac{n}{2}} \frac{m!}{\left(\frac{m+n}{2}\right)! \left(\frac{m-n}{2}\right)!} \cos(n\omega t), \text{ m even} \end{aligned} \quad (\text{B.6})$$

$$\sin^m(\omega t) = \left(\frac{1}{2}\right)^{m-1} \sum_{n=1,3,5}^n (-1)^{\frac{n-1}{2}} \frac{m!}{\left(\frac{m+n}{2}\right)! \left(\frac{m-n}{2}\right)!} \sin(n\omega t), \text{ m odd} \quad (\text{B.7})$$

so the Fourier coefficients of the torque are (from Appendix A, equations A.15-17)

$$A_0 = -k_m A^m \left(\frac{1}{2}\right)^m \frac{m!}{\left(\frac{m}{2}\right)! \left(\frac{m}{2}\right)!}, \text{ m even} \quad (\text{B.8})$$

$$A_n = -k_m A^m \left(\frac{1}{2}\right)^{m-1} (-1)^{\frac{n}{2}} \frac{m!}{\left(\frac{m+n}{2}\right)! \left(\frac{m-n}{2}\right)!}, \text{ m and n even; } m \geq n > 0 \quad (\text{B.9})$$

$$A_n = 0, \text{ m or n odd} \quad (\text{B.10})$$

$$B_n = -k_m A^m \left(\frac{1}{2}\right)^{m-1} (-1)^{\frac{n-1}{2}} \frac{m!}{\left(\frac{m+n}{2}\right)! \left(\frac{m-n}{2}\right)!}, \text{ m and n odd; } m \geq n \geq 1 \quad (\text{B.11})$$

$$B_n = 0, \text{ m or n even} \quad (\text{B.12})$$

Plugging these into Appendix A, equations A.23-26, yields the following:

$$\theta_0 = \frac{A_0}{k_1} = -\frac{k_m}{k_1} A^m \left(\frac{1}{2}\right)^m \frac{m!}{\left(\frac{m}{2}\right)! \left(\frac{m}{2}\right)!}, \text{ m even} \quad (\text{B.13})$$

$$\frac{\Delta \omega^2}{\omega^2} = -\frac{B_1}{A k_1} = \frac{k_m}{k_1} A^{m-1} \left(\frac{1}{2}\right)^{m-1} \frac{m!}{\left(\frac{m+1}{2}\right)! \left(\frac{m-1}{2}\right)!} \quad (\text{B.14})$$

$$a_n = -\frac{A_n}{k_1} \frac{1}{n^2-1} = \frac{k_m}{k_1} \frac{A^m}{n^2-1} \left(\frac{1}{2}\right)^{m-1} (-1)^{\frac{n}{2}} \frac{m!}{\left(\frac{m+n}{2}\right)! \left(\frac{m-n}{2}\right)!} \quad (\text{B.15})$$

(m and n even, n > 0)

$$b_n = -\frac{B_n}{k_1} \frac{1}{n^2-1} = \frac{k_m}{k_1} \frac{A^m}{n^2-1} \left(\frac{1}{2}\right)^{m-1} (-1)^{\frac{n-1}{2}} \frac{m!}{\left(\frac{m+n}{2}\right)! \left(\frac{m-n}{2}\right)!} \quad (\text{B.16})$$

(m and n odd, n > 1)

$$a_n = b_n = 0 \text{ for all other values of m, n} \quad (\text{B.17})$$

Using Appendix A, equation A.28, we can confirm that this is a conservative torque: no energy is dissipated, shown by the fact that $A_1 = 0$.

From equations 15 and 16, we can see some characteristic effects of a θ^m torque. Most obviously, an even-m torque will produce only even cosine harmonics, while an odd-

m torque will produce odd sine harmonics. An even m torque will produce an offset angle, but will not affect the frequency, while an odd m torque will not produce any offset, but will affect the frequency.

It makes intuitive sense that even-m torques would produce an offset, as they torque the oscillator in the same direction for both positive and negative θ . It also makes sense that they should not, to lowest order, affect the frequency, as they are not inherently restorative, and “push” first towards and then away from equilibrium as the oscillator passes through the equilibrium point.

Lastly, all harmonics, plus the angle offset or frequency shift, are clearly amplitude dependent, approaching zero as the amplitude approaches zero. This also makes sense, as the higher order torques will vanish more quickly than the linear torque as $\theta \rightarrow 0$, leaving only a simple harmonic oscillator for any sufficiently small angle.

Table 1 presents the effect of torque perturbations on the form of equation 1, through $m=7$, below.

Table B.1: Sample Offset, Change of Frequency, and Harmonics
of k_m through $m = 7$

m	a_0	a_2	a_4	a_6
2	$-(A^2 k_2) / (2 k_1)$	$-(A^2 k_2) / (6 k_1)$		
4	$-(3 A^4 k_4) / (8 k_1)$	$-(A^4 k_4) / (6 k_1)$	$(A^4 k_4) / (120 k_1)$	
6	$-(5 A^6 k_6) / (16 k_1)$	$-(5 A^6 k_6) / (32 k_1)$	$(A^6 k_6) / (80 k_1)$	$-(A^6 k_6) / (1120 k_1)$

m	$\Delta\omega^2/\omega_0^2$	b_3	b_5	b_7
3	$(3 A^2 k_3) / (4 k_1)$	$-(A^3 k_3) / (32 k_1)$		
5	$(5 A^4 k_5) / (8 k_1)$	$-(5 A^5 k_5) / (128 k_1)$	$(A^5 k_5) / (384 k_1)$	
7	$(35 A^6 k_7) / (64 k_1)$	$-(21 A^7 k_7) / (512 k_1)$	$(7 A^7 k_7) / (1536 k_1)$	$-(A^7 k_7) / (3072 k_1)$

Appendix C

Conservative Field Torques: Offset, Harmonics, Frequency Shift, Calculation of Coefficients, and Symmetries

This Appendix applies the technique laid out in Appendix A to the special case where the forces are periodic in x (or torques periodic in θ). It concludes with a discussion of symmetries of spherical harmonic representations. The technique from Appendix A is used to consider non-linear torques arising from the pendulum's interaction with static ambient fields. Such fields might be Newtonian gravitation, electrostatic or magnetostatic forces, or indeed a new force in nature. In these cases the torque acting on the pendulum is necessarily a periodic function of the rotation angle of the pendulum. Thus,

$$I \ddot{\theta} = -k_1 \theta + \tau_{field}(\theta) \quad (C.1)$$

where

$$\tau_{field}(\theta) = - \sum_{m=1}^{\infty} \alpha_m \cos(m\theta) + \beta_m \sin(m\theta) \quad (C.2)$$

The minus sign is chosen in order to make this derivation consistent with the notation for other forces, such as the nonlinear conservative fiber torques in Appendix B.

If the perturbing torque is small, we may assume a dominant sinusoidal behavior for the pendulum,

$$\theta_0(t) = A \sin(\omega_0 t) \quad (C.3)$$

We now replace θ in the right-hand side of equation 2 with the approximate $\theta_0(t)$ given in equation 3. Then,

$$\tau_{field}(A, \omega, t) \approx - \sum_{m=1}^{\infty} \alpha_m \cos[m A \sin(\omega_0 t)] + \beta_m \sin[m A \sin(\omega_0 t)] \quad (C.4)$$

The formalism in Appendix A involves breaking this down into its Fourier components,

$$\begin{aligned} \tau(t) &= \tau(\theta(t), \dot{\theta}(t)) = \tau(\theta(t)) \simeq \tau(A \sin(\omega_0 t)) \\ \tau(t) &\simeq A_0 + \sum_{n=1}^{\infty} A_n \cos(n \omega_0 t) + B_n \sin(n \omega_0 t) \end{aligned} \quad (C.5)$$

Applying equations A.15-17 of Appendix A,

$$\begin{aligned} A_0 &= \frac{\omega}{2\pi} \int_0^{\frac{2\pi}{\omega}} \tau(t) dt \\ &= \frac{\omega}{2\pi} \int_0^{\frac{2\pi}{\omega}} \sum_{m=1}^{\infty} -[\alpha_m \cos[m A \sin(\omega t)] + \beta_m \sin[m A \sin(\omega t)]] dt \\ &= - \sum_{m=1}^{\infty} \alpha_m J_0(m A) \end{aligned} \quad (C.6)$$

$$\begin{aligned} A_{n>0} &= \frac{\omega}{\pi} \int_0^{\frac{2\pi}{\omega}} \tau(t) \cos(n \omega t) dt \\ &= \frac{\omega}{\pi} \int_0^{\frac{2\pi}{\omega}} \sum_{m=1}^{\infty} -[\alpha_m \cos[m A \sin(\omega t)] + \beta_m \sin[m A \sin(\omega t)]] \cos(n \omega t) dt \\ &= - \sum_{m=1}^{\infty} 2 \alpha_m J_n(m A), \text{ n even} \\ &= 0, \text{ n odd} \end{aligned} \quad (C.7)$$

$$\begin{aligned} B_n &= \frac{\omega}{\pi} \int_0^{\frac{2\pi}{\omega}} \tau(t) \sin(n \omega t) dt \\ &= \frac{\omega}{\pi} \int_0^{\frac{2\pi}{\omega}} \sum_{m=1}^{\infty} -[\alpha_m \cos[m A \sin(\omega t)] + \beta_m \sin[m A \sin(\omega t)]] \sin(n \omega t) dt \\ &= - \sum_{m=1}^{\infty} 2 \beta_m J_n(m A), \text{ n odd} \\ &= 0, \text{ n even} \end{aligned} \quad (C.8)$$

The above expressions for A_n and B_n may now be plugged into equations A.25-28 from

Appendix A to yield the resultant angular offset, the change in frequency, and the Fourier coefficients a_n and b_n that describe the harmonics in the motion of the pendulum. The pendulum's motion is changed from that given in equation 3 to

$$\theta(t) = A \sin(\omega t) + \theta_0 + \sum_{n=2}^{\infty} a_n \cos(n \omega t) + b_n \sin(n \omega t) \quad (\text{C.9})$$

The formulas for the offset, frequency, and harmonics are

$$\theta_0 = \frac{A_0}{k_1} = \sum_{m=1}^{\infty} -\frac{\alpha_m}{k_1} J_0(mA) \quad (\text{C.10})$$

$$\frac{\Delta \omega^2}{\omega^2} = -\frac{B_1}{A k_1} = \sum_{m=1}^{\infty} \frac{\beta_m}{k_1} \frac{2 J_1(mA)}{A} \quad (\text{C.11})$$

$$a_n = -\frac{A_n}{k_1} \frac{1}{n^2 - 1} = \sum_{m=1}^{\infty} \frac{\alpha_m}{k_1} \frac{2 J_n(mA)}{(n^2 - 1)}, \text{ n even} \\ = 0, \text{ n odd} \quad (\text{C.12})$$

$$b_n = -\frac{B_n}{k_1} \frac{1}{n^2 - 1} = \sum_{m=1}^{\infty} \frac{\beta_m}{k_1} \frac{2 J_n(mA)}{n^2 - 1}, \text{ n odd} \\ = 0, \text{ n even} \quad (\text{C.13})$$

As shown in Appendix A, equation A.28, the contribution to $1/Q$ is proportional to A_1 , which is zero. No energy is dissipated by static field interactions.

So far, this treatment applies to torques arising from any sort of static field interactions. A case of particular importance in this thesis is the gravitational interaction of a pendulum with ambient mass distributions. We will now show how to find the coefficients α_m and β_m first introduced in equation 2 in terms of the mass distributions of a pendulum and its environment.

Consider a pendulum with mass distribution $\rho_p(\mathbf{x})$ with \mathbf{x} close to the origin. It is in the presence of a scalar potential $\Phi(\mathbf{x})$, generated by a more distant mass source distribution $\rho_s(\mathbf{x})$. The potential energy of the system is:

$$U = \int \rho_p(\mathbf{x}) \Phi(\mathbf{x}) dV_p = -G \int \rho_s(\mathbf{x}') \int \rho_p(\mathbf{x}) \frac{1}{|\mathbf{x} - \mathbf{x}'|} dV_p dV'_s \quad (\text{C.14})$$

For $|\mathbf{x}| < |\mathbf{x}'|$, the $1/|\mathbf{x} - \mathbf{x}'|$ portion can be expanded into its spherical harmonic representation,

$$\frac{1}{|\mathbf{x} - \mathbf{x}'|} = \sum_{l=0}^{\infty} \sum_{m=-l}^l \sum_{l'=0}^{\infty} \sum_{m'=-l'}^{l'} \frac{4\pi}{2l'+1} \frac{r^l}{r'^{l'+1}} Y_{lm}^*(\theta, \phi) Y_{l'm'}(\theta', \phi') \delta_{l'l} \delta_{m'm} \quad (\text{C.15})$$

Plugging equation 15 into equation 14 yields

$$U = \left[\sum_{l=0}^{\infty} \sum_{m=-l}^l \int \rho_p(\mathbf{x}) r^l Y_{lm}^*(\theta, \phi) dV_p \right] * \left[\sum_{l'=0}^{\infty} \sum_{m'=-l'}^{l'} -\frac{4\pi G}{2l'+1} \int \frac{\rho_s(\mathbf{x}')}{r'^{l'+1}} Y_{l'm'}(\theta', \phi') dV'_s \delta_{l'l} \delta_{m'm} \right] \quad (\text{C.16})$$

First, going through the primed summations (and eliminating the Kronecker δ 's),

$$U = \sum_{l=0}^{\infty} \sum_{m=-l}^l \left[\int \rho_p(\mathbf{x}) r^l Y_{lm}^*(\theta, \phi) dV_p \right] \left[-\frac{4\pi G}{2l+1} \int \frac{\rho_s(\mathbf{x}')}{r'^{l+1}} Y_{lm}(\theta', \phi') dV'_s \right] \quad (\text{C.17})$$

Note that equation 17 is separable into two integrals, with a single summation over l and m .

Defining the pendulum mass multipole moments to be

$$q_{lm} = \int \rho_p(\mathbf{x}) r^l Y_{lm}^*(\theta, \phi) dV_p \quad (\text{C.18})$$

and the field multipole to be

$$a_{lm} = -\frac{4\pi G}{2l+1} \int \frac{\rho_s(\mathbf{x}')}{r'^{l+1}} Y_{lm}(\theta', \phi') dV'_s \quad (\text{C.19})$$

yields

$$U = \sum_{l=0}^{\infty} \sum_{m=-l}^l q_{lm} a_{lm} \quad (\text{C.20})$$

Next, consider what happens when the test mass undergoes a rotation about the z -axis by an angle, ψ . We will (for convenience) take the z -axis to be along the axis of rotation of the pendulum, and roughly parallel to the fiber.

$$q_{lm} \rightarrow q_{lm}' = \int \rho(r, \theta, \phi - \psi) r^l Y_{lm}^*(\theta, \phi) d\mathbf{r} \quad (\text{C.21})$$

Using the relation

$$Y_{lm}^*(\theta, \phi) = Y_{lm}^*(\theta, \phi - \psi) e^{-im\psi} \quad (\text{C.22})$$

it becomes clear that

$$\begin{aligned} q_{lm}' &= \int \rho(r, \theta, \phi - \psi) r^l Y_{lm}^*(\theta, \phi - \psi) e^{-im\psi} d\mathbf{r} \\ &= e^{-im\psi} \int \rho(r, \theta, \phi - \psi) r^l Y_{lm}^*(\theta, \phi - \psi) d\mathbf{r} \\ &= e^{-im\psi} q_{lm} \end{aligned} \quad (\text{C.23})$$

So, when the pendulum is rotated by an angle ψ about the z-axis, the potential energy becomes

$$V(\psi) = \sum_{l=0}^{\infty} \sum_{m=-l}^l q_{lm} a_{lm} e^{-im\psi} \quad (\text{C.24})$$

with an associated torque of

$$\tau_z(\psi) = -\frac{\partial V}{\partial \psi} = \sum_{l=0}^{\infty} \sum_{m=-l}^l i m q_{lm} a_{lm} e^{-im\psi} \quad (\text{C.25})$$

Next, consider the symmetry of $m \rightarrow -m$.

Using the relation from spherical harmonics,

$$Y_{lm}^*(\theta, \phi) = (-1)^m Y_{l-m}(\theta, \phi) \quad (\text{C.26})$$

yields the following:

$$\begin{aligned} q_{lm} a_{lm} &= -\frac{4\pi G}{2l+1} \int \int \rho_s(\mathbf{r}') \rho(\mathbf{r}) \frac{r'^l}{r'^{l+1}} Y_{lm}(\theta', \phi') Y_{lm}^*(\theta, \phi) d\mathbf{r}' d\mathbf{r} \\ &= -\frac{4\pi G}{2l+1} \int \int \rho_s(\mathbf{r}') \rho(\mathbf{r}) \frac{r'^l}{r'^{l+1}} Y_{l-m}^*(\theta', \phi') Y_{l-m}(\theta, \phi) d\mathbf{r}' d\mathbf{r} \\ &= q_{l-m}^* a_{l-m}^* \end{aligned} \quad (\text{C.27})$$

Summing the torque listed in equation 24 from both the +m and -m terms and using equation 26,

$$\begin{aligned}
\tau_{lm} + \tau_{l-m} &= (i)(m)q_{lm}a_{lm}e^{-im\psi} + (i)(-m)q_{l-m}a_{l-m}e^{im\psi} \\
&= (i)(m)q_{lm}a_{lm}e^{-im\psi} + (-i)(m)q_{lm}^*a_{lm}^*e^{im\psi} \\
&= (i)(m)q_{lm}a_{lm}e^{-im\psi} + \text{complex conjugate} \\
&= 2\Re(imq_{lm}a_{lm}e^{-im\psi})
\end{aligned} \tag{C.28}$$

So, combining equations 28 and 25, the field torques are:

$$\tau_z(\psi) = \sum_{l=1}^{\infty} \sum_{m=1}^l 2\Re(imq_{lm}a_{lm}e^{-im\psi}) \tag{C.29}$$

As expected, this is a set of sines and cosines of the angle of rotation. Comparing equation 29 with equation 4 yields the following relations:

$$\begin{aligned}
\alpha_m &= \sum_{l=m}^{\infty} 2m\Im(q_{lm}a_{lm}) \\
\beta_m &= -\sum_{l=m}^{\infty} 2m\Re(q_{lm}a_{lm})
\end{aligned} \tag{C.30}$$

Symmetries of the the Spherical Harmonic Representation

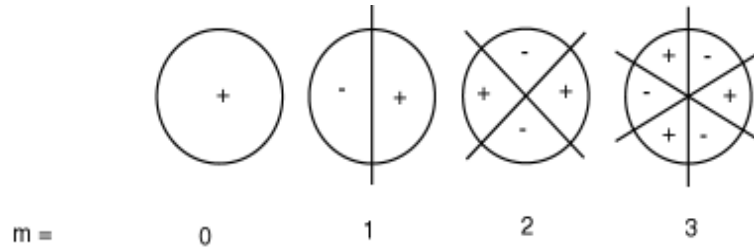
There are a number of simple rules that are useful in thinking about spherical harmonics, and functions of circular symmetry. The first relates to the “m” coefficient in the $q_{lm}a_{lm}$ formulation or, equivalently, the Y_{lm} formulation. The Y_{lm} term can be broken down into two parts, a polar dependence and an azimuthal dependence.

$$Y_{lm}(\theta, \phi) = P_{lm}(\cos \theta) e^{im\phi} \tag{C.31}$$

The $e^{im\phi}$ term has m “nodes” where, $\Re(e^{im\phi}) = 0$, and the real part flips sign from one side of the node to the other. Similarly for the imaginary part, though the imaginary nodes will bisect the angles formed by the real nodes, and vice-versa. Because these nodes are evenly spaced, it is very easy to conceptualize.

Figure C.1 Symmetry in $\text{Re}(e^{im\phi})$

(facing toward the $-z$ direction)



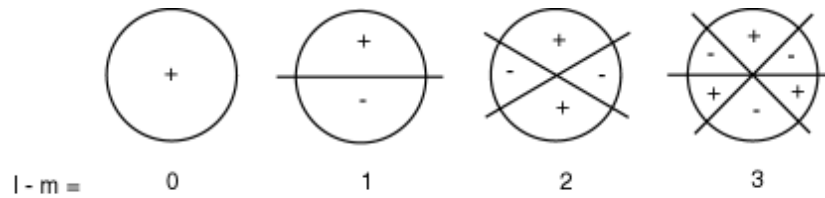
Because each Newtonian moment (q_{lm} or a_{lm}) includes an integration over $e^{im\phi}$, the term will be zero if either the source mass, or the test mass, has an azimuthal symmetry that $e^{im\phi}$ does not match. By looking at Figure 1, it is easily seen that a rectangular pendulum with an oblong cross section will not produce any odd- m terms, only even- m . A square pendulum (that is, square in the x - y plane) will not produce any moments of $m=1, 2$, or 3 , but only those that are divisible by 4 (ie, $m = 0, 4, 8, 12, \dots$). A pendulum with the cross section of an equilateral triangle, on the other hand, will only produce nonzero moments q_{lm} where m is divisible by 3 (ie, $m = 0, 3, 6, 9, \dots$).

The UCI G measurement has (to within fabrication errors) a two-fold pendulum symmetry. Ie, it is invariant under a 180 degree rotation about the torsion (z) axis, so it couples primarily to gravitational field moments with even m . And because the ring source masses have a two-fold symmetry (again, to within fabrication errors), the source masses will *produce* primarily gravitational multipole moments of even m .

Conceptualizing the role that the “ l ” terms play in Y_{lm} is a more intricate business, as the $P_{lm}(\cos\theta)$ terms are not as simple as the $e^{im\phi}$ ones. The polar symmetry is actually determined not by l , but by the value of $(l-m)$. This number, $(l-m)$, is the number of nodal values of θ , distributed symmetrically about $\theta = \pi/2$. At these nodes, $P_{lm}(\cos \theta) = 0$. The

function will be either even or odd, in flips about $\theta = \pi/2$, just like $\cos^n\theta$. Figure 2 shows a few special cases of this symmetry, with only relative factors of -1 about the polar angle shown, for fixed ϕ . The actual function is complex at any given polar angle, due to the effect of the $e^{im\phi}$ term. Lastly, the actual angles between the nodal lines vary for different values of l and m , and do not lend themselves to easy memorization; the only thing that is obvious about them, is that they are distributed symmetrically about $\theta = \pi/2$.

Figure C.2: Node Representation of $P_m(\cos\theta)$, as a Function of Polar Angle, θ



When looking at the q_{42} moment, for example, $(l-m) = (4-2)=2$, it is apparent that the magnitude of this term is maximized for either an extremely tall, narrow mass, or an extremely squat, wide mass. It is not obvious from this picture precisely which ratio of height to width would null the 4,2 moment; that would require a formal calculation of the geometry.

Appendix D

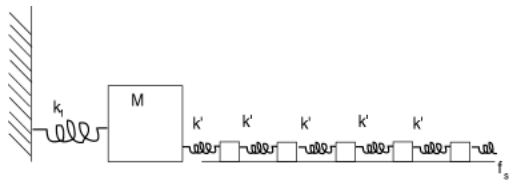
The Stick-Slip Model

Studies at the UCI Gravity Lab have found evidence of a “stick-slip” behavior in torsion pendulums, which has a significant effect on the fiber's harmonics as well as the Q of its oscillation. In order to explore this effect, we will begin with a linear (rather than rotational) toy model.

Consider single massive block, coupled to a wall by a spring of constant k_1 , and also coupled to the first of an infinite line of massless blocks, each attached to its adjacent blocks by a spring of constant k_{ss} , as shown in Figure 1

Figure D.1

Blocks in a 1-Dimensional Parallel Stick-Slip Model



Note that in this linear model, the stick-slip blocks, and the stick-slip force, are “in parallel” with the k_1 force. The stick-slip system and the “ k_1 ” spring are both acting

independently on the mass, M . A torsion system that would physically represent this “parallel” system would be a pair of fibers represented by concentric hollow cylinders, one of which has a stick-slip behavior, and the other of which has a linear behavior, and neither of which touch each other (hence the fact that they are in parallel). This distinction is made now because, later on in this appendix, a “series” stick-slip system will be introduced. We will now proceed to find the force on the massive block M from the k' spring attached to it.

In this “parallel” stick-slip system, each of the massless blocks, when moved, experiences a force of friction opposite its movement, of magnitude f_{ss} . This frictional force is independent of velocity, and will serve to keep the block fixed in place if the absolute value of the sum of all other forces on the block is less than f_{ss} .

Define the distance between stick-slip block i and the wall as x_i , with x being the position of the massive block. The force on the massless stick-slip block i will then be

$$F_i(x_{i-1}, x_i, x_{i+1}) = -k'[(x_i - x_{i-1}) - (x_{i+1} - x_i)] = k'(x_{i+1} + x_{i-1} - 2x_i) \quad (D.1)$$

and the force on the massive block M at position x due to the stick-slip perturbation will be

$$F_{ss}(x, x_1) = -k'(x - x_1) \quad (D.2)$$

Let us also define the a fundamental unit of length for this system,

$$\Delta x \equiv \frac{f_{ss}}{k'} \quad (D.3)$$

Given a system with $x = 0$ and all $x_i = 0$, this is simply the maximum amount you could move any one block (including the massive block) without moving any of the others.

Note that, in order for this system to behave like a simple harmonic oscillator, to 0th order in k_{ss} , there would have to be a restriction, namely,

$$F_{ss}(x = A) \ll k_1 A; \quad (D.4)$$

In the simplest case, consider what would happen if the largest block were to

oscillate at an amplitude $A = \Delta x$, with $x_1(t) = 0$ (ie, the first stick-slip block never moves).

In that case, the nearest block would never move, no energy would be dissipated by the system, and the stick-slip force equation would be trivial:

$$F_{ss}(x) = -k'x \quad (D.5)$$

Next, consider what would happen if the amplitude of the oscillation of M were large enough to move the first stick-slip block a maximum distance of Δx from its equilibrium point, or just enough so that block 2 does not move at all.

The following analyses will only apply to circumstances where block M moves monotonically from some negative extremum to some maximum, stops, and then moves monotonically back to its negative extremum, etc. This is because the stick-slip force on block M, as a function of position, will be a hysteresis loop, and any motion that does not behave in this monotonic fashion will explore the interior of this loop, rather than the perimeter. Such behavior is beyond the scope of this derivation.

At $t=0$, both block M and block 1 are at their negative extrema, with block M's coordinate,

$$x(0) = -A = -2\Delta x \quad (D.6)$$

and about to begin moving in a positive direction. Block 2 will be at

$$x_2(t) = 0 \text{ for all } t \quad (D.7)$$

since it does not move. Block 1 will be at the maximum negative displacement possible without moving block 2:

$$x_1(t=0) = -\Delta x + x_2 = -\Delta x \quad (D.8)$$

and by equations 1, 7, and 8,

$$\frac{F_1(t=0)}{k'} = -\frac{f_{ss}}{k'} = -\Delta x = x_2 + x(0) - 2x_1(0) = x(0) + 2\Delta x; \quad (D.9)$$

$$x(0) = -3\Delta x$$

As block M is moved to the right, the force will at first be described by the equation,

$$F_{ss}(x; v > 0) = k'(x_1 - x) = k'(-\Delta x - x) \quad (D.10)$$

$$= -k'(x + \Delta x), \quad -3\Delta x \leq x \leq -\Delta x$$

Once x reaches $-\Delta x$, block 1 will begin to slip from its position. Once block 1 begins to slip, the stick-slip force upon block M will depend on the value of x_1 . From this point onwards, the force on block 1 will be $+k_{ss}\Delta x$, and by equation 1,

$$F_1 = k'\Delta x = k'(x_2 + x - 2x_1) = k'*(x - 2x_1) \quad (D.11)$$

or

$$x_1(x; v > 0) = \frac{x - \Delta x}{2}, \quad -\Delta x \leq x \leq 3\Delta x \quad (D.12)$$

Thus the force on block M is (by equations 2 and 12)

$$F_{ss}(x; v > 0) = -k'(x - x_1) = -k'\left(x - \frac{x - \Delta x}{2}\right) = -k'\left(\frac{x + \Delta x}{2}\right), \quad -\Delta x \leq x \leq 3\Delta x \quad (D.13)$$

So, from equation 13, we have the stick-slip force on the massive block for a single slipping block as a function of position for the positive velocity portion of the oscillation.

For the negative velocity part of the oscillation, by a similar technique,

$$F_{ss}(x; v < 0) = -k(x - \Delta x), \quad \Delta x \leq x \leq 3\Delta x \quad (D.14)$$

and

$$F_{ss}(x; v < 0) = -k'\left(\frac{x - \Delta x}{2}\right), \quad -3\Delta x \leq x \leq \Delta x \quad (D.15)$$

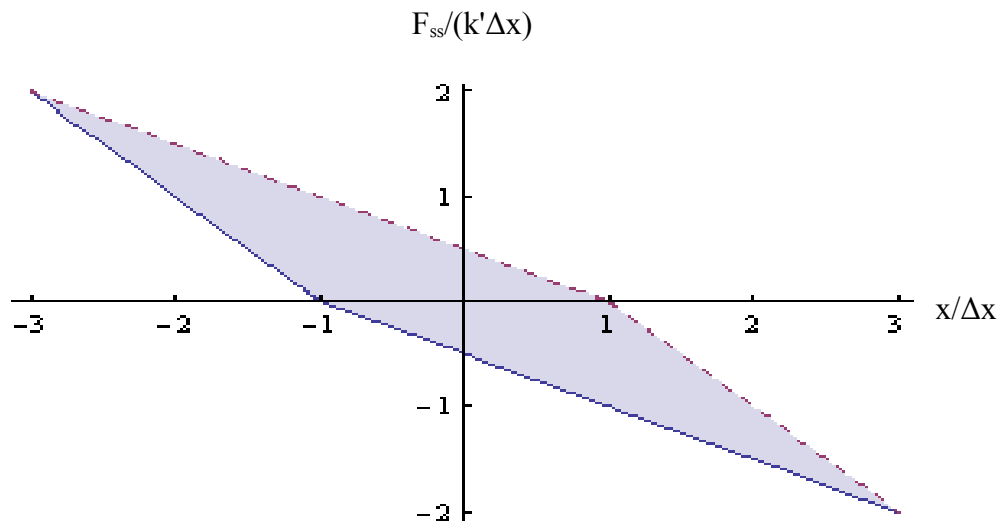
The amount of energy dissipated by this system is simply the integral of the force over these four regions:

$$\begin{aligned}
\Delta E &= \int_{-3\Delta x}^{-\Delta x} k'(x+\Delta x) dx + \int_{-\Delta x}^{3\Delta x} k'\left(\frac{x+\Delta x}{2}\right) dx \\
&+ \int_{3\Delta x}^{\Delta x} -k'(x-\Delta x) + \int_{\Delta x}^{-3\Delta x} -k'\left(\frac{x-\Delta x}{2}\right) dx \\
&= k' \Delta x^2 [(2)+(-4)+(2)+(-4)] \\
\Delta E &= -4k' \Delta x^2
\end{aligned}
\tag{D.16}$$

This result makes intuitive sense, as the force on block 1 as it slides is $-k' \Delta x = -f_{ss}$, and it slides a total distance of $4 \Delta x$, equal to twice its peak-to-peak amplitude of oscillation. This is shown graphically in Figure 2.

Figure D.2

Stick-Slip Force for a One Slipping Block System



Note that a hysteresis loop has already emerged from this simple model. The area of this loop is the energy dissipated, as calculated in equation 16.

Next, consider the case where N of the stick-slip blocks move as the massive block M oscillates between its extrema.

The Nth block will have an amplitude of Δx , like block 1 in the above example. The (N-1)th block has an amplitude of $3 \Delta x$ like the massive block in the above example, the (N-2) block must (by equation 1) have an amplitude of $6 \Delta x$, and the (N-3) block $10 \Delta x$, etc.

The (N-n)th block will slide a peak-to-peak amount of twice its amplitude,

$$\max(x_{N-n}) - \min(x_{N-n}) = (n+1)(n+2) \Delta x \quad (\text{D.17})$$

By equation 17, block M (at position $0 = N-N$) will oscillate with an amplitude of

$$A = (N+1) \frac{(N+2)}{2} \Delta x \quad (\text{D.18})$$

Consider what will happen when the massive block is at the negative extremum, as it begins to move with positive velocity. It will at first experience a force,

$$\begin{aligned} F_{ss}(-A) &= k'(x_{1\min} - x_{0\min}) = k' \Delta x \left\{ -N \frac{(N+1)}{2} - \left[-(N+1) \frac{(N+2)}{2} \right] \right\} \\ &= k' \Delta x \left[-\frac{N^2+N}{2} + \frac{N^2+3N+2}{2} \right] = (N+1) k' \Delta x \\ F_{max} &\equiv (N+1) k' \Delta x \end{aligned} \quad (\text{D.19})$$

Equation 19 should be intuitively obvious: N+1 springs are under compression, with the tension stepping up by exactly $k' \Delta x$ on each successive spring, and the final spring exerts its force on the massive block, expressed as F_{ss} .

As the massive block begins to move, this force will diminish linearly for a distance $2 \Delta x$. By equation 2,

$$F_{ss}(x; v > 0) = -k' [(N+1) \Delta x - (x+A)], \quad -A \leq x \leq -A + 2 \Delta x \quad (\text{D.20})$$

at which point the first massless block will begin to slip, generating a new, slightly more shallow slope, until the second block begins to slip, which will generate an even shallower slope. The net force on any slipping block is $+k' \Delta x$. So, for block 1, using equation 1,

$$F_1(x_1, x_2, x) = k' \Delta x = k'(x_2(t) + x(t) - 2x_1(t)) \quad (\text{D.21})$$

which yields

$$x_1(x_2, x) = \frac{1}{2}(x_2 + x - \Delta x) \quad (\text{D.22})$$

Plugging equation 2 into equation 22 yields

$$F_{ss}(x; v > 0) = \frac{-k}{2}(x(t) - x_2(0) + \Delta x), -A + 2\Delta x \leq x_0 \leq -A + 6\Delta x \quad (\text{D.23})$$

In equation 23, we have eliminated the explicit dependence upon the position of the moving block, x_1 , and only look at the position of x_2 , which is fixed over this region. A repeated application of this method produces a telescoping series revealing F_{ss} , such that when block m breaks free,

$$F_{ss}(x, m; v > 0) = \left[\left(\frac{x_{(m+1)}(t=0)}{m+1} - \frac{m\Delta x}{2} \right) - \frac{x_0}{m+1} \right] k', \quad -A + m(m+1)\Delta x \leq x_0 \leq -A + (m+1)(m+2)\Delta x \quad (\text{D.24})$$

where, by equation 18,

$$A = (N+1) \frac{(N+2)}{2} \Delta x \quad (\text{D.25})$$

and, using equation 17,

$$x_m(t=0) = x_m(t < t_m) = -(N-m+1) \frac{(N-m+2)}{2} \Delta x \quad (\text{D.26})$$

until the block begins to move at time t_m .

When looking at the change in F_{ss} over this range, we can look at the change in force between the beginning and end of the range. For instance,

$$\Delta F_{ss}(m=0) = 2\Delta x k' - 0\Delta x k' = 2\Delta x k' \quad (\text{D.27})$$

While, for $m = 1$,

$$\Delta F_{ss}(m=1) = \frac{1}{2}(6\Delta x - 2\Delta x) k' = 2\Delta x k' \quad (\text{D.28})$$

In general, using the maximum and minimum values of x in equation 23,

$$\begin{aligned}\Delta F_{ss}(m) &= \frac{1}{m+1}(-A+(m+1)(m+2)\Delta x + A-m(m+1)\Delta x)k' \\ &= \frac{\Delta x k'}{m+1}(m^2+3m+2-m^2-m)=2\Delta x k'\end{aligned}\quad (D.29)$$

which leads to

$$F_{ss}(m, v>0) = F_{max} - \sum_{i=0}^m 2\Delta x k' = [(N+1)-2m]\Delta x k' \quad (D.30)$$

Thus, the stick-slip force is linear in m, the number of blocks that have broken free.

Equivalently,

$$\begin{aligned}F_{ss}(m, v>0) &= F_{max} - \sum_{i=0}^m 2\Delta x k' = [(N+1)-2m]\Delta x k' \\ m &= \frac{N+1}{2} - \frac{F_{ss}}{2k'\Delta x} \\ m &= \frac{F_{max} - F_{ss}}{2k'\Delta x}\end{aligned}\quad (D.31)$$

Finding the average value of x(m),

$$\begin{aligned}\bar{x}(m, v>0) &= \frac{1}{2}[-A+(m+1)(m+2)\Delta x - A+m(m+1)\Delta x] \\ &= -A+(m^2+2m+1)\Delta x \\ &= [-\frac{1}{2}(N+1)(N+2)\Delta x + (m+1)^2\Delta x]\end{aligned}\quad (D.32)$$

Combining equations 31 and 32 to eliminate m and find x as a function of F_{ss} ,

$$\begin{aligned}x(F_{ss}, v>0) &= -\frac{1}{2}(N+1)^2\Delta x - \frac{(N+1)}{2}\Delta x + (m^2+2m+1)\Delta x \\ &= -\frac{F_{max}^2}{2k'^2\Delta x} + \frac{F_{max}^2}{4k'^2\Delta x} + \frac{F_{ss}^2}{4k'^2\Delta x} - \frac{F_{ss}F_{max}}{2k'^2\Delta x} + \frac{F_{max}}{k'} - \frac{F_{ss}}{k'} + \Delta x \\ &= \frac{-F_{max}^2}{4k'^2\Delta x} + \frac{F_{ss}^2}{4k'^2\Delta x} - \frac{F_{ss}F_{max}}{2k'^2\Delta x} + \frac{F_{max}}{k'} - \frac{F_{ss}}{k'} + \Delta x \\ x(F_{ss}, v>0) &\approx \frac{1}{4k'^2\Delta x}[F_{max}^2 - F_{ss}^2 - 2F_{ss}F_{max}]\end{aligned}\quad (D.33)$$

When the force is a maximum, pushing to the right, the position is at the negative

extremum, and vice versa.

More generally,

$$x(F_{ss}) \approx -\frac{1}{4k'^2 \Delta x} [2F_{ss} F_{max} + \hat{v}(F_{ss}^2 - F_{max}^2)] \quad (D.34)$$

This is confirmed by an independent derivation [18, p. 98]. It can be re-expressed as

$$F_{ss}(x) = -\hat{v}(F_{max} - \sqrt{2F_{max}^2 - \hat{v}4k'^2(\Delta x)x}) \quad (D.35)$$

Setting $x = A$ to find F_{max} gives us

$$F_{max} = k' \sqrt{2A \Delta x} \quad (D.36)$$

yielding a better version of equation 35:

$$F_{ss}(x) = -\hat{v}(k' \sqrt{2A \Delta x} - 2k' \sqrt{\Delta x} \sqrt{A - \hat{v}x}) \quad (D.37)$$

Let us now define, for the parallel stick-slip case,

$$k_{ss} = k' \sqrt{2 \Delta x} \quad (D.38)$$

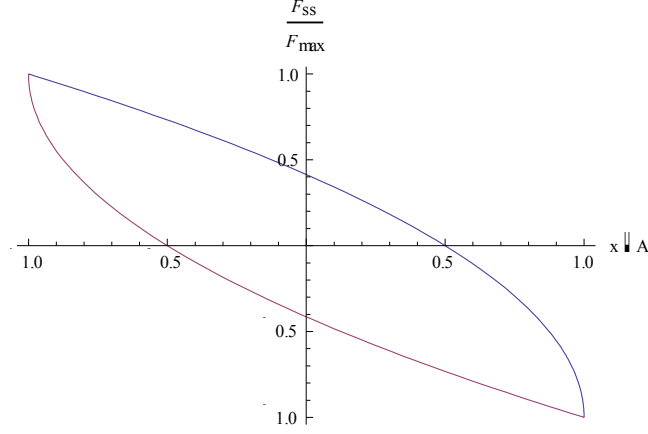
and rewrite equation 37 as

$$F_{ss}(x, \hat{v}) = -\hat{v}(k_{ss} \sqrt{A} - \sqrt{2} k_{ss} \sqrt{A - \hat{v}x}) \quad (D.39)$$

Here is a plot of equation 39:

Figure D.3

$F_{ss}(x)$ for a Large Number of
Stick-Slip Blocks



This linear system can easily be generalized to a torsion system, with a series of zero-inertia cylindrical shells playing the role of the massless blocks. Let the stick-slip torque perturb a system's simple harmonic motion:

$$I \ddot{\theta} = -k_1 \theta - \hat{v} k_{ss} (\sqrt{A} - \sqrt{2} \sqrt{A - \hat{v} \theta}) \quad (\text{D.40})$$

Or, expressed as a function of time,

$$\begin{aligned} \tau_{ss}(t) &= -\hat{v} k_{ss} (\sqrt{A} - \sqrt{2} \sqrt{A - \hat{v} A \sin(\omega t)}) \\ &= -\hat{v} k_{ss} \sqrt{A} (1 - \sqrt{2} \sqrt{1 - \hat{v} \sin(\omega t)}) \end{aligned} \quad (\text{D.41})$$

The formalism in Appendix 1 involves breaking this torque down into its Fourier components,

$$\tau_{ss}(t) = A_0 + \sum_n A_n \cos(n \omega t) + B_n \sin(n \omega t) \quad (\text{D.42})$$

The formulas to calculate these torque coefficients are in Appendix A, equations A.15-17:

$$A_0 = \frac{\omega}{2\pi} \int_0^{\frac{2\pi}{\omega}} \tau_{ss}(t) dt = \frac{\omega}{2\pi} \int_0^{\frac{2\pi}{\omega}} -\hat{v} k_{ss} (\sqrt{A} - \sqrt{2} \sqrt{A - \hat{v} A \sin(\omega t)}) \cos(n \omega t) dt = 0 \quad (\text{D.43})$$

$$\begin{aligned}
A_n &= \frac{\omega}{\pi} \int_0^{\frac{2\pi}{\omega}} \tau_{ss}(t) \cos(n\omega t) dt \\
&= \frac{\omega}{\pi} \int_0^{\frac{2\pi}{\omega}} -\hat{v} k_{ss} (\sqrt{A} - \sqrt{2} \sqrt{A - \hat{v} A \sin(\omega t)}) \cos(n\omega t) dt \\
&= 0, \text{ n even} \\
&= \frac{4}{\pi} \frac{(-1)^{\frac{n-1}{2}}}{n(4n^2-1)} k_{ss} \sqrt{A}, \text{ n odd}
\end{aligned} \tag{D.44}$$

$$\begin{aligned}
B_n &= \int_0^{\frac{2\pi}{\omega}} \tau_{ss}(t) \sin(n\omega t) dt \\
&= \frac{\omega}{\pi} \int_0^{\frac{2\pi}{\omega}} -\hat{v} k_{ss} (\sqrt{A} - \sqrt{2} \sqrt{A - \hat{v} \theta}) \sin(n\omega t) dt \\
&= \frac{8}{\pi} \frac{(-1)^{\frac{n+1}{2}}}{4n^2-1} k_{ss} \sqrt{A}, \text{ n odd} \\
&= 0, \text{ n even}
\end{aligned} \tag{D.45}$$

Plugging these into Appendix A, equations A.23-26, yields:

$$\theta_0 = \frac{A_0}{k_1} = 0 \tag{D.46}$$

$$\frac{\Delta \omega^2}{\omega^2} = -\frac{B_1}{A k_1} = \frac{8}{3\pi} \frac{k_{ss}}{\sqrt{A}} \tag{D.47}$$

$$\begin{aligned}
a_{n \geq 2} &= -\frac{A_n}{k_1} \frac{1}{n^2-1} = \frac{4}{\pi} \frac{(-1)^{\frac{n+1}{2}}}{n(4n^2-1)(n^2-1)} \frac{k_{ss}}{k_1} \sqrt{A}, \text{ n odd} \\
&= 0, \text{ n even}
\end{aligned} \tag{D.48}$$

$$\begin{aligned}
b_{n \geq 2} &= -\frac{B_n}{k_1} \frac{1}{n^2-1} = \frac{8}{\pi} \frac{(-1)^{\frac{n-1}{2}}}{(4n^2-1)(n^2-1)} \frac{k_{ss}}{k_1} \sqrt{A}, \text{ n odd} \\
&= 0, \text{ n even}
\end{aligned} \tag{D.49}$$

The effect on Q can be derived in a straightforward manner using Appendix 1, equation A1.28

$$\begin{aligned}\Delta\left(\frac{1}{Q}\right)_{ss} &= -\frac{A_1}{k_1 A} \\ &= \frac{4}{3\pi} \frac{k_{ss}}{k_1} \frac{1}{\sqrt{A}}\end{aligned}\tag{D.50}$$

However, experiments at the UCI gravity lab [17] have shown that to a good approximation,

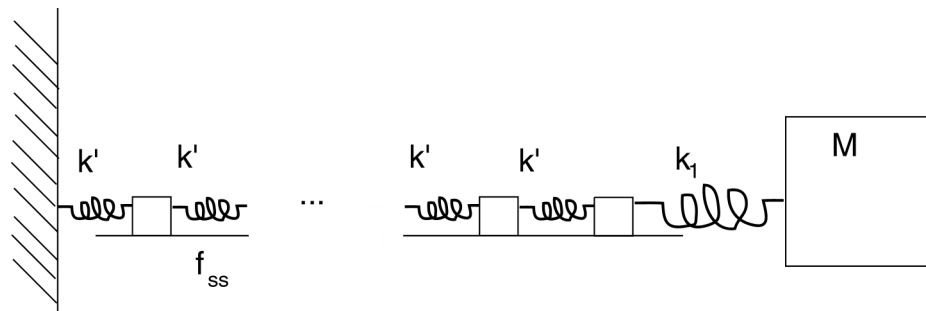
$$\Delta\left(\frac{1}{Q}\right) \propto A\tag{D.51}$$

Therefore, the model presented above cannot be a significant contribution to $1/Q$. However, a variation of this model is potentially viable.

Consider what would happen if Figure 1 were altered so that the long series of stick-slip blocks were located between the massive block and the immobile wall.

Figure D.4

Stick-Slip Blocks in a Series Configuration



Note that the system is now “in series.” The mass is coupled through the linear spring to the stick slip system, and from there to the wall. Neither the stick-slip system nor the k_1 spring can be severed without decoupling the massive block from the wall entirely. From this point onward, the derivation of the stick-slip behavior will follow the path presented in Mike Bantel's thesis, chapter 7, p. 98. For a torsion effect, this would occur if the fiber itself

were anchored by a “stick-slip” region to its mount.

Consider equation 34, reproduced here:

$$x(F_{ss}) \approx -\frac{1}{4k_1^2 \Delta x} [2F_{ss} F_{max} - \hat{v}(F_{max}^2 - F_{ss}^2)] \quad (D.34)$$

This formula does not involve any approximations, beyond the assumption of a large number of stick-slip blocks. It is equally applicable to both the series and parallel situations. Then, consider the effect of the following approximation, which are necessary in the case of a “series” stick-slip torsional force:

$$\begin{aligned} \tau_{ss}(\theta) &= -k_1 \theta \\ \tau_{max} &= -k_1 A \end{aligned} \quad (D.52)$$

The stick-slip torque no longer acts directly on the pendulum. Instead, the stick-slip region acts as an additional spring, extending and contracting to alleviate the tension or compression on the k_1 spring. The relevant differential equation becomes:

$$I \ddot{\theta} = -k_1 (\theta - \theta_{ss}) \quad (D.53)$$

where θ_{ss} is defined by equation 34:

$$\theta_{ss}(\tau_{ss}) = -\frac{1}{4k_1^2 \Delta x} [2\tau_{ss} \tau_{max} - \hat{\theta}(\tau_{max}^2 - \tau_{ss}^2)] \quad (D.54)$$

Plugging equation 55 into equation 57 yields:

$$\theta_{ss}(\theta) = -\frac{1}{4k_1^2 \Delta x} [2k_1^2 A \theta - \hat{\theta} k_1^2 (A^2 - \theta^2)] \quad (D.55)$$

which, when plugged into equation 53, yields the effective stick-slip torque:

$$\tau_{ss} = I \ddot{\theta} + k_1 \theta = \frac{k_1^3}{4k_1^2 \Delta x} [(2A\theta) - \hat{\theta}(A^2 - \theta^2)] \quad (D.56)$$

This equation has both a linear amplitude-dependent correction of the k_1 term (a conservative torque that affects frequency but no harmonics), and a stick-slip term with a

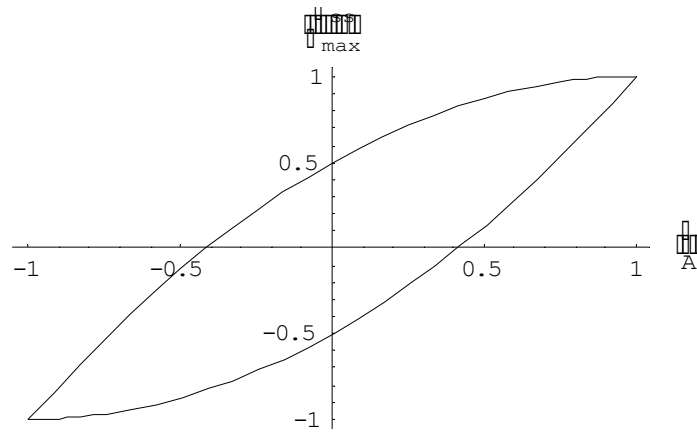
force-hysteresis loop shown in Figure 5. Let us renormalize the k' , Δx , and k_1 terms, and create a single stick-slip term to represent them:

$$\tau_{ss}(\theta) = 2 A k_{ss} \theta - \hat{\theta} k_{ss} (A^2 - \theta^2) \quad (\text{D.57})$$

$$\begin{aligned} \tau_{ss}(t) &= 2 A^2 k_{ss} \sin(\omega t) - \hat{\theta} A^2 k_{ss} [1 - \sin^2(\omega t)] \\ &= A^2 k_{ss} [2 \sin(\omega t) - \hat{\theta} \cos^2(\omega t)] \end{aligned} \quad (\text{D.58})$$

Figure D.5

Torque as a Function of Amplitude
for a Small Series Stick-Slip Effect



In order to find the harmonics, we again turn to Appendix 1, equations A1.15-17, and find the time-series harmonics of the stick-slip force:

$$A_0 = \frac{\omega}{2\pi} \int_0^{\frac{2\pi}{\omega}} \tau(t) dt = 0 \quad (\text{D.59})$$

$$\begin{aligned}
A_n &= \frac{\omega}{\pi} \int_0^{\frac{2\pi}{\omega}} \tau(t) \cos(n\omega t) dt \\
&= \frac{\omega}{\pi} \int_0^{\frac{2\pi}{\omega}} A^2 k_{ss} [2 \sin(\omega t) - \hat{\theta} \cos^2(\omega t)] \cos(n\omega t) dt \\
&= \frac{8}{\pi} \frac{(-1)^{\frac{n+1}{2}}}{n(n^2-4)} A^2 k_{ss}, \text{ n odd} \\
&= 0, \text{ n even}
\end{aligned} \tag{D.60}$$

$$\begin{aligned}
B_n &= \frac{\omega}{\pi} \int_0^{\frac{2\pi}{\omega}} \tau(t) \sin(n\omega t) dt \\
&= \frac{\omega}{\pi} \int_0^{\frac{2\pi}{\omega}} A^2 k_{ss} [2 \sin(\omega t) - \hat{\theta} \cos^2(\omega t)] \sin(n\omega t) dt \\
&= 2A^2 k_{ss}, \text{ n=1} \\
&= 0, \text{ n} \geq 2
\end{aligned} \tag{D.61}$$

The Fourier torque coefficients given in equations 59-61 can be used to determine the shift in frequency and Fourier harmonics of the pendulum using Appendix 1, equations A.23-26:

$$\theta_0 = \frac{A_0}{k_1} = 0 \tag{D.62}$$

$$\frac{\Delta \omega^2}{\omega^2} = -\frac{B_1}{A k_1} = -2A \frac{k_{ss}}{k_1} \tag{D.63}$$

$$\begin{aligned}
a_{n \geq 2} &= -\frac{A_n}{k_1} \frac{1}{n^2-1} = \frac{8}{\pi} \frac{(-1)^{\frac{n-1}{2}}}{n(n^2-4)(n^2-1)} A^2 \frac{k_{ss}}{k_1}, \text{ n odd} \\
&= 0, \text{ n even}
\end{aligned} \tag{D.64}$$

$$b_n = 0 \tag{D.65}$$

As shown in Appendix 1, equation A.28, the contribution to 1/Q is proportional to A_1 :

$$\begin{aligned}
\Delta \left(\frac{1}{Q} \right)_{ss} &= -\frac{A_1}{k_1 A} \\
&= \frac{8}{3\pi} \frac{k_{ss}}{k_1} A
\end{aligned} \tag{D.66}$$

This gives the a contribution consistent with the findings of Newman and Bantel [17].

Some harmonic coefficients of this behavior are given, below.

Table D.1
 a_n For Series Stick-Slip Effect

n	$a_n^*(k_1/k_{ss} A^2)$
3	$1/(15\pi)$
5	$-1(315/\pi)$
7	$1/(1890\pi)$

Note that equation 57 can be expressed as two dissipative terms, one proportional to A^2 , and the other proportional to θ^2 . Both of these contribute to the linear dependence of $1/Q$ on A .

In practice, almost any force with a contribution to $1/Q$ that is linear in amplitude will be an acceptable torque candidate. Multiplying either the A^2 or the θ^2 term in the stick-slip torque by any dimensionless function $f(A/\theta)$ will also result in an acceptable torque profile. In the absence of a measurement of the shape of the stress-strain loop (figures 5, 3, and 2), it is difficult to determine the profile of the torque that generates it [21]. This derivation is an attempt to impose some physical model on the behavior of the pendulum, but in fact the torque profile that produces our measured dependence of $1/Q$ on amplitude is unknown.

Appendix E

An Examination of the Effect of a Magnetic Field on Pendulum

Damping

Consider a region of uniform, static magnetic field,

$$\mathbf{B} = B_0(\cos \psi_0 \hat{\mathbf{x}} + \sin \psi_0 \hat{\mathbf{y}}) \quad (\text{E.1})$$

In this field hangs a thin, flat, nonconductive pendulum painted with a thin conductive ring of resistivity ρ centered about the center of mass of the pendulum. The ring's radius is “ r ,” its thickness is “ ϵ ,” and its width is “ dr .” The ring encloses an area $S = \pi r^2$, and a circuit around the ring has a total resistance of

$$R = \rho \frac{2\pi r}{\epsilon dr} \quad (\text{E.2})$$

The orientation of the pendulum is

$$\hat{\mathbf{n}} = \cos \theta \hat{\mathbf{x}} + \sin \theta \hat{\mathbf{y}} \quad (\text{E.3})$$

The angle ψ_0 in equation 1 describes the angle made by the magnetic field and the normal vector to the pendulum when it (the pendulum) is at rest. The z -axis is parallel to the axis of rotation.

The pendulum's behavior in the absence of a magnetic field is described by a simple harmonic oscillation of frequency ω_0 and amplitude A .

$$\theta_0(t) = A \sin(\omega_0 t) \quad (\text{E.4})$$

The magnetic flux passing through the pendulum as a function of angle is

$$\Phi = S \mathbf{B} \cdot \hat{\mathbf{n}} = B_0 S (\cos \psi_0 \cos \theta + \sin \psi_0 \sin \theta) \quad (\text{E.5})$$

As the pendulum rotates, it induces a magnetic current,

$$I = -\frac{1}{R} \frac{d\Phi}{dt} = -\frac{1}{R} S B_0 (-\cos \psi_0 \sin \theta + \sin \psi_0 \cos \theta) \frac{d\theta}{dt} \quad (\text{E.6})$$

This current generates a magnetic moment of

$$\boldsymbol{\mu}(\theta, \dot{\theta}) = I S \hat{\mathbf{n}} = -\frac{1}{R} S^2 B_0 [-\cos \psi_0 \sin \theta + \sin \psi_0 \cos \theta] \frac{d\theta}{dt} \hat{\mathbf{n}} \quad (\text{E.7})$$

The torque is straightforward to calculate:

$$\begin{aligned} \boldsymbol{\tau}(\theta, \dot{\theta}) &= \boldsymbol{\mu}(\theta, \dot{\theta}) \times \mathbf{B} \\ &= -\frac{1}{R} S^2 B_0^2 [-\cos \psi_0 \sin \theta + \sin \psi_0 \cos \theta] \frac{d\theta}{dt} (\cos \theta \hat{\mathbf{x}} + \sin \theta \hat{\mathbf{y}}) \times (\cos \psi_0 \hat{\mathbf{x}} + \sin \psi_0 \hat{\mathbf{y}}) \\ &= -\frac{1}{R} S^2 B_0^2 (-\cos \psi_0 \sin \theta + \sin \psi_0 \cos \theta) (\cos \theta \sin \psi_0 - \sin \theta \cos \psi_0) \frac{d\theta}{dt} \hat{\mathbf{z}} \\ &= -\frac{1}{R} S^2 B_0^2 \frac{d\theta}{dt} [\sin^2(\theta - \psi_0)] \hat{\mathbf{z}} \end{aligned} \quad (\text{E.8})$$

For convenience, we will use

$$b_{mag} \equiv \frac{1}{R} S^2 B_0^2 \quad (\text{E.9})$$

to describe the strength of the torque, in analogy with “- b v” style damping.

Plugging in equation 1 in order to find the torque as a function of time,

$$\boldsymbol{\tau}(t) = -b_{mag} \dot{\theta} \sin^2(\theta - \psi_0) = -b_{mag} A \omega \cos(\omega t) \sin^2[A \sin(\omega t) - \psi_0] \hat{\mathbf{z}} \quad (\text{E.10})$$

Using appendix A, equations A.15-17 to find the Fourier components of the torque, to express it as

$$\tau_z(t) = A_0 + \sum_{n=0}^{\infty} A_n \cos(n \omega t) + B_n \sin(n \omega t) \quad (\text{E.11})$$

with coefficients

$$A_0 = \frac{\omega}{2\pi} \int_0^{\frac{2\pi}{\omega}} \tau_z(t) dt = 0 \quad (\text{E.11})$$

$$\begin{aligned} A_1 &= \frac{\omega}{\pi} \int_0^{\frac{2\pi}{\omega}} \tau_z(t) \cos(\omega t) dt \\ &= \frac{\omega}{\pi} \int_0^{\frac{2\pi}{\omega}} -b_{mag} A \omega \cos(\omega t) \sin^2[A \sin(\omega t) - \psi_0] \cos(\omega t) dt \\ &= -b_{mag} \frac{\omega}{2} (A - \cos[2\psi_0] J_1(2A)) \end{aligned} \quad (\text{E.12})$$

$$\begin{aligned} A_{n>1} &= \frac{\omega}{\pi} \int_0^{\frac{2\pi}{\omega}} \tau_z(t) \cos(n\omega t) dt \\ &= \frac{\omega}{\pi} \int_0^{\frac{2\pi}{\omega}} -b_{mag} A \omega \cos(\omega t) \sin^2[A \sin(\omega t) - \psi_0] \cos(n\omega t) dt \\ &= b_{mag} \frac{\omega}{2} \cos(2\psi_0) n J_n(2A), \text{ n odd} \\ &= 0, \text{ n even} \end{aligned} \quad (\text{E.13})$$

$$\begin{aligned} B_n &= \frac{\omega}{\pi} \int_0^{\frac{2\pi}{\omega}} \tau_z(t) \sin(n\omega t) dt \\ &= \frac{\omega}{\pi} \int_0^{\frac{2\pi}{\omega}} -b_{mag} A \omega \cos(\omega t) \sin^2[A \sin(\omega t) - \psi_0] \sin(n\omega t) dt \\ &= b_{mag} \frac{\omega}{2} \sin(2\psi_0) n J_n(2A), \text{ n even} \\ &= 0, \text{ n odd} \end{aligned} \quad (\text{E.14})$$

Now that we have the time-series torque effects, we can apply these to determine the measurable pendulum behavior: offset, change in frequency, harmonic oscillations, and energy dissipation using Appendix A, equations A.23-A.26.

$$\frac{\Delta \omega^2}{\omega_0^2} = -\frac{B_1}{A k_1} = 0 \quad (\text{E.15})$$

$$\theta_0 = \frac{A_0}{k_1} = 0 \quad (\text{E.16})$$

$$\begin{aligned}
a_n &= -\frac{A_n}{k_1} \frac{1}{n^2-1} \\
&= -\frac{b_{mag}}{k_1} \frac{\omega}{2} \cos(2\psi_0) \frac{n}{n^2-1} J_n(2A), \text{ n odd} \\
&= 0, \text{ n even}
\end{aligned} \tag{E.17}$$

$$\begin{aligned}
b_n &= -\frac{B_n}{k_1} \frac{1}{n^2-1} \\
&= -\frac{b_{mag}}{k_1} \frac{\omega}{2} \sin(2\psi_0) \frac{n}{n^2-1} J_n(2A), \text{ n even} \\
&= 0, \text{ n odd}
\end{aligned} \tag{E.18}$$

$$\begin{aligned}
\Delta\left(\frac{1}{Q}\right) &= -\frac{A_1}{k_1 A} \\
&= \frac{b_{mag}}{k_1} \frac{\omega}{2} \left(1 - \cos[2\psi_0] \frac{J_1(2A)}{A}\right)
\end{aligned} \tag{E.19}$$

So the eddy currents do not offer simple “-bv” type damping of the pendulum, but produce harmonics and amplitude-dependent damping.

Applications to the UCI G pendulum

The relationship between the model presented here and that of the square G pendulum is not obvious. The path of electrons for a square pendulum of finite thickness undergoing harmonic oscillation is not simple to calculate, and will not be attempted, here. However, we can deal with the special case of a flat disc-shaped pendulum of area $S = \pi r^2$ where the electric current is constrained to flow in concentric, circular paths about the center of mass of the flat pendulum. While this may not give the exact eddy current damping value for the pendulum, it should give an answer that is accurate to within a close order of magnitude.

First, combining equations 8 and 2,

$$\begin{aligned}
\tau(\theta, \dot{\theta}) &= - \int_0^r \frac{\epsilon}{2\pi r' \rho} [\pi (r')^2]^2 B_0^2 \frac{d\theta}{dt} [\sin^2(\theta - \psi_0)] dr' \\
&= - \frac{\pi \epsilon}{2 \rho} B_0^2 \frac{d\theta}{dt} [\sin^2(\theta - \psi_0)] \int_0^r (r')^3 dr' \\
&= - \frac{\pi \epsilon}{8 \rho} r^4 B_0^2 \frac{d\theta}{dt} [\sin^2(\theta - \psi_0)] \\
&= - \frac{1}{8\pi \rho} \epsilon S^2 B_0^2 \frac{d\theta}{dt} [\sin^2(\theta - \psi_0)]
\end{aligned} \tag{E.20}$$

This gives an “interaction strength” of

$$b_{mag} = \frac{1}{8\pi \rho} \epsilon S^2 B_0^2 \tag{E.21}$$

For the UCI G pendulum, $S = 1.6 * 10^{-3} \text{ m}^2$. For 4K, $\rho_{Al} = 1.1 * 10^{-12} \Omega \text{ m}$ [23], and $\rho_{Au} = 2.2 * 10^{-10} \Omega \text{ m}$ [24]. Although the temperature of the UCI G pendulum was between 2K and 4K, this should not affect the resistivities, as they were quite insensitive to changes in temperature in this range. The aluminum layer has a thickness of 100 nm on each side, while the gold is approximately 200 nm thick on each side. Although the gold is thicker, its two orders of magnitude greater resistivity at this temperature make its contribution to the eddy current damping small compared with that of the aluminum, and so it will be ignored. While differential changes in the vicinity of the pendulum are quite small (see chapter 4), the full field strength is not well known. Assuming (as an upper limit) that the magnetic field in the vicinity of the pendulum is roughly equal to the ambient magnetic field of the earth ($5 * 10^{-5}$ Tesla), we find that

$$\begin{aligned}
b_{mag} &= \frac{1}{8\pi} \frac{2.0 * 10^{-7} \text{ m}}{1.1 * 10^{-12} \Omega \text{ m}} * (1.6 * 10^{-3} \text{ m}^2)^2 (5.0 * 10^{-5} \text{ T})^2 \\
&= 4.6 * 10^{-11} \text{ T}^2 / \Omega = 4.6 * 10^{-11} \text{ kg m}^2 / \text{s}
\end{aligned} \tag{E.22}$$

For a value of $k_1 = 3.3 * 10^{-9} \text{ kg m}^2 / \text{s}^2$ and $\omega = 2\pi / (135 \text{ s}) = .047 / \text{s}$, this gives us a value of $1/Q$ of (from equation 19)

$$\begin{aligned}\Delta\left(\frac{1}{Q}\right) &= \frac{b_{mag} \omega}{2 k_1} = \frac{(4.6*10^{-11} \text{ kg m}^2/\text{s})(.047/\text{s})}{2*(3.3*10^{-9} \text{ kg m}^2/\text{s}^2)} \left(1 - \cos[2\psi_0] \frac{J_1(2A)}{A}\right) \\ &= 3.3*10^{-4} \left(1 - \cos[2\psi_0] \frac{J_1(2A)}{A}\right)\end{aligned}\quad (\text{E.23})$$

At extremely low amplitudes, $1/Q = 3.3 * 10^{-4} \pm 100\%$ (depending on magnetic field orientation), corresponding to a Q of at least 1500 and possibly much greater. At 7.4 radians, $1/Q$ is very close to $3.3 * 10^{-4} \pm 3\%$, which could contribute to a Q of no more 3000 (depending on magnetic field orientation). This is smaller than the observed Q of 80,000+ by a factor of about 27.

Because an 0.5 gauss field has such a deleterious effect on Q, we can work backward from the observed Q to see what upper limit this places on B_0 . By equation 21, b_{mag} is proportional to B_0^2 , so in order to decrease the contribution to $1/Q$ by a factor of 27, we need to attenuate the assumed magnetic field by a factor of at least 5. Therefore the upper limit placed on the magnetic field by eddy current damping is approximately $1*10^{-5}$ T.

Studies of the UCI G experiment (see chapter 4) find that changes in external magnetic fields are attenuated by a factor of 2,000. While this does not tell us what internal magnetic fields may be present, it suggests that the field may be a factor of 2,000 less than the 0.5 gauss assumed for equation 22. If that were the case, then rather than getting a contribution to $1/Q$ of $3.3*10^{-4}$, it would be a contribution of $3.3*10^{-4}/(2*10^3)^2 = 8.3*10^{-11}$. This would only be a significant contribution to damping for a Q on the order of 10^{10} , six orders of magnitude larger than the observed value of Q.